CONTACTLESS POWER TRANSFER FOR ELECTRIC VEHICLE CHARGING APPLICATION

Master of Science Thesis
Swagat Chopra
August 2011

DELFT UNIVERSITY OF TECHNOLOGY
FACULTY OF ELECTRICAL ENGINEERING, MATHEMATICS AND COMPUTER SCIENCE
ELECTRICAL POWER PROCESSING

TUDelft

Contactless Power Transfer for Electric Vehicle Charging Application

August 23, 2011
Delft

Author

Swagat Chopra
4033019

Thesis Committee

prof. dr. eng. J.A. Ferreira
prof.dr.ir. P. Bauer
prof.dr. M. Zeman

Summary

Contactless Power Transfer (CPT) is the process of transferring power between two or more physically unconnected electric circuits or devices by means of magnetic induction. The potential application of CPT can range from power transfer to low power home and office appliances to high power industrial systems. Medical, marine, transportation, battery charging applications where physical connections are either dangerous or impossible or inconvenient are all prospective candidates for use of this technology. This thesis mainly concentrates on development of fundamental theory of CPT and application of CPT technology in achieving driving range extension of Electric Vehicles (EV). The work in this thesis can be divided into three broad categories which are, analysis and development of design criteria of a CPT system, experimental and practical implementation, and range extension studies with on-road charging of EVs using CPT technology.

The main components of a CPT system are specially constructed windings separated apart by a large air gap across which power transfer occurs. These windings form what we call as CPT transformer. In order to achieve efficient power transfer through this large air gap between the windings of the CPT transformer, principle of resonance is used. To increase power transfer capability and to reduce VA rating of the CPT system, capacitive compensation is used in both primary and secondary winding of the CPT transformer. In this regard, Series-Series (SS), Series-Parallel (SP), Parallel-Series (PS) and Parallel-Parallel (PP) topologies are analysed and design criteria for efficient and stable operation are presented. Constant current mode and constant voltage mode operation of SS compensated system are discussed and it is concluded that SS compensation topology is the most suitable topology for battery charging application. Power electronic requirements for efficient power transfer are investigated and it is concluded that use of active rectifiers in the output stage provide more controlling options and higher power transfer efficiency.

To test the many analytically deduced design considerations and feasibility of a CPT system with respect to the efficiency of power transfer, an experimental setup is built. The efficiency of power transfer was measured to be close to 91%. But since DC power is required at the output to accomplish battery charging process, full bridge diode rectifier is employed in the output stage causing additional losses in the system which brings down the overall efficiency of system to 83.2%. To reduce losses in the rectifier stage, use of active rectifier is recommended. Later, CPT charging process is successfully demonstrated on MagIC (Magnetically Induced Charging) car, which is a radio controlled car with super capacitors acting as the on-board energy storage.

Due to multitude of advantages associated with CPT technology, use of this technology in EV charging application is considered. In particular, application of CPT technology in on-road

charge replenishment of EVs is discussed with the help of two case studies. In the first case study, urban driving scenario is considered in which it is assumed that CPT systems are installed at traffic signals and CPT for charge replenishment would occur whenever the EV stops at a red light. From this case study it is inferred that for the various urban driving cycles under consideration, considerable driving range enhancement is achievable i.e., the driving range of the EV would be more than doubled with CPT of 20kW and for CPT of 30kW there will be no net change in state-of-charge of the battery during the journey which implies minimum use of on-board battery. In the second case study, highway driving scenario is considered in which case charge replenishment occurs when the EV drives over the primary winding buried underneath the highway. From this case study, it is concluded that to attain considerable range extension, large portion of the highway will have to be covered by primary winding of the CPT system. For example, a CPT system of 30kW rating and a road coverage of 20% would more than double the driving range and a CPT system of 30kW rating and a road coverage of 40% would cause no net change in state-of-charge of battery during the journey and thereby minimizing the use of on-board battery. However, economic and practical feasibility of such on-road charge replenishment systems have to be studied further in detail. A cost estimate of such CPT systems for stationary EV charging application is also presented.

Acknowledgements

This research has been carried out at the Delft University of Technology, The Netherlands, in the group of Electrical Power Processing (EPP). This thesis could not have been finished without the help and support of many people. I would like to take this opportunity to express my gratitude to them.

First of all, I wish to express my sincere gratitude to my supervisor Prof. Pavol Bauer. I am truly grateful to him for trusting in my ability to complete this work and for his valuable suggestions and ideas during this work. His patience and kindness are greatly appreciated.

I would also like to sincerely thank Rob Schoevaars for his help in building the experimental. Anyone who has worked in the EPP lab knows that Rob invariable has all the answers to their questions.

I would also like to thank fellow masters students for always keeping the spirits high and maintaining a cheerful atmosphere in the 'afstudeerderskamer'. Last but not the least; I would like to thank all the PhD researchers in the EPP group for their inputs.

Contents

Chapter 1

Introduction

1.1 Contactless Power Transfer

The term Contactless Power Transfer (CPT), in general, can be used to describe the power transfer between two objects that are physically unconnected. The word 'contactless' infers some sort of remote action, so that the transfer of power could occur over a physical distance i.e., a non-galvanic contact is established between the source and the load that enables power transfer. In the context of electrical systems, CPT can be achieved by electromagnetic induction or electromagnetic radiation. In this thesis, CPT specifically refers to transfer of electric power between two or more galvanically isolated electric circuits by means of magnetic induction. However, in literature, there exist a large number of terms that describe the same phenomenon. Some of these terms are contactless inductive energy transfer (CIET), contactless energy transfer (CET), contactless inductive power transfer (CIPT), inductive power transfer (IPT), wireless power transfer (WPT), Witricity and so on.

The use of contactless power transfer is sometimes the only way of transferring power between the source and the load. CPT is must in applications where conventional cables and connectors are either impractical or useless – either for the sake of convenience, safety or because of the absence of another solution. Presently, there are a number of contactless power transfer solutions for applications with varying power levels and varying distances. The applications of this technology can range for power transfer to low power home and office devices to high power industrial applications. Medical, marine, space and transportation are some of the other areas in which this application is used.

1.2 State of the art of CPT technology

In this section, a brief outline of the state of research and production of CPT devices is presented. Because of the large number of applications of CPT technology, this technology has the potential to make its way into the future technological agenda and might play a vital role in existing and future power transfer technologies. A wide spectrum of technological solutions using this technology has been researched and the scientific state of art is illustrated. The CPT solutions because of their large number of applications, for the sake of simplicity, are classified as low power and high power transfer.

1.2.1 Low power transfer

One of the perhaps most popular examples of commercially available low power device that use CPT system today are the range of Sonicare electrical toothbrushes by Philips [1]. The tooth brushes are fitted with rechargeable batteries which can be charged by placing the toothbrush on a charging socket of the charger. In this application, the technology of CPT is employed to make the device electric shock proof. There are some companies that have come up with innovative solutions of powering or charging consumer electronic devices using CPT. These solutions include wireless charging of mobile electronics like cellphones, laptops etc., and direct wireless powering of stationary devices like TV's, desktop PCs, speakers, kitchen appliances, etc. A few of these companies are Witricity, Powermat Fujitsu etc. Use of CPT technology in very low power bio-medical applications has also been an area of interest for researchers. Direct wireless power interconnections and automatic wireless charging for implantable medical devices like ventricular assist devices, pacemakers, defibrillators etc.is being researched.Figure 1.1 shows some of the wireless powering and charging solution existing in the market or being introduced in the market in near future. All these low power applications

Figure 1.1 a) Sonicare Philips toothbrush mounted on a charger b) Powermat charging platform c) Witricity wireless power transfer station d) Fujitsu wireless charging platform

1.2.2 High power transfer

Contactless power transfer has also found a large number of applications where high power needs to be transferred wirelessly. The magnitude of power transfer can range from some kilowatts to hundreds of kilowatts. High power contactless power transfer has found applications in people movers, industrial transport and automation, mining, military and aviation, electric vehicles etc. But, unlike low power transfer applications where the air gap between the load and source is very small and power transfer efficiency is comparatively small, in case of high power transfer the air gap are larger and efficiency of power transfer is intended to be high as the amount of power transfer is large. People movers that utilize the principle of magnetic levitation for their propulsion, along with propulsion, the train acquires by contactless means the energy needed to power its onboard circuits and to recharge the onboard batteries for backup power supply. In case of industrial environments where the use of normal electrical cables and connectors is restricted, contactless transporters and contactless platforms can be used. In cases of underground works and exploration where the environment is more often than not highly explosive, conventional connectors are not safe. To tackle this problem sliding transformer [2] has been proposed as a solution. Contactless power transfer technology is necessary in many military and space system where sealing of compartments is vital. A satellite rotary connection has been proposed [3] for application in space application. Contactless charging of electric vehicles (EV) is a widely researched topic in recent past as this technology can make electric vehicles a more user friendly. In this thesis, emphasis is given to the contactless charging of EVs and hence in the following section, CPT technology for charging of EVs is looked into in detail.

1.3 Electric vehicles and CPT charging

Electric vehicles are not a new phenomenon and have been around since the beginning of automotive era in early 1900s [4] and was in fact the first car to break the speed barrier of 100 kmph in 1899.However with the advent of internal combustion engine and cheap oil in the early 20th century, the EVs went out of mass production. The EVs also grew unpopular because of their very limited driving range. But the idea of an environment friendly, affordable and silent EV has not died and several attempts have been made by car manufacturers to come up with new technologies and make EV more affordable and popular. But glacial pace of advancements in battery technology has been a major setback in broad introduction of EVs on roads. Limited range, slow energy replenishment and cost have been major bottlenecks that limit the use of EVs on a large scale. However, with the development of Li-ion batteries and fast charging infrastructure, and lower cost of production, EVs can become a realistic alternative to conventional vehicles.

Charge replenishment of EVs has been traditionally done via conductive charging by establishing a galvanic connection between the charging station and the vehicle. The obvious and most common way of achieving this contact is to plug a cable into the EV. There are several commercially available products that use conductive charging technology which are simple and reliable solutions. However, one major disadvantage of this is that connection will have to be made manually between the EV and the charging station. This is a source of inconvenience and may also cause safety risks in wet and damp conditions. Another disadvantage of this is that easy automation cannot be achieved with this charging process. A solution to these problems is to use CPT technology for charge replenishment of EVs.

1.3.1 CPT technology for EV charging

General Motors in 1996 and in 1997 introduced two EVs namely EV1 and Chevrolet S-10 EV that were using 'Magne Charge' also known as J1773 charging technology. Magne Charge was the first commercially introduced charger that used the principle of inductive power transfer [5]. Instead of a plug, a 'paddle' as shown in Figure 1.2, containing the primary coil is inserted in a slot in the EV. The slot contains the secondary coil and together with the paddle, a CPT transformer was formed. However, due to limitations with respect to the size of the paddle, the performance of these paddles was not too promising. These paddles also had to be manually inserted in the EV and hence were as inconvenient as the traditional plugs. The EVs however were not a commercial success and were discontinued from manufacturing and the inductive paddle charging technology was not used in future EVs.

Figure 1.2 Magne charger used in EV1 and Chevrolet S-10 EV

However, with renewed interest in e-mobility in recent times, a lot of research interest is being shown to make EVs a viable option for future transportation. CPT charging technology has the potential to bring about a positive change in mindset of people regarding EVs. EVs have traditionally been expensive, with limited driving range, inconvenient with respect to the charging process. However, with introduction of CPT technology for charge replenishment, EVs can become an attractive option. CPT charging has the advantage that it can make the charging process automated, convenient and safe for users and large scale introduction of CPT charging infrastructure can help reduce the battery pack size and in turn make the EVs more efficient. However, all this cannot be accomplished by using traditional inductive chargers and CPT charging through large air gaps and least possible human interaction are required.

In recent years, some of the major auto manufacturers GM, Tesla Motors, Nissan, Toyota etc. have shown interest in wireless charging technology and have announced that sometime in near future will roll out CPT chargers for their EVs. Also, there are several research groups in various universities which are pursuing research in this field. Figure 1.3 and Figure 1.4. shows artistic impressions of such a proposed CPT charging system for EV application. The primary winding of the CPT system is buried underneath the ground as shown in Fig. 4 and the secondary winding will be located on the EV.

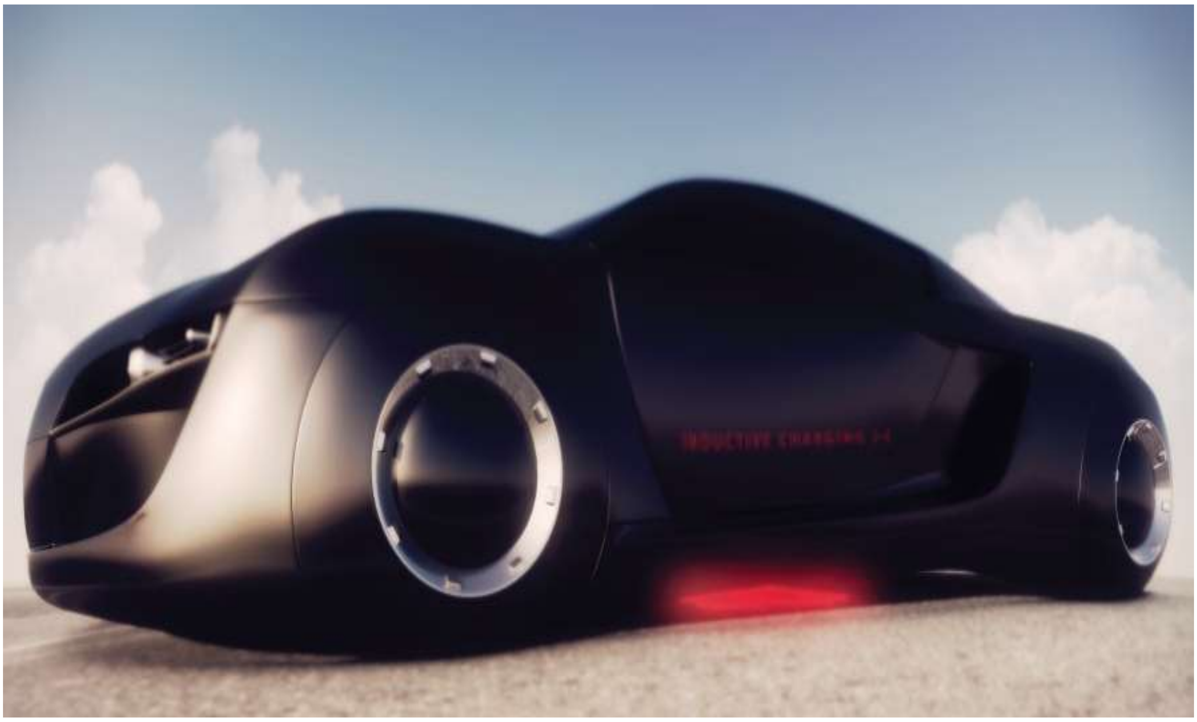

Figure 1.3 An EV being charged by CPT system

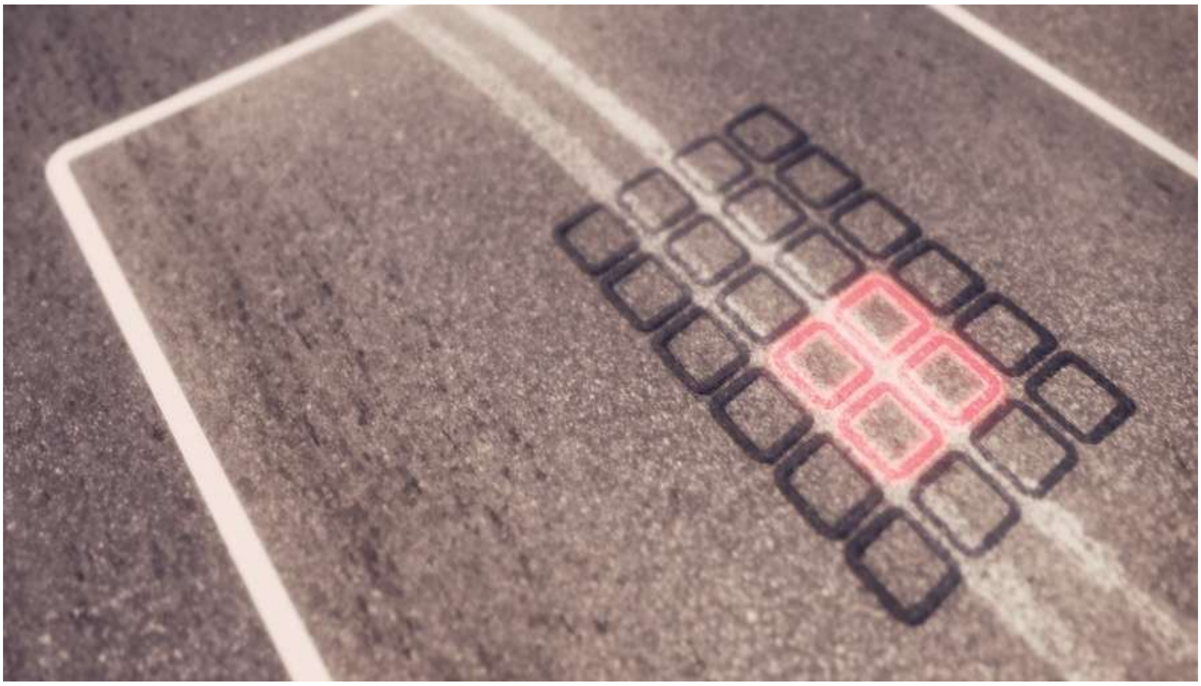

Figure 1.4 Primary winding of the CPT transformer buried under the ground

1.4 Research goals and objectives

With the rising costs of fossil fuel, EVs will play a major role in future transportation and so it not the question of if but when. CPT technology has the potential to bring about a change in how EVs are perceived by making them more use- friendly and if not better, at par with conventional vehicles especially in the aspect of energy replenishment and cost.

The main goals of this thesis are to demonstrate CPT as a feasible technology for charging application in EV and to study the implications of such charging infrastructure on the driving range of an EV. To achieve these goals, following objectives were formulated:

- Develop firm theoretical background of a CPT system

The first objective of this thesis is to build firm theoretical background of the CPT technology based on the knowledge already existing in literature and to pin point key design criteria of a CPT system. The theory so developed will not only be useful for designing a CPT system for EV applications but can be used in general for any CPT application.

- Demonstrate CPT by building a prototype

The second objective of this thesis is to build a demonstrator to demonstrate CPT using the theory developed already. The main objective of building a prototype is to demonstrate that efficient power transfer over relatively large air gaps is achievable. The secondary objective is to study certain practical aspects like tolerance to misalignment.

- Study the effect of CPT charging technology on the range of an EV

The third objective of this thesis is to study the effect of CPT infrastructure on the driving range of an EV. To achieve this, CPT infrastructure installed in urban and highway driving conditions will be considered. In urban scenario, CPT systems installed at traffic lights will be considered, for energy replenishment when the EV is idle at a stop light and in highway scenario, CPT system installed underneath the highway, for energy replenishment in motion, will be considered.

1.5 Organization of the Thesis

This thesis contains six chapters (including the introduction) and the content of each chapter is described hereunder.

- The background theory of CPT is developed in **Chapter 2**. This chapter is dedicated to introducing the reader with theory behind a CPT system and presents some general guidelines for design of a CPT system for any application.
- In **Chapter 3**, power electronic requirements of such a CPT are presented. Emphasis is given on load current control and techniques to achieve this are presented.

- The purpose of **Chapter 4** is to present experimental measurement of a prototype built using the theory developed in chapter 2. Efficiency measurement, effect of misalignment, practical implementation etc. are presented.
- Range extension of an EV with CPT system is discussed in **Chapter 5**. To study the effect of CPT charging on driving range, case studies with CPT infrastructure installed in urban and highway driving scenarios is presented.
- **Chapter 6** contains conclusions from previous chapters and recommendations for future work.

1.6 Publications

Chopra, S., Bauer, P., , "Analysis and design considerations for a contactless power transfer system," *33rd International Telecommunications Energy Conference (INTELEC),* 9-13 Oct. 2011, (paper accepted)

Chopra, S, Bauer, P, , "Driving range extension of an EV with on-road contactless power transfer- A case study," *IEEE Transactions on Industrial Electronics,* (paper under review)

Chapter 2

Analysis and Design Considerations

2.1 Introduction

In this chapter the basic principles of contactless power transfer (CPT) by inductive coupling between the primary and secondary of a loosely coupled transformer is presented. Firstly, the basic concepts used to describe the power transfer between two inductively couples circuits is described. Secondly, the concept of compensation is introduced. Four different compensation techniques are discussed and it is described how compensation can be used to increase the power transfer capability and reduce the VA rating of a CPT system. The phenomenon of bifurcation is introduced for the compensated system and conditions have been presented for stable operation of a CPT system.

2.2 CPT Transformer

An inductively coupled CPT system is capable of efficiently delivering power from a stationary primary source to a movable or stationary secondary source over relatively large air gap. In an inductively coupled CPT system, power is magnetically transferred from the primary winding to the secondary winding of specially constructed transformer.

A number of transformer configurations have been proposed in literature. Generally, these transformers are composed of flat spiral windings [7][8][9]. Some of these proposed transformer configurations have a magnetic core and others have an air core. Factors that influence the choice of transformer are air gap between the primary and secondary winding, cost of the magnetic material core, weight of the core, eddy current losses in the core, operating frequency and sensitivity to misalignment between primary and secondary windings Figure 2.1 and Figure

2.2 show the sectional view of transformer windings with magnetic core and air core respectively.

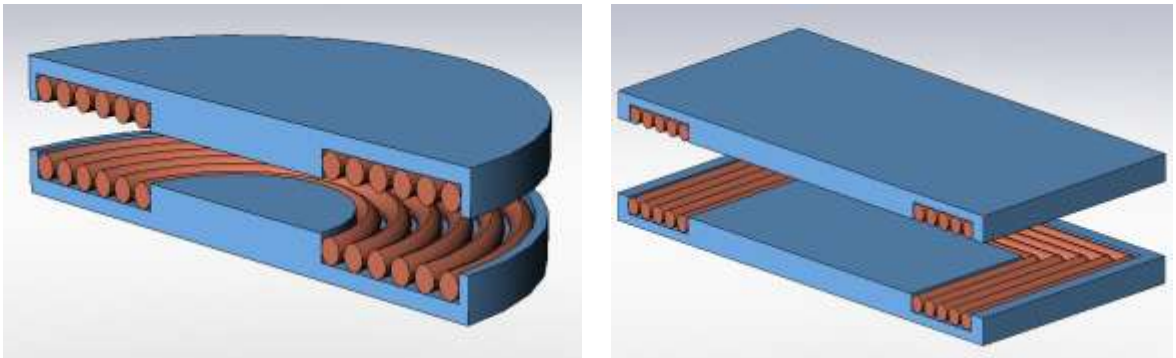

(a) (b)

Figure 2.1 CPT transformer windings with magnetic core a) circular geometry b) rectangular geometry

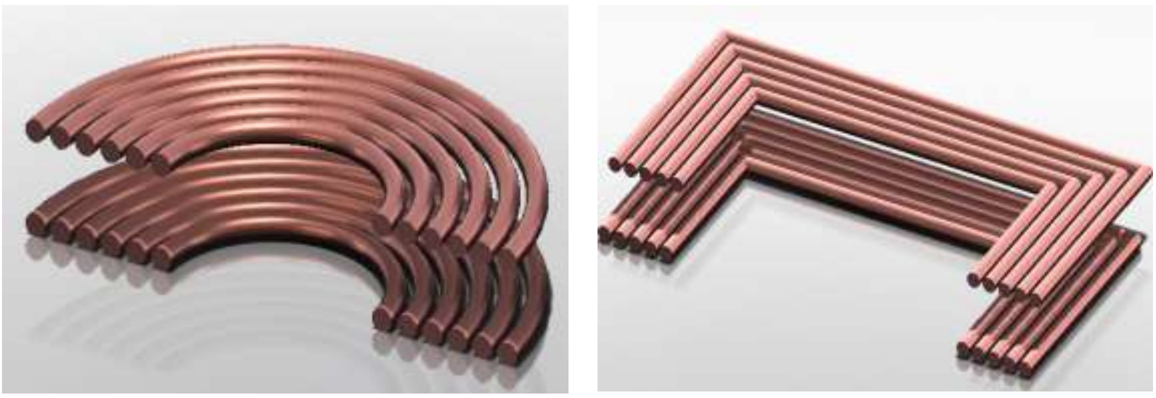

(a) (b)

Figure 2.2 CPT transformer windings with air core a) circular geometry b) rectangular geometry

The air gap in both the transformer configurations is large; so, both these configurations have a large leakage inductance and low mutual coupling which implies large magnetizing current. Since CPT transformer with air core is light in weight and has no core losses [6], for the analysis, CPT transformer with air core is considered. Also the CPT transformer with magnetic core, makes the circuit non-linear. Figure 2.3 shows the circuit representation of a CPT air core transformer. L_1 and L_2 represent the self inductance of primary and secondary winding respectively. The associated primary and secondary winding resistance is represented by R_1 and R_2 respectively. M is the mutual inductance between the transformer winding. The stray capacitances are neglected in representation of the CPT transformer as stray capacitance which dependent on the winding geometry and proximity of conductor to surfaces, become prominent at relatively high frequencies close to the self-resonance frequency of the transformer windings.

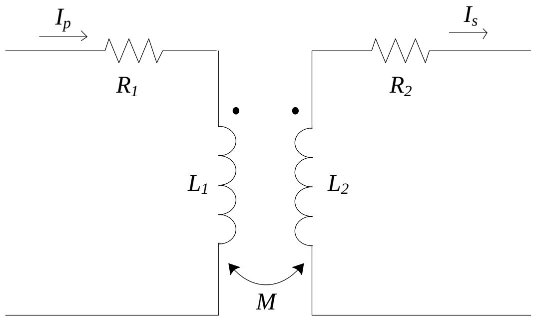

Figure 2.3 CPT air core transformer representation

2.2.1 Winding resistance

The winding resistances R_1 and R_2 of CPT transformer are important factors that determine the efficiency and power transfer capability of a CPT transformer. The DC resistance calculations are based on the simple analytical expressions where the conductor resistivity, its cross-sectional area and length is used to calculate the resistance. At DC or very low frequencies, the magnetic fields inside the conductor are approximately static and hence no additional electric fields are induced in the conductor. The current density is such that it can be considered constant and uniform across the cross section of the conductor. The DC resistance is given by

$$R_{DC} = \frac{\rho l}{A} \tag{2.1}$$

Where l is the length of the conductor, A is the cross sectional area of the conductor and ρ is the resistivity of the conductor material. Copper is the most preferable conductor for this application which has $\rho = 1.68 \times 10^{-8}\ \Omega m$.

However, in CPT applications, the primary is excited with high frequency voltage source which in turn leads to high frequency currents in the windings of the CPT transformer. In general, a conductors carrying time varying current experiences magnetic fields due to their own currents and also magnetic fields due to all current carrying conductors in their vicinity which in turn induces eddy currents in the windings. These eddy currents oppose the penetration of the conductor by the magnetic fields and produce ohmic losses by converting electromagnetic energy into heat. There are two kinds of eddy current effects: the skin effect and the proximity effect. Both of these effects cause non uniform current density in conductors at high frequencies.

2.2.1.1 Skin effect

When a rise in conductor resistance occurs due to the field created by the current flowing in the same conductor, the phenomenon is referred to as skin effect. Skin depth is the term that describes the degree of penetration of a conductor by the magnetic flux and the eddy current. In other words, skin depth is the distance at which the amplitude of electromagnetic wave travelling in the conductor is reduced to $1/e$ times of its original value. The skin effect is negligible only if the skin depth δ is much greater than the conductor thickness. Skin depth for a round conductor is given by

$$\delta = \sqrt{\frac{\rho}{\pi \cdot \mu_r \cdot \mu_0 \cdot f}} \tag{2.2}$$

Where μ_r is the relative permeability of the conducting material. For copper μ_r is very close to 1. μ_0 is the permeability of free space $\mu_0 = 4\pi \times 10^{-7} Hm^{-1}$.$f$ is the frequency. Figure 2.4 shows the plot of skin depth for a copper conductor as a function of frequency. It can be noted that at high frequencies, skin effect become quite dominant. So, care must be taken so as not to neglect this effect at high frequencies.

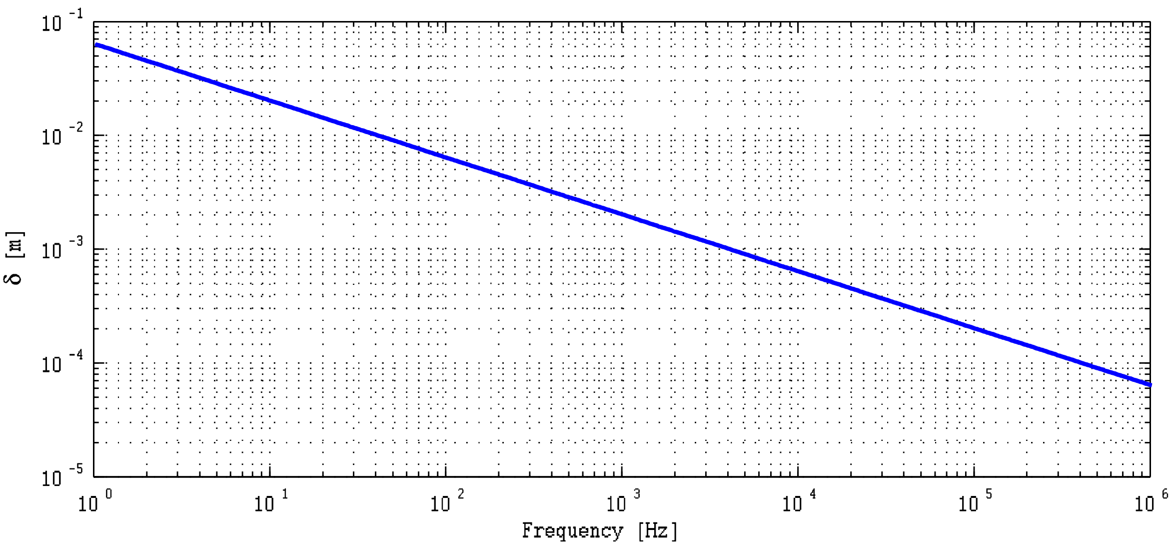

Figure 2.4 Skin depth of a round copper conductor

In literature several methods of calculating the resistance of a conductor as a function of frequency have been presented. The frequency dependent resistance of a round wire can be accurately calculating using the formula derived in [10]. This is given by

$$R_{AC} = \frac{\rho l}{\pi\delta\left(1 - e^{-\frac{r}{\delta}}\right)\left(2r - \delta\left(1 - e^{-\frac{r}{\delta}}\right)\right)} \tag{2.3}$$

Where r is the radius of the round conductor. The derivation of Eq. (3) is based on determining the width of an annulus which carries the equivalent current to the full wire. The relation represented by Eq. (2.3) can be used to accurately determine the AC resistance of a round conductor.

2.2.1.2 Proximity Effect

Another high frequency phenomenon that affects the resistance of a conductor is proximity effect. Proximity effect in inductors and transformers is caused by the time varying magnetic fields arising from currents flowing in adjacent winding layers in multi-layer winding. It is similar to skin effect but is caused by nearby conductors. In other words, the proximity effect causes magnetic field due to high frequency currents in one conductor to induce voltage in adjacent conductors, which in turn cause eddy current n adjacent conductor or in adjacent winding layers in multi-layer inductors or transformers. Proximity effect depends on the conductor geometry, frequency, arrangement of conductors, and spacing between adjacent conductors. Mathematically, proximity effect is very complex to calculate and beyond the scope of this thesis.

At high frequencies, however, Litz wire can be used to form the primary and secondary windings of the CPT transformer as these are designed specifically to minimize the skin effect and proximity effect. The Litz wire is constructed with number of thin insulated strands which are transposed or weaved in such a fashion that both the external proximity effect and the internal skin effect are reduced.

2.3 Basic CPT transformer analysis

In this section the basics of CPT are described. Figure 2.5 shows the circuit diagram for the inductive power transfer from a voltage source to a resistive load. It is assumed that the CPT transformer has an air core and the frequency of operation is far below the self-resonance frequency and hence the stray capacitance can be neglected. The voltage source $V_1$is a sinusoidal voltage source with an oscillation angular frequency of ω. R_L represents the resistive load to which the power is to be transferred. The equivalent circuit representation of the CPT transformer is obtained and represented in Figure 2.6. This equivalent circuit representation makes the process of network analysis easier. In the equivalent representation, $L_a = L_1 - M$ and $L_b = L_2 - M$, i.e., L_a and L_b represent the leakage inductances of primary and secondary windings respectively.

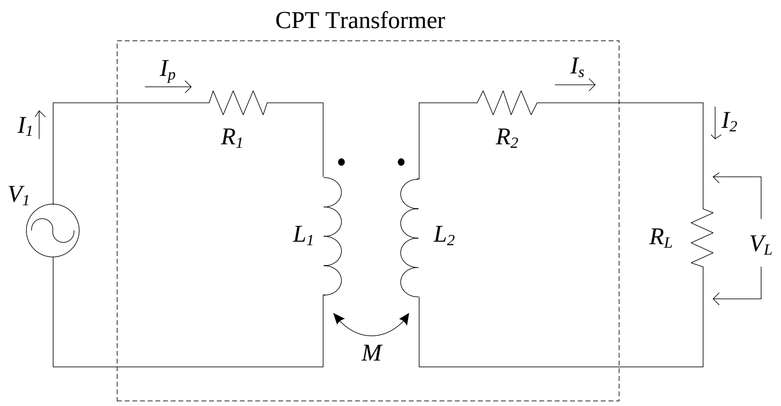

Figure 2.5 Schematic circuit of inductive power transfer to a resistive load

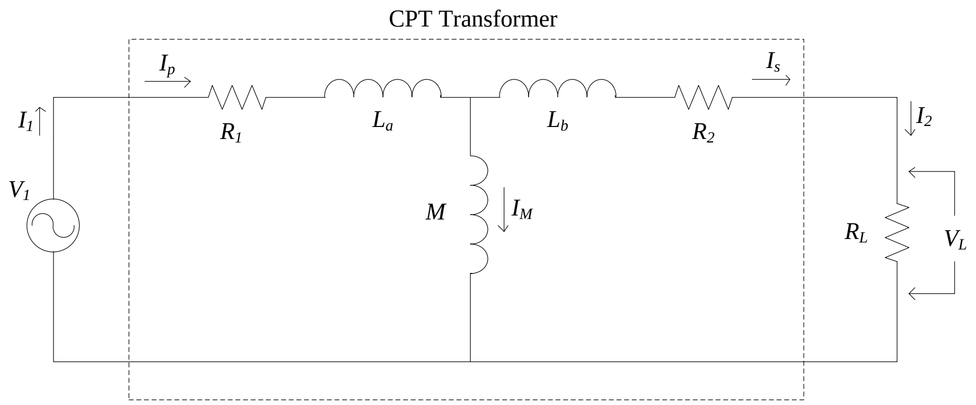

Figure 2.6 Schematic circuit of inductive power transfer to a resistive load with equivalent circuit representation of CPT transformer

Network analysis of circuit shown in Figure 2.6 gives

$$\overrightarrow{I_1} = \frac{\overrightarrow{V_1}}{Z_1} \tag{2.4}$$

Where Z_1 is the impedance of the network as seen by the source given by

$$Z_1 = \frac{\omega^2 M^2 + (R_1 + j\omega L_a + j\omega M)(R_L + R_2 + j\omega L_b + j\omega M)}{R_L + R_2 + j\omega L_b + j\omega M} \tag{2.5}$$

The efficiency of the power transfer is given by

$$\eta = \frac{R_L \left|\overrightarrow{I_2}\right|^2}{R_L \left|\overrightarrow{I_2}\right|^2 + R_2 \left|\overrightarrow{I_s}\right|^2 + R_1 \left|\overrightarrow{I_p}\right|^2} \tag{2.6}$$

$$\begin{aligned} \eta &= \frac{R_L}{R_L + R_2 + R_1 \left(\left(\frac{L_b + M}{M} \right)^2 + \left(\frac{R_2 + R_L}{\omega M} \right)^2 \right)} \\ &= \frac{R_L}{(R_L + R_2)\left(1 + \frac{R1(R_2 + R_L)}{\omega^2 M^2}\right) + R1 \left(\frac{L_b + M}{M}\right)^2} \end{aligned} \tag{2.7}$$

But, for condition specified by Eq. (2.8), power transfer at maximum possible efficiency occurs. This condition can be derived when $\frac{R_1(R_2+R_L)}{\omega_0^2 M^2}$ tends to 0. The maximum theoretical efficiency is given by Eq. (2.9).

$$\omega \gg \frac{\sqrt{R_1(R_2 + R_L)}}{M} \tag{2.8}$$

$$\eta_{\max} = \frac{R_L}{R_L + R_2 + R_1 \left(\frac{L_b + M}{M}\right)^2} \tag{2.9}$$

This CPT transformer model is often used as first approximation to describe the operation principle of contactless power transfer. The efficiency of the CPT transformer as indicated by Eq. (2.7) depends on the load, primary and secondary winding of the CPT transformer. In order to attain high efficiency of CPT, the Eq. (2.9) must be satisfied which in turn means that the frequency of the source must be reasonably high.

The power factor, which is defined as the ratio of active power flowing into a device to the apparent power it draws, is highly dependent on the load and the CPT transformer inductances. However, in order to attain high efficiency of power transfer, high operational frequency satisfying Eq. (2.8) is desirable. But, at relatively high frequencies, the impedance as seen by the source becomes more and more inductive in nature. As a result, the power factor becomes very small and starts approaching zero as the frequency increases. This means that the high frequency source side inverter should have a large VA rating and the circulating power would also decrease the efficiency of power transfer. This is one of the major disadvantages of using basic CPT configuration for power transfer. To overcome this, capacitive compensation in both primary and secondary windings is recommended.

2.4 Capacitive compensation

Compensation capacitors are used in CPT applications to increase the efficiency and the capability of the system they are used in. Capacitive compensation is used in both the primary and secondary windings of the CPT transformer. The purpose of compensation in the secondary winding is to enhance the power transfer capability of the CPT transformer and the primary compensation is used to decrease the VA rating of the source side converter thereby ensuring power transfer at unity power factor. These capacitors essentially store and supply reactive power to and from the secondary and primary windings, reducing the amount of reactive power drawn from the supply.

There exist four basic types of compensation topologies. These are Series-Series (SS) compensation, Series-Parallel (SP) compensation, Parallel-Series (PS) compensation and Parallel-Parallel (PP) compensation.

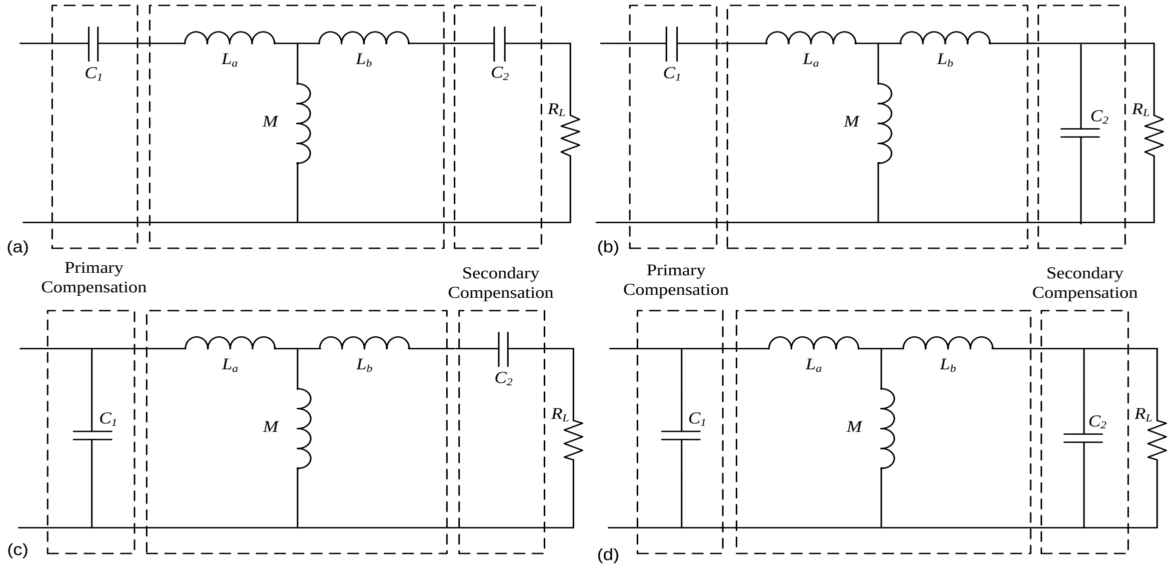

Figure 2.7 Compensation topologies (a) SS (b) SP (c) PS (d) PP

To increase the power transfer capability of CPT system in all the above mentioned topologies, it is necessary that the system operates at the secondary resonance frequency ω_0.When operating at this frequency, the self inductance of the secondary winding is fully compensated by the secondary compensation capacitance and therefore the impedance of the secondary as seen by the primary is purely resistive in nature. Thus, for all the topologies, the value of compensation capacitance C_2 is given by

$$C_2 = \frac{1}{\omega_0^2(L_b + M)} \tag{2.10}$$

The primary compensation for all the compensation topologies is so chosen that the impedance as seen from the source side is purely resistive in nature so as to ensure that high frequency inverter which acts as the primary power source has minimum possible VA rating, i.e., the input current and voltage are in phase. Analysis of all four compensation topologies is presented in following sections and equations are derived for choice of primary compensation capacitance.

2.4.1 SS compensation topology analysis

The equivalent circuit representation of SS compensated topology is given by Figure 2.8.

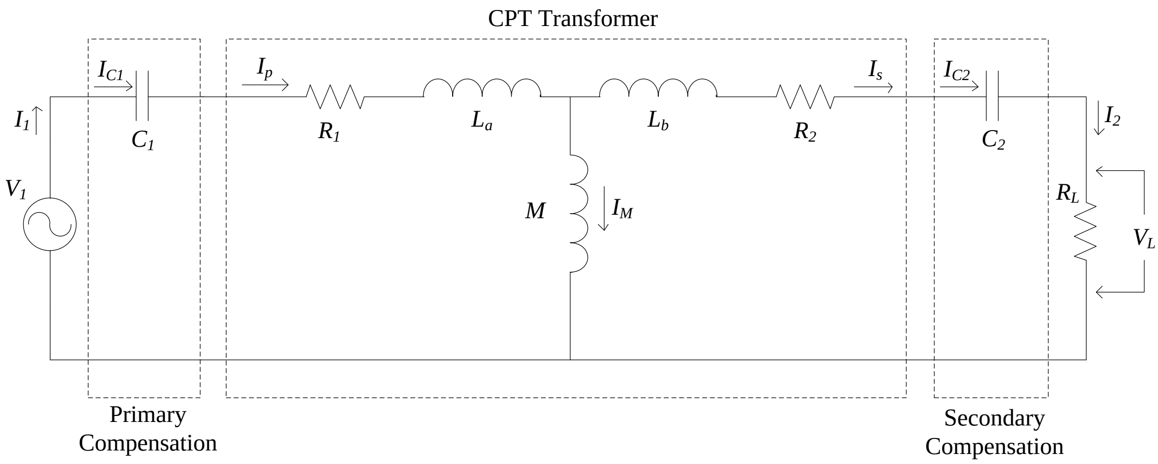

Figure 2.8 SS topology circuit representation

The impedance as seen by the voltage source, $Z_{1,SS}$ when operating at an angular frequency ω is given by

$$Z_{1,SS} = \frac{M^2\omega^2}{j\omega(L_b + M) - \frac{j}{\omega C_2} + R_2 + R_L} + j\omega(L_a + M) - \frac{j}{\omega C_1} + R_1 \tag{2.11}$$

The imaginary part of the impedance $Im(Z_{1,SS})$ as seen by the source is given by

$$Im(Z_{1,SS}) = \left(\omega(L_a + M) - \frac{1}{\omega C_1}\right) - \frac{\omega^2 M^2 \left(\omega(L_b + M) - \frac{1}{\omega C_2}\right)}{(R_L + R_2)^2 + \left(\omega(L_b + M) - \frac{1}{\omega C_2}\right)^2} \tag{2.12}$$

However, in order to attain high power transfer capability the operating frequency should be equal to the secondary resonance frequency as explained earlier. The secondary frequency ω_0 is given by

$$\omega_0 = \frac{1}{\sqrt{(L_b + M)C_2}} \tag{2.13}$$

Since the primary capacitance is so chosen such that $Im(Z_{1,SS}) = 0$. Using this condition and Eq. (2.12) and Eq. (2.13), an equation can be derived for the choice of primary capacitance C_1.

$$\left(\omega_0(L_a + M) - \frac{1}{\omega_0 C_1}\right) - \frac{\omega_0^2 M^2 \left(\omega_0(L_b + M) - \frac{1}{\omega_0 C_2}\right)}{(R_L + R_2)^2 + \left(\omega_0(L_b + M) - \frac{1}{\omega_0 C_2}\right)^2} = 0 \tag{2.14}$$

Therefore, from Eq. (2.14),

$$C_1 = \frac{1}{\omega_0^2(L_a + M)} \tag{2.15}$$

In SS topology, the primary compensation capacitance as given by Eq. (2.15), is only dependent on the secondary resonance frequency and the self- inductance of the primary winding. The self inductance of both the primary and secondary windings is independent the relative position of the two windings and only depend on the physical dimensions and geometry of the windings.

However, the objective is also to attain high efficiencies of power transfer through CPT. Therefore the behaviour of CPT efficiency with respect to the operating frequency of the power source is studied.

The efficiency of power transfer from the voltage source $V_1$to the load R_L is given by

$$\eta = \frac{\left|\overrightarrow{I_2}\right|^2 R_L}{\left|\overrightarrow{I_p}\right|^2 R_1 + \left|\overrightarrow{I_s}\right|^2 R_2 + \left|\overrightarrow{I_2}\right|^2 R_L} \tag{2.16}$$

From Figure 2.8, $I_s = I_2$ and

$$\frac{|I_p|}{|I_2|} = \frac{R_2 + R_L}{\omega_0 M} \tag{2.17}$$

From Eq. (2.16) and Eq. (2.17)

$$\eta = \frac{R_L}{(R_L + R_2)\left(1 + \frac{R_1(R_2 + R_L)}{\omega_0^2 M^2}\right)} \tag{2.18}$$

From Eq. (2.18), the condition to achieve maximum efficiency can be derived. If $\frac{R_1(R_2+R_L)}{\omega_0^2 M^2}$ tends to 0, maximum possible efficiency can be attained. Therefore,

$$\omega_0 \gg \frac{\sqrt{R_1(R_2 + R_L)}}{M} \tag{2.19}$$

$\eta_{\max}$, the maximum theoretical efficiency can be achieved when condition given by Eq. (2.20) is fulfilled. The maximum theoretical efficiency in that case would be

$$\eta_{\max} = \frac{R_L}{R_L + R_2} \tag{2.20}$$

2.4.2 SP compensation topology analysis

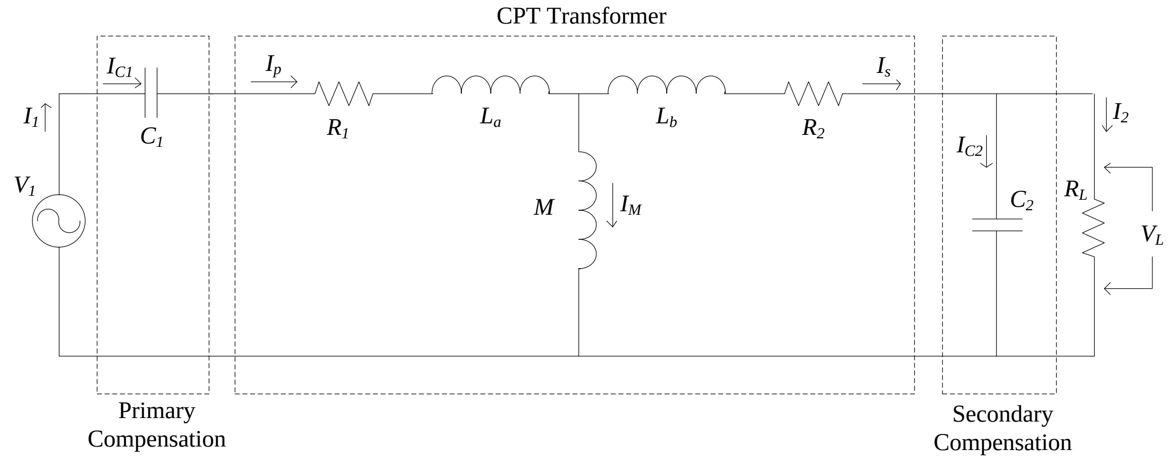

Figure 2.9 SP topology circuit representation

The impedance as seen by the voltage source, $Z_{1,SP}$ when operating at an angular frequency ω is given by

$$Z_{1,SP} = \frac{M^2\omega^2}{j\omega(L_b + M) + R_2 + \frac{R_L}{1 + jR_L C_2 \omega}} + j\omega(L_a + M) - \frac{j}{\omega C_1} + R_1 \tag{2.21}$$

The imaginary part of the impedance $Im(Z_{1,SP})$ as seen by the source is given by

$$Im(Z_{1,SP}) = \left(\omega(L_a + M) - \frac{1}{\omega C_1}\right) - \frac{\omega^3 M^2 (C_2 R_L^2 (\omega^2 (L_b + M) C_2 - 1) + L_b + M)}{(R_2 + R_L - \omega^2 (L_b + M) C_2 R_L)^2 + \omega^2 (L_b + M + C_2 R_2 R_L)^2} \tag{2.22}$$

Since the primary capacitance is so chosen such that $Im(Z_{1,SS}) = 0$. Using this condition and Eq. (2.22) and Eq. (2.13), an equation can be derived for the choice of primary capacitance C_1. However, in the derivation of equation for the capacitance C_1, the effect of primary and secondary resistance associated with CPT transformer windings is neglected.

$$C_1 = \frac{(L_b + M)^2 C_2}{(L_a + M)(L_b + M) - M^2} \tag{2.23}$$

The efficiency of power transfer from the voltage source $V_1$to the load R_L is given by Eq. (2.16).

From Figure 2.9,

$$\frac{\left|\overrightarrow{I_s}\right|}{\left|\overrightarrow{I_2}\right|} = \sqrt{1 + R_L^2 C_2^2 \omega_0^2} \tag{2.24}$$

And

$$\frac{\left|\overrightarrow{I_p}\right|}{\left|\overrightarrow{I_2}\right|} = \frac{\sqrt{R_2^2 + \left((L_b + M)\omega_0 + R_2 R_L C_2 \omega_0\right)^2}}{\omega_0 M} \tag{2.25}$$

By substituting Eq. (2.24) and Eq. (2.25) in Eq. (2.16), we get

$$\eta = \frac{R_L}{R_L + R_2 + \frac{R_2 R_L^2}{\omega^2 (L_b + M)^2} + \frac{R_1 R_2^2}{\omega^2 M^2} + \frac{R_1 \left((L_b + M)\omega^2 + \frac{R_2 R_L}{\omega^2 (L_b + M)}\right)^2}{\omega^2 M^2}} \tag{2.26}$$

Upon further simplification of Eq. (2.26), we get

$$\eta = \frac{R_L}{R_L + R_2 + \frac{R_1 (L_b + M)^2}{M^2}\left(1 + \frac{R_2 R_L^2 M^2 + R_1 R_2^2 (L_b + M)^2}{\omega_0^2 (L_b + M)^2 M^2}\right)} \tag{2.27}$$

From Eq. (2.27), the condition to achieve maximum efficiency can be derived. If $\frac{R_2 R_L^2 M^2 + R_1 R_2^2 (L_b + M)^2}{\omega_0^2 (L_b + M)^2 M^2}$ tends to 0, maximum possible efficiency can be attained. Therefore,

$$\omega_0 \gg \frac{\sqrt{R_2 R_L^2 M^2 + R_1 R_2^2 (L_b + M)^2}}{(L_b + M) M} \tag{2.28}$$

$\eta_{\max}$, the maximum theoretical efficiency can be achieved when condition given by Eq. (2.28) is fulfilled. The maximum theoretical efficiency in that case would be

$$\eta_{\max} = \frac{R_L}{R_L + R_2 + \frac{R_1 (L_b + M)^2}{M^2}} \tag{2.29}$$

2.4.3 PS compensation topology analysis

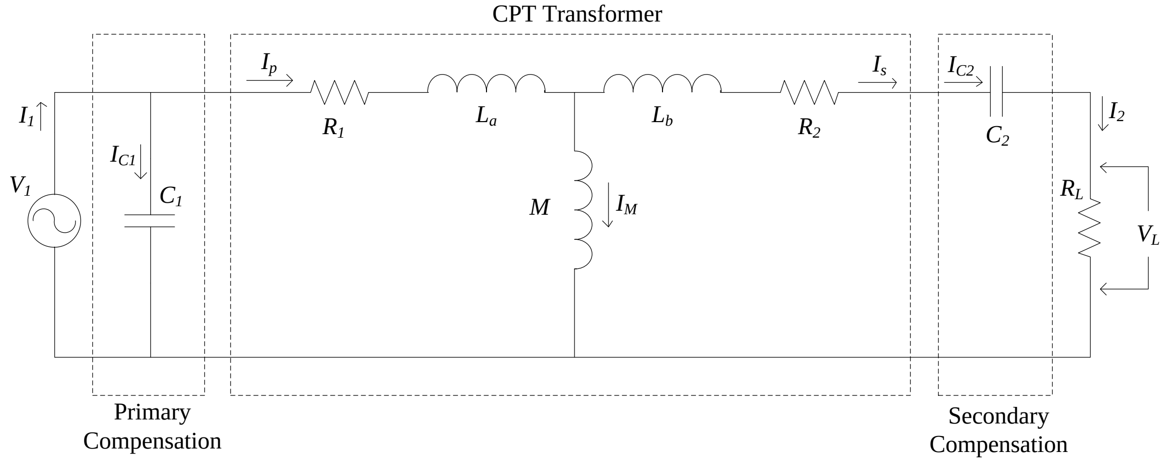

Figure 2.10 PS topology circuit representation

The impedance as seen by the voltage source, $Z_{1,PS}$ when operating at an angular frequency ω is given by

$$Z_{1,PS} = \frac{1}{j\omega C_1 + \cfrac{1}{R_1 + j\omega(L_a + M) + \cfrac{\omega^2 M^2}{R_2 + R_L + j\omega(L_b + M) - \cfrac{j}{\omega C_2}}}} \tag{2.30}$$

Since the primary has a parallel compensating primary capacitance, it is more desirable to continue further analysis with the admittance as seen by the source rather than the impedance.

$$Y_{1,PS} = j\omega C_1 + \frac{1}{R_1 + j\omega(L_a + M) + \cfrac{\omega^2 M^2}{R_2 + R_L + j\omega(L_b + M) - \cfrac{j}{\omega C_2}}} \tag{2.31}$$

By definition the primary capacitance is chosen so that the imaginary part of the impedance or admittance as seen by the source is zero. Therefore to derive an equation for the choice of primary capacitance, $Im(Y_{1,PS}) = 0$. Using this condition and Eq. (2.13), an equation can be derived for the choice of primary capacitance C_1. However, in the derivation of equation for the capacitance C_1, the effect of primary and secondary resistance associated with the CPT transformer windings is neglected.

$$C_1 = \frac{(L_a + M)(L_b + M)^2 C_2^2 R_L^2}{M^4 + (L_a + M)(L_b + M)R_L^2} \tag{2.32}$$

The efficiency of power transfer from the voltage source V_1 to the load R_L is given by Eq. (2.16).

From Figure 2.10,

$$I_s = I_2 \tag{2.33}$$

And

$$\frac{|I_p|}{|I_2|} = \frac{R_2 + R_L}{\omega_0 M} \tag{2.34}$$

From Eq. (2.33)and Eq. (2.34)

$$\eta = \frac{R_L}{(R_L + R_2)\left(1 + \frac{R_1(R_2 + R_L)}{\omega_0^2 M^2}\right)} \tag{2.35}$$

From Eq.(2.35), the condition to achieve maximum efficiency can be derived. If $\frac{R_1(R_2+R_L)}{\omega_0^2 M^2}$ tends to 0, maximum possible efficiency can be attained. Therefore,

$$\omega_0 \gg \frac{\sqrt{R_1(R_2 + R_L)}}{M} \tag{2.36}$$

$\eta_{\max}$, the maximum theoretical efficiency can be achieved when condition given by Eq. (2.36) is fulfilled. The maximum theoretical efficiency in that case would be

$$\eta_{\max} = \frac{R_L}{R_L + R_2} \tag{2.37}$$

2.4.4 PS compensation topology analysis

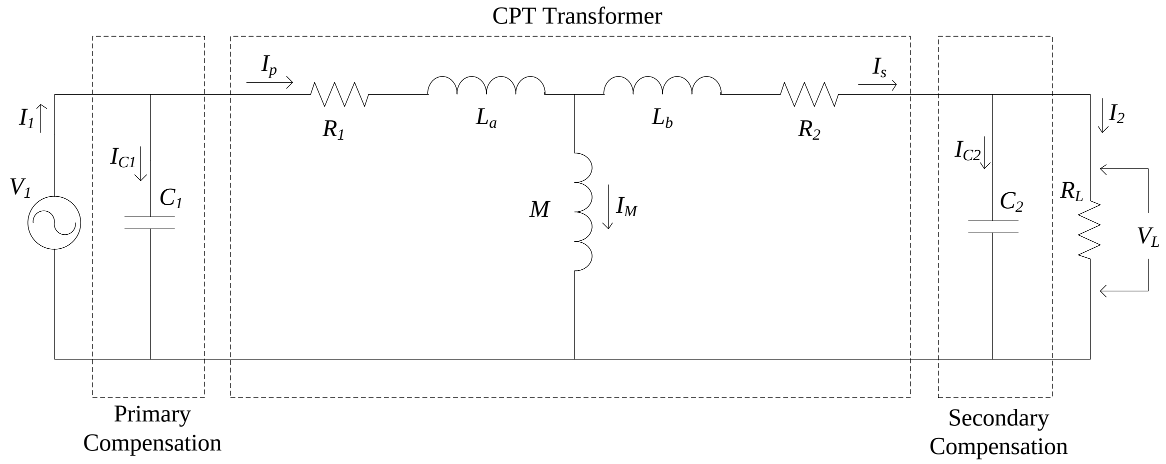

Figure 2.11 PP topology circuit representation

The impedance as seen by the voltage source, $Z_{1,PP}$ when operating at an angular frequency ω is given by

$$Z_{1,PP} = \frac{1}{j\omega C_1 + \frac{1}{R_1 + j\omega(L_a + M) + \frac{\omega^2 M^2 (1 + R_L C_2 \omega)}{\left(R_L + R_2 + j\omega(L_b + M)\right)(1 + R_L C_2 \omega)}}} \tag{2.38}$$

Since the primary has a parallel compensating primary capacitance, it is more desirable to continue further analysis with the admittance as seen by the source rather than the impedance.

$$Y_{1,PP} = j\omega C_1 + \frac{1}{R_1 + j\omega(L_a + M) + \frac{\omega^2 M^2 (1 + R_L C_2 \omega)}{\left(R_L + R_2 + j\omega(L_b + M)\right)(1 + R_L C_2 \omega)}} \tag{2.39}$$

By definition the primary capacitance is chosen so that the imaginary part of the impedance or admittance as seen by the source is zero. Therefore to derive an equation for the choice of primary capacitance, $Im(Y_{1,PP}) = 0$. Using this condition and Eq. (2.13), an equation can be derived for the choice of primary capacitance C_1. However, in the derivation of equation for the capacitance C_1, the effect of primary and secondary resistance associated with the CPT transformer windings is neglected.

$$C_1 = \frac{(L_b + M)^2\left((L_a + M)(L_b + M) - M^2\right)C_2}{\left((L_b + M)(L_a + M) - M^2\right)^2 + M^4 R_L^2 (L_b + M) C_2} \tag{2.40}$$

The efficiency of power transfer from the voltage source $V_1$to the load R_L is given by Eq. (2.16).

From Figure 2.11,

$$\frac{|\overrightarrow{I_s}|}{|\overrightarrow{I_2}|} = \sqrt{1 + R_L^2 C_2^2 \omega_0^2} \tag{2.41}$$

And

$$\frac{|\overrightarrow{I_p}|}{|\overrightarrow{I_2}|} = \frac{\sqrt{R_2^2 + \left((L_b + M)\omega_0 + R_2 R_L C_2 \omega_0\right)^2}}{\omega_0 M} \tag{2.42}$$

By substituting Eq. (2.41) and Eq. (2.42) in Eq. (2.16), we get

$$\eta = \frac{R_L}{R_L + R_2 + \dfrac{R_2 R_L^2}{\omega^2 (L_b + M)^2} + \dfrac{R_1 R_2^2}{\omega^2 M^2} + \dfrac{R_1 \left((L_b + M)\omega^2 + \dfrac{R_2 R_L}{\omega^2 (L_b + M)} \right)^2}{\omega^2 M^2}} \tag{2.43}$$

Upon further simplification of Eq. (2.43), we get

$$\eta = \frac{R_L}{R_L + R_2 + \dfrac{R_1 (L_b + M)^2}{M^2} \left(1 + \dfrac{R_2 R_L^2 M^2 + R_1 R_2^2 (L_b + M)^2}{\omega_0^2 (L_b + M)^2 M^2} \right)} \tag{2.44}$$

From Eq. (2.44), the condition to achieve maximum efficiency can be derived. If $\frac{R_2 R_L^2 M^2 + R_1 R_2^2 (L_b + M)^2}{\omega_0^2 (L_b + M)^2 M^2}$ tends to 0, maximum possible efficiency can be attained. Therefore,

$$\omega_0 \gg \frac{\sqrt{R_2 R_L^2 M^2 + R_1 R_2^2 (L_b + M)^2}}{(L_b + M) M} \tag{2.45}$$

$\eta_{\max}$, the maximum theoretical efficiency can be achieved when condition given by Eq. (2.45) is fulfilled. The maximum theoretical efficiency in that case would be

$$\eta_{\max} = \frac{R_L}{R_L + R_2 + \dfrac{R_1 (L_b + M)^2}{M^2}} \tag{2.46}$$

2.5 Electrical parameters for compensation topologies

Once the operating frequency is determined for the applied load and for the given geometry of the of windings and the coupling coefficient between the windings, and obtaining the expressions for the choice of primary and secondary capacitances, the next step is to obtain the nominal electrical parameters like the voltages across and currents through different elements. It is assumed the load resistance R_L and the power to the load P are already given. The electrical parameters for different topologies are tabulated in Table 2-1.

2.6 Bifurcation

A CPT system can be either operated with a fixed frequency control or a variable frequency control. A fixed frequency control CPT system is assumed to operate at the predefined nominal design frequency which is equal to the secondary resonance frequency. However, for reasons such as temperature rise, if there is a change in secondary compensation capacitance, the secondary resonance frequency would change accordingly. In a fixed frequency control CPT system, this would mean that the system is no longer operating at secondary resonance frequency which will have an adverse effect on the power transfer capability of the CPT system. When operating at off resonance frequency, even a small change in secondary capacitance will have a profound effect on the power transfer capability as shown in [11]. Also, in case of SP, PS and PP topologies where primary compensation capacitance is a function of M and R_L which could vary depending on the positioning of the secondary w.r.t. primary and the load, a fixed frequency system would not always operate at zero phase angle of the power supply i.e., the phase difference between the power supply voltage and current will not be zero. This will cause hard switching of the inverter switches which in turn will lead to higher switching losses.

A variable frequency control can be employed to minimize the required VA rating of the power supply. This can be accomplished by controlling the frequency in such a way that the phase difference between the power supply voltage and current is always zero i.e., the imaginary part of the impedance as seen by the power supply is zero. However, analysis of a compensated CPT system shows that the system could have as many as three zero phase angle frequencies of which only one is the resonance frequency. This phenomenon of existence of more than one zero phase angle frequency is called bifurcation.

The criterion for bifurcation-free phenomenon is strongly dependent on the quality factor of the CPT transformer windings and the coupling coefficient. The coupling coefficient between the primary a primary and secondary winding of the CPT transformer is given by

$$k = \frac{M}{\sqrt{(L_a + M)(L_b + M)}} \tag{2.47}$$

Q_1 and Q_2represent the quality factor associated with the primary and secondary winding of the CPT transformer. These quality factors are defined as the ratio of reactive power to real power and are calculated at the secondary resonance frequency ω_0.

Therefore,

$$Q_1 = \frac{VAr_1}{P_1} \; ; \; Q_2 = \frac{VAr_2}{P_2} \tag{2.48}$$

For the case of SS and PS compensation topologies,

$$Q_1 = \frac{\omega_0 (L_a + M) I_1^2}{\frac{\omega_0^2 M^2 I_1^2}{R_L}} = \frac{R_L (L_a + M)}{\omega_0 M^2} \tag{2.49}$$

$$Q_2 = \frac{\omega_0 (L_b + M) I_L^2}{R_L I_L^2} = \frac{\omega_0 (L_b + M)}{R_L} \tag{2.50}$$

Table 2-1 Electrical parameters for different topologies

	SS	SP	PS	PP
$\overrightarrow{I_2}$	$\sqrt{\frac{P}{R_L}}$	$\sqrt{\frac{P}{R_L}}$	$\sqrt{\frac{P}{R_L}}$	$\sqrt{\frac{P}{R_L}}$
$\overrightarrow{V_L}$	$R_L\overrightarrow{I_2}$	$R_L\overrightarrow{I_2}$	$R_L\overrightarrow{I_2}$	$R_L\overrightarrow{I_2}$
$\overrightarrow{I_{C2}}$	$\overrightarrow{I_2}$	$j\omega C_2\overrightarrow{V_2}$	$\overrightarrow{I_2}$	$j\omega C_2\overrightarrow{V_2}$
$\overrightarrow{V_{C2}}$	$\frac{\overrightarrow{I_2}}{j\omega C_2}$	$\overrightarrow{V_2}$	$\frac{\overrightarrow{I_2}}{j\omega C_2}$	$\overrightarrow{V_2}$
$\overrightarrow{I_s}$	$\overrightarrow{I_2}$	$\overrightarrow{I_2}+\overrightarrow{I_{C2}}$	$\overrightarrow{I_2}$	$\overrightarrow{I_2}+\overrightarrow{I_{C2}}$
$\overrightarrow{I_p}$	$\frac{\left(j\omega(L_b+M)+\frac{1}{j\omega C_2}+R_2+R_L\right)\overrightarrow{I_s}}{j\omega M}$	$\frac{(j\omega(L_b+M)+R_2)\overrightarrow{I_s}+\overrightarrow{V_2}}{j\omega M}$	$\frac{\left(j\omega(L_b+M)+\frac{1}{j\omega C_2}+R_2+R_L\right)\overrightarrow{I_s}}{j\omega M}$	$\frac{(j\omega(L_b+M)+R_2)\overrightarrow{I_s}+\overrightarrow{V_2}}{j\omega M}$
$\overrightarrow{V_{C1}}$	$\frac{\overrightarrow{I_p}}{j\omega C_1}$	$\frac{\overrightarrow{I_p}}{j\omega C_1}$	$(j\omega(L_a+M)+R_1)\overrightarrow{I_p}-j\omega M\overrightarrow{I_s}$	$(j\omega(L_a+M)+R_1)\overrightarrow{I_p}-j\omega M\overrightarrow{I_s}$
$\overrightarrow{I_{C1}}$	$\overrightarrow{I_p}$	$\overrightarrow{I_p}$	$j\omega C_1\overrightarrow{V_{C1}}$	$j\omega C_1\overrightarrow{V_{C1}}$
$\overrightarrow{I_1}$	$\overrightarrow{I_p}$	$\overrightarrow{I_p}$	$\overrightarrow{I_p}+\overrightarrow{I_{C1}}$	$\overrightarrow{I_p}+\overrightarrow{I_{C1}}$
$\overrightarrow{V_1}$	$\left(j\omega(L_a+M)+\frac{1}{j\omega C_1}+R_1\right)\overrightarrow{I_p}-j\omega M\overrightarrow{I_s}$	$\left(j\omega(L_a+M)+\frac{1}{j\omega C_1}+R_1\right)\overrightarrow{I_p}-j\omega M\overrightarrow{I_s}$	$\overrightarrow{V_{C1}}$	$\overrightarrow{V_{C1}}$

For the case of SP and PP compensation topologies,

$$Q_1 = \frac{\omega_0 (L_a + M) I_1^2}{\frac{R_L M^2 I_1^2}{(L_b + M)^2}} = \frac{\omega_0 (L_a + M)(L_b + M)^2}{M^2 R_L} \tag{2.51}$$

$$Q_2 = \frac{(L_b + M)\omega_0 I_s^2}{R_L I_2^2} = \frac{R_L}{\omega_0 (L_b + M)} \tag{2.52}$$

2.6.1 SS topology – bifurcation analysis

In order to analyse the phenomenon of bifurcation, SS topology is considered. However, similar analysis can be carried out for the other three topologies. At the end of this analysis, a condition is derived which when fulfilled will eliminate bifurcation and the CPT system will have only one zero phase angle frequency which will be the resonance frequency.

For the system to have a zero phase angle frequency, the imaginary part of the impedance as seen by the source must be zero, i.e., $Im(Z_{1,SS}) = 0$. For the purpose of this analysis, the resistance associated with the primary and secondary windings of the CPT transformer are neglected. The imaginary part of the impedance as seen by the source is given by

$$Im(Z_{1,SS}) = \left(\omega(L_a + M) - \frac{1}{\omega C_1}\right) - \frac{\omega^2 M^2 \left(\omega(L_b + M) - \frac{1}{\omega C_2}\right)}{R_L^2 + \left(\omega(L_b + M) - \frac{1}{\omega C_2}\right)^2} \tag{2.53}$$

For simplifying the analysis, normalized frequency u as defined by Eq. (2.54) is considered.

$$u = \frac{\omega}{\omega_0} \tag{2.54}$$

From Eq. (2.10) and Eq. (2.15), we get

$$\omega_0^2 = \frac{1}{(L_a + M)C_1} = \frac{1}{(L_b + M)C_2} \tag{2.55}$$

Eq. (2.54) and Eq. (2.55) gives

$$u^2 = (L_a + M)C_1\omega^2 = (L_b + M)C_2\omega^2 \tag{2.56}$$

By substituting Eq. (2.56) in $Im(Z_{1,SS}) = 0$, Eq. (2.57) is obtained.

$$(u^2 - 1)((u^2 - 1)^2 + R_L^2\omega^2 C_2^2 - M^2\omega^4 C_1 C_2) = 0 \tag{2.57}$$

Eq. (2.57) can have at most three real roots of which $u = 1$, is one of the roots which corresponds to zero phase angle frequency being equal to the resonance frequency. Further simplification of Eq. (2.57) gives Eq. (2.58), where k is the coupling coefficient.

$$(u^2 - 1)^2 + \frac{u^2}{Q_2^2} - u^4 k^2 = 0 \tag{2.58}$$

For bifurcation-free operation, the roots of the Eq.(2.58) must be complex, i.e., the discriminant of the equation must be less than zero. This gives the criterion for achieving a single zero phase angle frequency for SS topology.

$$Q_2 < \sqrt{\frac{1}{2\left(1 - \sqrt{1 - k^2}\right)}} \tag{2.59}$$

Similar analysis is carried out for all other compensation topologies. The necessary criteria for bifurcation-free operation are tabulated in Table 2-2.

Table 2-2 Necessary criteria for a single zero phase angle frequency

SS topology	$Q_2 < \sqrt{\frac{1}{2\left(1 - \sqrt{1 - k^2}\right)}}$
SP and PP topologies	$Q_2 < \frac{1}{k}\sqrt{1 - k^2}$
PP topology	$Q_2 < \frac{1}{k}$

2.7 Choice of topology

All the four topologies have different advantages and disadvantages, and their choice mainly depends on the type of application. In [12], some of these advantages and disadvantages are presented. Selecting a topology plays a vital role in the correct choice of primary capacitance as shown earlier. Since the series compensated secondary reflects no reactance at the nominal resonance frequency, the primary inductance can be tuned out independent of either the magnetic coupling or the load by series compensated primary network. As the parallel compensated secondary reflects a load-independent capacitive reactance at the nominal resonance frequency, series tuning in the primary is dependent on the magnetic coupling but not on the load. But, because the reflected impedance contain a real component representing the load, parallel tuning in the primary becomes dependent on both the magnetic coupling and the load.

However, for any general CPT system, SS topology has two major advantages that make it exceptionally useful. Firstly, the reflected impedance of the secondary winding on to the primary winding has only a real reflected component and no reactive component. This means that the secondary winding will draw only active when operating at secondary resonance frequency, giving the secondary a unity power factor. The second advantage is that the choice of primary and secondary compensation capacitances is independent of either mutual inductance or the load which means that the primary and secondary resonance frequencies are independent of either the mutual inductance or the load and only depend on the self inductance of the primary and secondary windings and their respective compensation capacitances. Therefore, for applications where relative orientations of the windings as well as load currents are variable, it is desirable to have a CPT system which has a resonant frequency independent of these variables.

In many CPT applications, the transferred power is used to replenish battery charge which means that in these applications, the load is a battery which needs to be recharged. Some of these applications are EV battery charging, battery charging of consumer electronics like cell phones etc. For battery charging applications, SS topology provides some very specific advantages which are described in the following section.

2.7.1 SS topology for battery charging application

Li-ion batteries, because of their high specific power and ability to charge quickly, are being extensively used in applications where batteries act as the primary energy source. The charging process of a Li-ion battery can be divided into two stages; the constant current charging stage and the constant voltage charging stage. During the constant current charging stage, the battery is charged at constant current until the specified peak voltage of battery cells is reached. There is a linear rise of the battery cell voltage during this period of constant current charging. During the constant voltage charging stage, the charging takes place at constant voltage. At the end of constant current charging stage, the battery cell voltage is at the specified peak value and this voltage is maintained across the battery cell throughout the constant voltage charging stage. Therefore, a topology that acts as both a constant current source and constant voltage is very much desirable in battery charging application. Based on the frequency of operation, a SS topology CPT system can act as a constant current source and a constant voltage source without any complex sensory control involved.

2.7.1.1 Constant current source mode

When operating at nominal resonance frequency ω_0, the load current $\overrightarrow{I_2}$ as represented in Figure 2.8, is given by

$$\overrightarrow{I_2} = \frac{\overrightarrow{V_1}}{j\omega_0 M} \tag{2.60}$$

This means that when operating at resonance frequency, the SS topology acts as a constant current source for the load i.e., the load current is independent of the load. Load current $\overrightarrow{I_2}$ is only dependent on the source voltage $\overrightarrow{V_1}$, the resonance frequency ω_0 and the mutual inductance M between primary and secondary windings. Apart from the obvious advantage of this topology in the constant current charging stage, this topology is inherently short circuit proof.

2.7.1.2 Constant voltage source mode

The same topology can also act as a constant voltage source for the load. In order to arrive at the conditions when this topology works in constant voltage source mode, consider the output voltage gain in Laplace domain as represented in Figure 2.8.

$$\frac{\boldsymbol{V_L}(s)}{\boldsymbol{V_1}(s)} = \frac{MC_1C_2R_Ls^3}{1 + R_LC_2s + \big((L_a+M)C_1 + (L_b+M)C_2\big)s^2 + (L_a+M)C_1C_2R_Ls^3 + \big((L_a+M)(L_b+M)C_1C_2 - M^2C_1C_2\big)s^4} \tag{2.61}$$

The input admittance as seen by the source in Laplace domain is given by

$$\frac{\boldsymbol{I_1}(s)}{\boldsymbol{V_1}(s)} = \frac{C_1s + R_LC_1C_2s^2 + (L_b+M)C_1C_2s^3}{1 + R_LC_2s + \big((L_a+M)C_1 + (L_b+M)C_2\big)s^2 + (L_a+M)C_1C_2R_Ls^3 + \big((L_a+M)(L_b+M)C_1C_2 - M^2C_1C_2\big)s^4} \tag{2.62}$$

From Eq. (2.61), ratio of load voltage $\overrightarrow{V_L}$ phasor to the source voltage $\overrightarrow{V_1}$ phasor is given by

$$\frac{\overrightarrow{V_L}}{\overrightarrow{V_1}} = \frac{-jMC_1C_2R_L\omega^3}{(1-(L_a+M)C_1\omega^2)(1-(L_b+M)C_1\omega^2 + j\omega R_LC_2) - M^2C_1C_2\omega^4} \tag{2.63}$$

The phase difference between the load voltage $\overrightarrow{V_L}$ and the source voltage $\overrightarrow{V_1}$ would be either 0^0 or 180^0 at frequencies $\omega_1$and ω_2 given by Eq. (2.64) and Eq. (2.65) respectively.

$$\omega_1 = \sqrt{\frac{\left((L_b+M)C_2 + (L_a+M)C_1 + \sqrt{\big((L_b+M)C_2 - (L_a+M)C_1\big)^2 + (L_a+M)C_1C_2M^2}\right)}{2C_1C_2\big((L_a+M)(L_b+M) - M^2\big)}} \tag{2.64}$$

$$\omega_2 = \sqrt{\frac{\left((L_b+M)C_2 + (L_a+M)C_1 - \sqrt{\big((L_b+M)C_2 - (L_a+M)C_1\big)^2 + (L_a+M)C_1C_2M^2}\right)}{2C_1C_2\big((L_a+M)(L_b+M) - M^2\big)}} \tag{2.65}$$

When operating at frequencies ω_1 and ω_2, the ratio of load voltage $\overrightarrow{V_L}$ phasor to the source voltage $\overrightarrow{V_1}$ phasor is given by Eq. (2.66) and Eq. (2.67).

$$\frac{\overrightarrow{V_L}}{\overrightarrow{V_1}} = \frac{MC_1\omega_1^2}{(L_a + M)C_1\omega_1^2 - 1} \tag{2.66}$$

$$\frac{\overrightarrow{V_L}}{\overrightarrow{V_1}} = \frac{MC_1\omega_2^2}{(L_a + M)C_1\omega_2^2 - 1} \tag{2.67}$$

However, since the CPT system is designed to operate at natural resonance frequency ω_0, Eq. (2.55) holds good. From Eq. (2.64), Eq. (2.65) and Eq. (2.55)

$$\omega_1 = \frac{\omega_0}{\sqrt{1-k}} \;;\; \omega_2 = \frac{\omega_0}{\sqrt{1+k}} \tag{2.68}$$

Correspondingly, the load voltage when operating at frequencies ω_1 and $\omega_2$is given by Eq. (2.69) and Eq. (2.70) respectively.

$$\overrightarrow{V_L} = \sqrt{\frac{L_b + M}{L_a + M}}\overrightarrow{V_1} \tag{2.69}$$

$$\overrightarrow{V_L} = -\sqrt{\frac{L_b + M}{L_a + M}}\overrightarrow{V_1} \tag{2.70}$$

From Eq. (2.69) and Eq. (2.70), it is evident that the load voltage is independent of the load and only depends on the winding parameters and the source voltage. Hence, when operating at frequencies ω_1 and ω_2, SS topology also acts a constant voltage source topology. However, when operating the CPT system at either of the two frequencies ω_1 or ω_2, the system is no longer in resonance and this off-resonance operation will have an adverse effect on the power transfer capability of the system. Also, since the CPT system is no longer operating at the zero phase angle frequency at the source side, the source side inverter will have a larger VA rating when compared to zero phase angle frequency operation. The input power factor can be found by plotting the phase of the transfer functions given by Eq. (2.61) and Eq. (2.62) on the same plot for the given CPT transformer parameters and natural resonance frequency.

2.8 Conclusions

In this chapter, analytical procedures for determining the basic design criteria of a CPT system are presented. The drawbacks of power transfer through a basic CPT transformer which are limited power transfer capability and low input power factor are discussed. As a remedy to these shortcomings, capacitive compensation in both primary and secondary windings of the CPT transformer is discussed. The primary and secondary compensation are employed to reduce the VA rating of the source side power supply and to increase the power transfer capability of the CPT system respectively. Based on this, four compensation topologies are introduced and extensive analysis of each of these compensation topologies is presented. General expressions are derived for the choice of primary and secondary compensation capacitances and the frequency of operation. The variable and fixed frequency control strategies are discussed and the phenomenon of bifurcation is introduced which is existence of more than one zero phase angle frequency of the source side voltage and current. General criteria for bifurcation-free operation of a variable frequency control CPT system are developed.

Later, some general advantages of SS topology over rest of the topologies are discussed. Specific advantages of using SS topology in battery charging application, which are constant current source mode and constant voltage source mode operations, are presented.

Chapter 3

Power Electronic Requirements

3.1 Introduction

There are various kinds of soft switching techniques that can be employed to achieve higher power densities, higher efficiencies and smaller sizes of converters. Soft switching techniques in general enable high frequency switching at high efficiencies by reducing the switching losses and thereby reducing the overall size of the converter by reducing the sizes of the passive components and heat sinks. In a CPT system, it would be a natural choice to go for resonant converter topology switching at resonance frequency of the designed CPT system. This is because, in order to increase the power transfer capability of the CPT transformer and to reduce the VA rating of the converter, the primary and secondary windings are compensated with capacitors. The primary compensation which ensures that the input current and voltage are in phase also indirectly ensures that when switching at resonance frequency, the switching action of the switches would take place at the instance when the current flowing through the switches is zero. This means that Zero Current Switching (ZCS) can be accomplished at resonance frequency switching. In this chapter, to start with, resonant converter topology for CPT system is introduced. Losses in power electronic components in various stages of a CPT system are discussed. Finally, methods of load current control for SS compensation based topology is discussed

3.2 Resonant Converter Topology for CPT System

A resonant power converter contains resonant circuits whose voltage and current waveforms vary sinusoidally during one or more subintervals of switching periods. For the application of CPT systems, the converters have low harmonic distortion because switching takes place at resonant frequency.

Figure 3.1 shows the half bridge and full bridge inverter topologies used to produce a square wave input voltage $u(t)$ which feed the CPT transformer having the fundamental frequency equal to the designed resonance frequency. The Fourier series analysis of voltage $u(t)$ represented by Eq. (3.1) and Eq. (3.2), shows that the spectrum contains fundamental and odd harmonics that feed the compensated CPT transformer. However, since the input current $i_1(t)$, that is fed to the CPT transformer is pure sinusoidal at the resonance frequency and hence cause low harmonic distortion and theoretically no losses are incurred due to harmonics other than the fundamental.

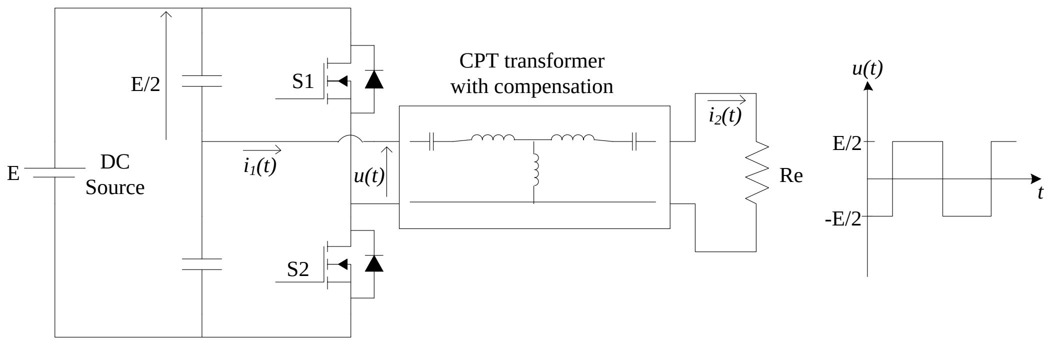

Figure 3.1 Half bridge inverter topology

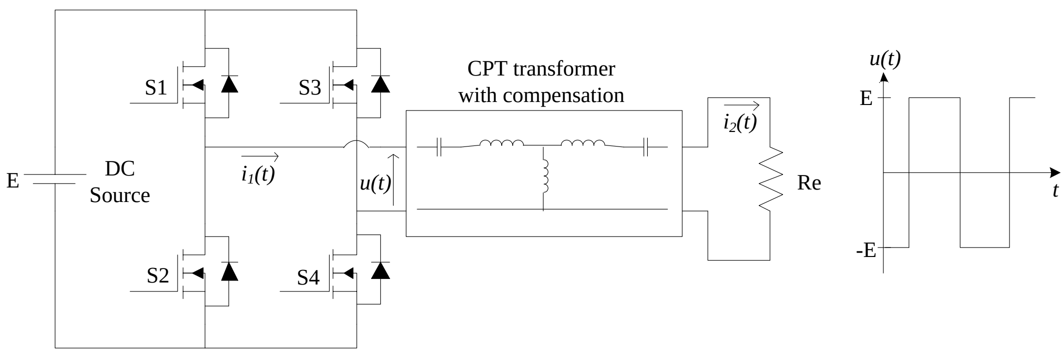

Figure 3.2 Full bridge inverter topology

Fourier series analysis of the input voltage $u(t)$ in case of half bridge and full bridge inverter topologies give

$$u(t) = \frac{4E}{2\pi} \sum_{n=1,3,5\ldots} \frac{1}{n} \sin(n\omega_s t) \tag{3.1}$$

$$u(t) = \frac{4E}{\pi} \sum_{n=1,3,5\ldots} \frac{1}{n} \sin(n\omega_s t) \tag{3.2}$$

Where n is the harmonic number and ω_s is the switching frequency.

For efficient power transfer to take place through the CPT transformer, the switching frequency should be equal to the resonance frequency. The resonance frequency of the system is given by Eq. (3.3).

So $\omega_s = \omega_0$ and

$$\omega_0 = \frac{1}{\sqrt{L_2 C_2}} \tag{3.3}$$

Where L_2 is the self inductance of the secondary winding of the CPT transformer and C_2 is the secondary compensation capacitance.

However, since it is desirable to have DC power at the output, a rectifier circuit and appropriate filter circuit (depending upon the topology used) is a must. So, the main components of a CPT system are input side inverter, CPT transformer and rectifier circuit with appropriate low-pass filter. Because of inherent advantages of SS compensation topology, in the following sections, analysis based on this topology is presented.

3.3 SS topology based CPT system

A SS topology based converter acts as a constant current source converter i.e., when switching at resonance frequency, the current $i_2(t)$ is constant irrespective of the load. Analysis of the SS topology gives us the relation

$$i_2(t) = \frac{u_{1_{(1)}}(t)}{j\omega_0 M} \tag{3.4}$$

Where $u_{1_{(1)}}(t)$ is the fundament component of $u_1(t)$, $M$is the mutual inductance between the primary and secondary windings of the CPT transformer.

A SS topology based CPT system is shown in Figure 3.2. The sinusoidal output current $i_2(t)$ feeds the rectifier network and C_f acts as a low-pass filter. Assuming that filter capacitor C_f is large enough so that ripple in the load current $i_L(t)$ and the ripple in the voltage across the load are negligible, the voltage $u_2(t)$ would appear as a square wave with $u_2(t)$ changing in sign as the current $i_2(t)$ changes its sign because of the nature of the load which is resistive.

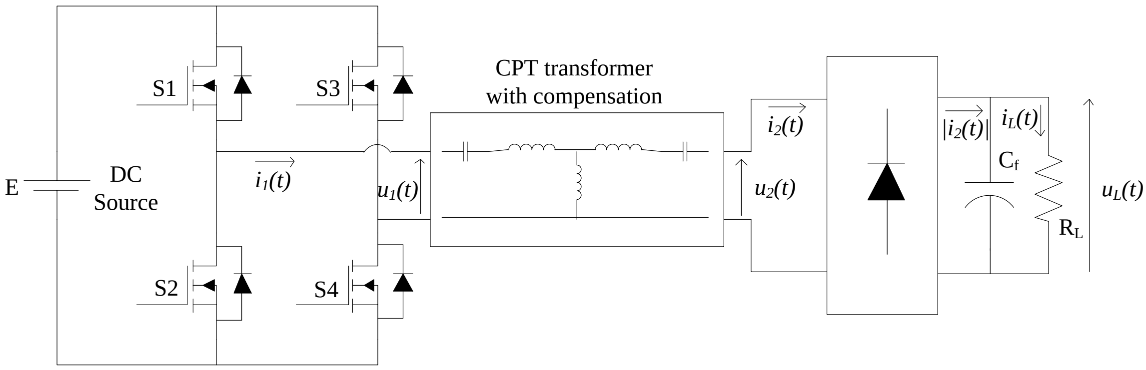

Figure 3.3 Full bridge inverter topology with rectified output and filter

It can be noted from Eq. (3.4) that when switching at resonance frequency, $i_2(t)$ leads the fundamental component of the voltage $u_1(t)$ which is $u_{1_{(1)}}(t)$ by $\frac{\pi}{2}$ radians. Therefore,

$$i_2(t) = I_2 \sin(\omega_s t + \frac{\pi}{2}) \tag{3.5}$$

Where I_2 is the amplitude of the current $i_2(t)$. $u_2(t)$ can be expressed as

$$u_2(t) = \frac{4U_L}{\pi} \sum_{n=1,3,5,\ldots} \frac{1}{n} \sin(n\omega_s t + \frac{\pi}{2}) \tag{3.6}$$

From Eq. (3.6),

$$u_{2_{(1)}}(t) = \frac{4U_L}{\pi} \sin\left(\omega_s t + \frac{\pi}{2}\right) \tag{3.7}$$

Where U_L is the average value of the voltage $u_L(t)$.

The current $i_2(t)$ is rectified by the diode network and then filtered by the filter capacitor C_f. The average value of rectified current $|i_2(t)|$ is equal to the average value of the current flowing through the load i.e., I_L. Therefore,

$$I_L = \frac{2}{\pi} I_2 \tag{3.8}$$

Hence, R_e the load resistance as seen from the resonant converter can be obtained using Eq. (3.7), Eq. (3.8) and Eq. (3.5)

$$R_e = \frac{u_{2_{(1)}}(t)}{i_2(t)} = \frac{8U_L}{\pi^2 I_L} \tag{3.9}$$

Therefore,

$$R_e = \frac{8}{\pi^2} R_L \tag{3.10}$$

In a simplified equivalent circuit for the SS compensated resonant converter, the rectifier and the low pass filter can be replaced by an effective resistance R_e given by Eq. (3.10).

3.4 Converter efficiency

In a SS compensated resonant converter shown in Figure 3.2, losses in the inverter stage, CPT transformer and diode rectifier amount for the majority of losses. Losses in the CPT transformer arise due to resistance associated with the CPT transformer windings which become quite dominating at high operational frequency as discussed in chapter 2. Losses in the input side inverter and load side rectifier are looked more closely in this section.

3.4.1 H-bridge inverter efficiency

Losses in the H-bridge converter have two components; namely the conduction losses and switching losses. When switching the SS converter topology at the resonance frequency, resonant switching takes place i.e., ZCS and ZVS can be accomplished thereby reducing the switching losses during the switching on and/or switching off. This also makes it possible to operate the converter at high switching frequencies when compared to hard switching PWM converters. In case of MOSFETs as the switching components, large turn on losses are observed due to charging of capacitances (C_{gs} *and* C_{gd}) and hence ZVS is desirable in this case. Whereas, in case of IGBTs as the switching components, large turn off losses are observed due to the current tailing effect and hence ZCS is desirable in this case.

The other losses associated with the converter are the conduction losses which are dependent on the type of switches used. In case of MOSFETs as the switching component, the conductions losses are dependent on the current flowing through the switch and the on state drain to source resistance $R_{DS(on)}$. So, for a given current, to reduce the conduction losses, MOSFET with larger current rating can be used as these have lower $R_{DS(on)}$. Using MOSFETs with large current rating will, however, mean that larger gate current is required to turn on the MOSFET which may cause greater constraints on the driver circuit employed. In case of IGBT as the switching device, the conduction losses are smaller when compared to that of MOSFET owing to the low forward voltage characteristics. But IGBTs are not as fast as MOSFETs and the choice between the two should be made based on the switching frequency and power rating of the converter.

3.4.2 Rectifier efficiency

Rectification of AC power to DC could very easily be achieved using a diode bridge rectifier. However, efficiency wise, this is not a very good option. Not much emphasis has been given in literature to the power loss in the rectification stage. In most of the references that analyse and discuss the CPT for battery charging application [17][18][19][20][21][22] this aspect is neglected. Diode rectifiers lead to large losses and can significantly reduce the efficiency of the system.

Diodes that are employed in low switching frequency converters have predominantly conduction losses. However, at high switching frequency, the transient losses in a diode are also quite significant. The conduction losses in a diode are due to forward bias voltage and the on state resistance. The transient losses in a diode are due to the phenomenon of reverse recovery current. So for large conduction currents and high frequency rectification, the losses in the diodes can become significantly high. Schottky diodes can be employed for high frequency operation as they have a very low reverse recovery current but then their forward bias voltage drop is quite significant and thereby increases the conduction losses. Therefore, in applications of CPT battery charging which requires high output currents and also relatively high switching frequency operations, diode rectification is not a very efficient option. In order to achieve high efficiency rectification, active rectifiers must be employed. This would also mean that additional controls have to be used to control the switching in the active rectifier which is a drawback both in terms reliability and cost of the system. But, the active rectifier also presents the opportunity to control the load current. This is discussed in later parts of this chapter.

3.5 Ripple calculation

The ripple in the load current $i_L(t)$ is governed by the filter capacitor C_f and the load R_L. It is required to limit the ripple in output (current and voltage) to a specified value. Therefore, in this section, a method is described to calculate the output ripple for the predefined load and filter capacitor. Since the SS topology resonant converter is a constant current source converter at the design resonance frequency, for the analysis of ripple in the load current, a constant current source is considered as the input to the rectifier network as shown in Figure 3.4(a). Figure 3.4(b) shows the equivalent representation of the rectifier circuit.

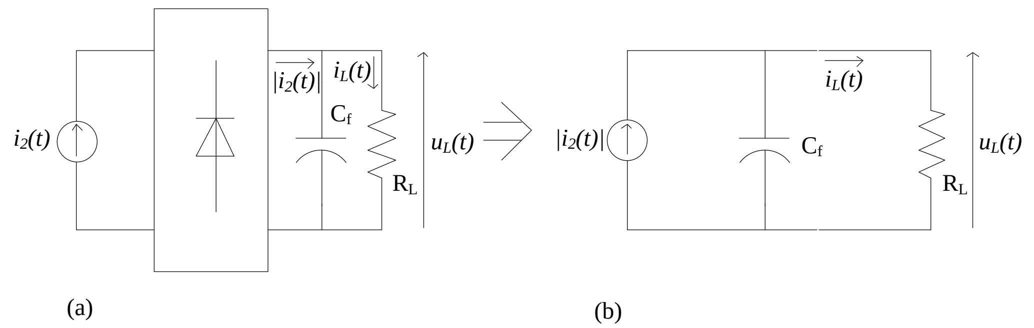

Figure 3.4 : a) Current source representation with rectifier and filter b) Equivalent rectifier and current source representation

The current $|i_2(t)|$ which is the rectified form of current $i_2(t)$ is henceforth referred to as $i_R(t)$. In order to determine the ripple in the load current, first the Fourier series analysis of the current wave $i_R(t)$ is performed. The DC component of this wave will determine the average value of the load current and harmonics will determine the ripple in the load current. Fourier series analysis of $i_R(t)$ gives

$$i_R(t) = \frac{2I_R}{\pi} - \frac{4I_R}{\pi} \sum_{n=2,4,6,\dots} \frac{\cos n\omega_s t}{n^2 - 1} \tag{3.11}$$

Where I_R is the amplitude of the rectified current wave $i_R(t)$.

Using the principle of superposition, each component of the Fourier series can be represented as an independent current source as shown in Figure 3.5. Simple phasor analysis can thus be performed to find ripple in the output current. However, since each phasor has different speed of rotation given by $n\omega_s$, while performing the analysis, the effect of each phasor on the ripple has to be analysed separately and then the ripple in the load current due to all the phasors under consideration can be found. From Eq. (3.11), it can be noted that as the harmonic number increases, the amplitude of the harmonic is reduced by a factor $n^2 - 1$ which means that higher order harmonics will have negligible effect on the ripple and can be neglected in the analysis. Using this multiple current source representation, ripple in the output current can be found.

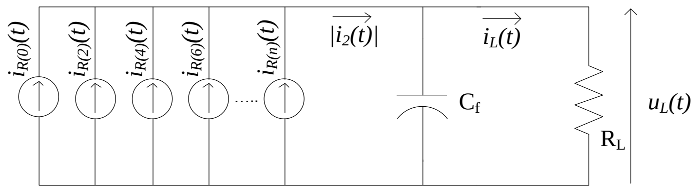

Figure 3.5 Multiple current source representation

3.6 Load current control

In a battery charging CPT system using SS topology resonant converter which acts as a constant current source converter, it is preferable to control the load current as the voltage is already set by the battery which will be the load in this case. In literature [17][18][19][20], an additional DC-DC converter is recommended in order to control the flow of charge to battery as shown in the Figure 3.6(a). However, an additional converter would also cause additional losses. Hence, it is desirable to achieve load current control using the existing power electronics. A CPT system has been proposed in which the DC-DC converter has been eliminated and current control has been achieved by controlling the switching of the inverter (in the input side) and/or the active rectifier (in the output side). This proposed CPT system is shown in Figure 3.6(b). In this section, load current control for the proposed system is discussed. The load current control can be achieved from the load side and/or from the source side. The methodology of source side load current control is the same for the proposed scheme and the scheme existing in literature. However, in case of load side current control, current control by active rectifier is discussed.

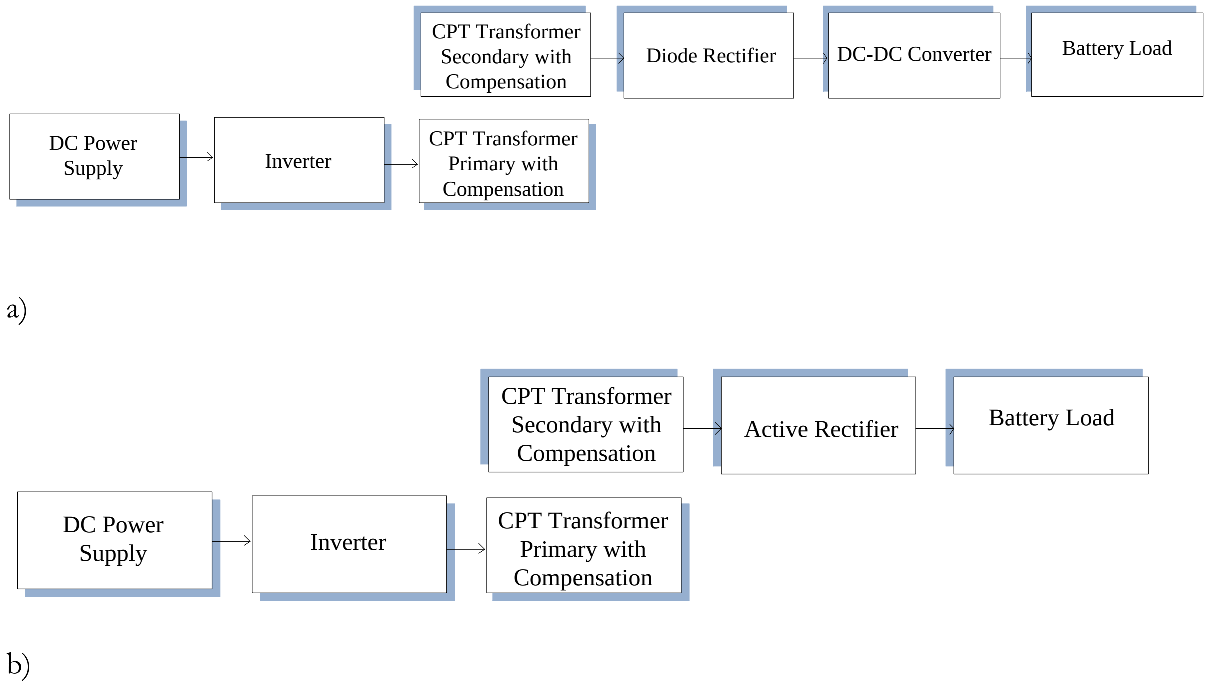

Figure 3.6 a) CPT system as present in literature b) Proposed CPT system

3.6.1 Load current control from source side

Source side current control can be achieved by controlling the switching of switches S1, S2, S3 and S4 shown in Figure 3.7. One way of doing this is by keeping the switching frequency constant at the resonance frequency and change the turn on and turn off duration of the switches, the other way is by changing the switching frequency itself. Later is however not a good way of achieving current control because at off resonance frequency the system efficiency goes down drastically. So, in order to achieve current control at resonance frequency, a switching scheme is proposed namely 'α-control'.

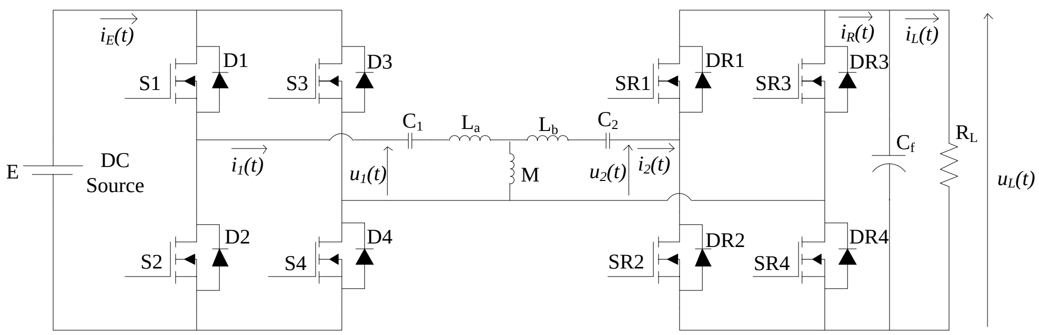

Figure 3.7 Proposed SS topology resonant converter system

3.6.1.1 α-control

In α-control, the switching durations and instances of switches S1, S2, S3 and S4 are controlled in such a way that that fundamental component of the voltage $u_1(t)$ i.e., $u_{1(1)}(t)$ has a frequency equal to the designed resonance frequency of the CPT transformer. The control of the load current is achieved by varying the amplitude of $u_{1_{(1)}}(t)$ as governed by Eq. (3.4). This control is named as α-contol because during one full cycle, for a duration corresponding to α^0, the current $i_1(t)$ flows once thorough the anti-parallel diodes D1 and D4, and once through the anti-parallel diodes D2 and D3. Figure 3.8(b) shows the gate signal to all the switches. Corresponding wave forms of the of the voltage $u_1(t)$, the fundamental component $u_{1_{(1)}}(t)$ and the current $i_1(t)$ are shown in Figure 3.8(a). The DC voltage source current $i_E(t)$ is shown in Figure 3.8(c).

The Fourier series analysis of the voltage $u_1(t)$ gives

$$u_1(t) = \frac{2E}{\pi} \sum_{n=1,2,3,\dots} (1 + cosn\pi + 2cosn\alpha) \sin n\omega_s t \tag{3.12}$$

From Eq. (3.12), the fundamental component of voltage $u_1(t)$ is given by

$$u_{1_{(1)}}(t) = \frac{4E}{\pi} cos\alpha \cdot sin\omega_s t \tag{3.13}$$

Substituting $u_{1_{(1)}}(t)$ in Eq. (3.4) gives

$$i_2(t) = \frac{\frac{4E}{\pi} cos\alpha \cdot sin\omega_s t}{j\omega_s M} \tag{3.14}$$

Therefore, by controlling the amplitude of the fundamental component $u_{1_{(1)}}(t)$ the amplitude of load current $i_2(t)$ can be controlled by using this switching methodology. Figure 3.9 shows the plot of voltage $u_1(t)$ and the fundamental component $u_{1_{(1)}}(t)$ for $\alpha = 30^0$.

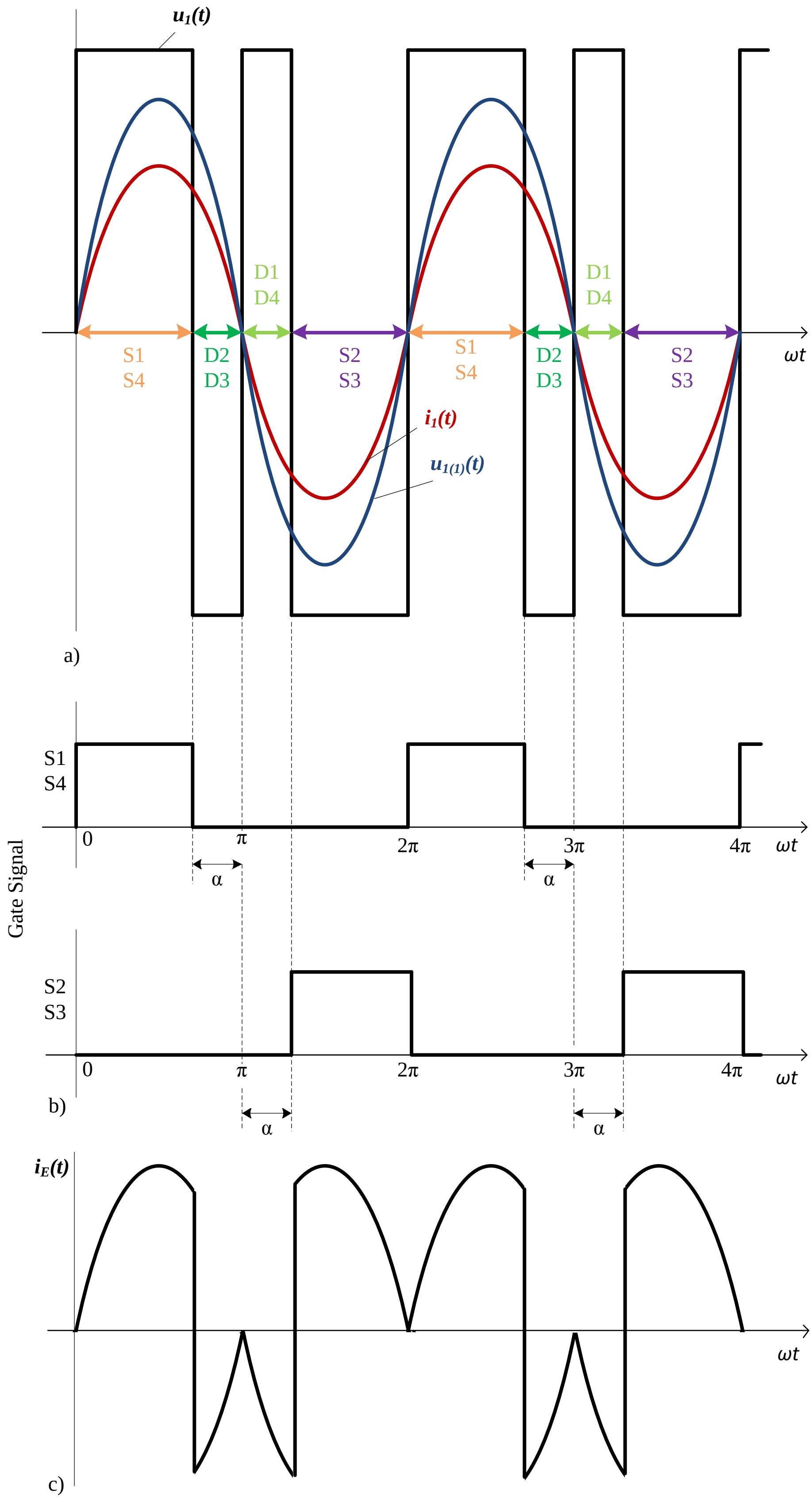

Figure 3.8 a) $u_1(t), u_{1_{(1)}}(t)$ *and* $i_1(t)$ waveforms b) Gate signal to switches D1, D2, D3 and D4 c) DC voltage source current $i_E(t)$

Some salient features of this switching methodology are as follows

The amplitude of the fundamental of voltage $u_1(t)$ and hence the amplitude of the load current $i_2(t)$ is a function of angle α.

For $\alpha = 0^0$, turn-on and turn-off of switches S1, S2, S3 and S4 occur at instance when the current through the corresponding switches is zero, i.e., ZCS occurs. This results in lower switching losses and thereby makes the power transfer more efficient.

For any other α, the turn-on of switches S1 and S3 and turn-off of switches S2 and S4 occur at instances of zero current i.e., ZCS occurs.

The proposed CPT system of the experimental setup is simulated in MATLAB Simulink. With α-control being incorporated in the simulated system, the theoretical and simulation results for the load current control correlate closely as shown in Figure 3.10.

However, one disadvantage of this current control method is that during the duration when neither of the switch pair is conducting, the current flows through the anti-parallel diodes D1 and D4 or D2 and D3 which is generally undesirable because of larger conduction losses that are encountered when current flows through the anti-parallel diodes. Moreover, since these diodes are parasitic, the characteristics of these are dependent on the characteristics of the switch that is being used and cannot be altered. So, in order to reduce the conduction losses during these durations, the parasitic diode can be bypassed by diode of better conduction characteristics but this will also involve another diode which has to be connected in series to the switch causing additional losses.

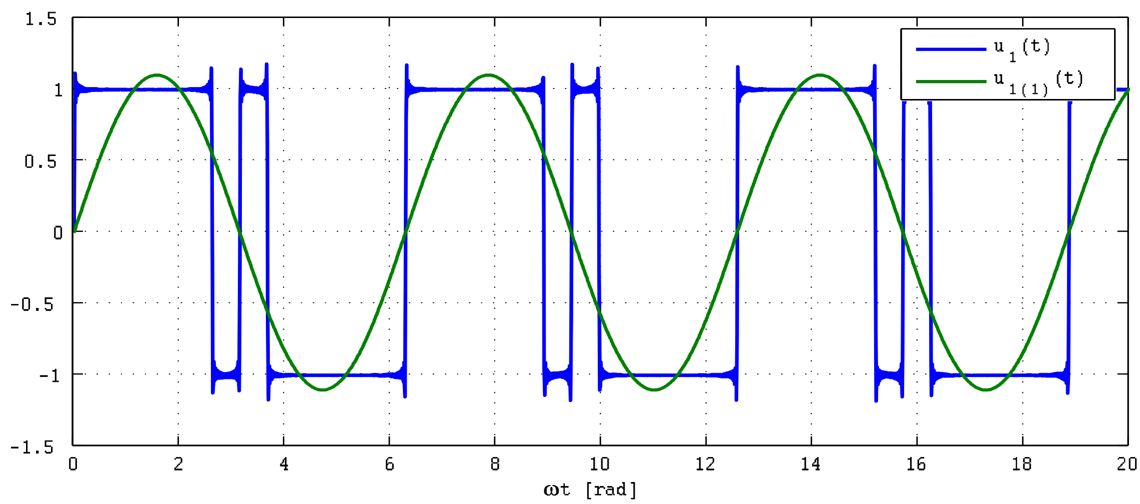

Figure 3.9 Voltage $u_1(t)$ and $u_{1_{(1)}}(t)$ waveform for $\alpha = 30^0$

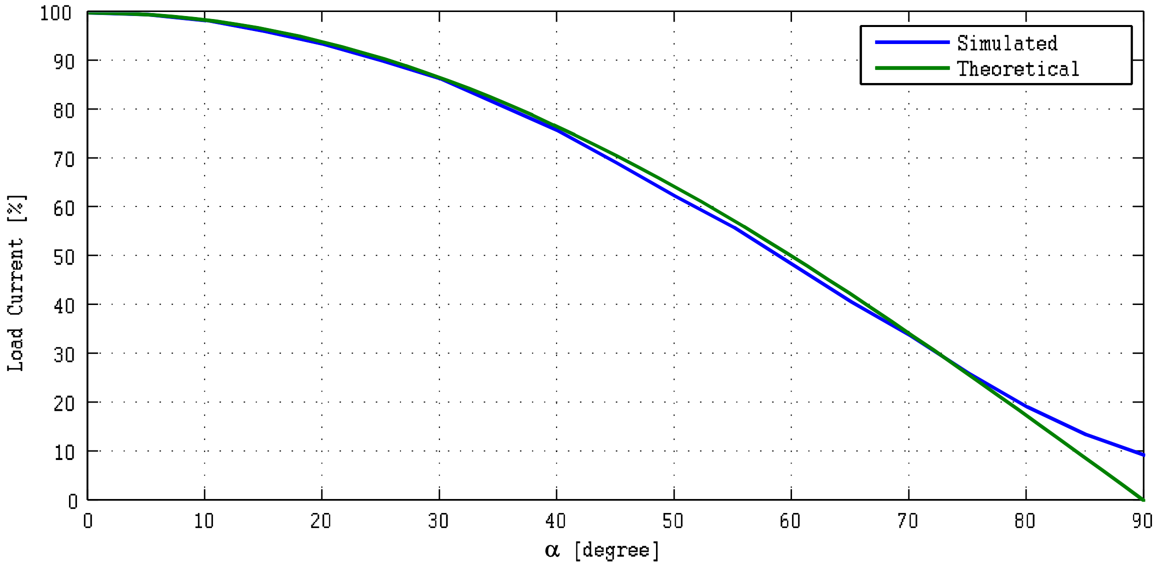

Figure 3.10 Theoretical and simulated load current control with α-control methodology

3.6.2 Load current control from load side

Load current control for the proposed CPT system can also be achieved by controlling the switching instances and duration of the load side active rectifier. While discussing the load current control in this section, the source side inverter switches such that $\alpha = 0^0$. In this current control methodology, the switches SR1, SR2, SR3 and SR4 are switched such that depending upon the load current to be attained, certain current pulses of current $i_2(t)$ flow through the load and certain other current pulses are freewheeled through the anti-parallel diode as shown in Figure 3.11. Since the SS converter topology acts as a constant current source, even during the short circuit that appear at the load side when the current is being freewheeled through the anti-parallel diode, the current will not be higher than the full load current. Figure 3.11(a) shows the $i_2(t)$ current waveform. Some of the current pulses of current $i_2(t)$ are freewheeled through the anti-parallel diode and results in current $i_R(t)$ which is the rectified current as shown in Figure 3.11(b). Figure 3.11(c) shows the conduction path of the current $i_2(t)$.

The average value of the load current $i_L(t)$ for this current control methodology is given by

$$I_L = \frac{\frac{2}{\pi}\widehat{\imath_2} p_{on}}{p_{on} + p_{off}} \tag{3.15}$$

Where $\widehat{\imath_2}$ is the amplitude of the current $i_2(t)$, p_{on} are the number of current pulses that conduct through the load in a period and p_{off} are the number of current pulses that freewheel through the anti-parallel diode in a period.

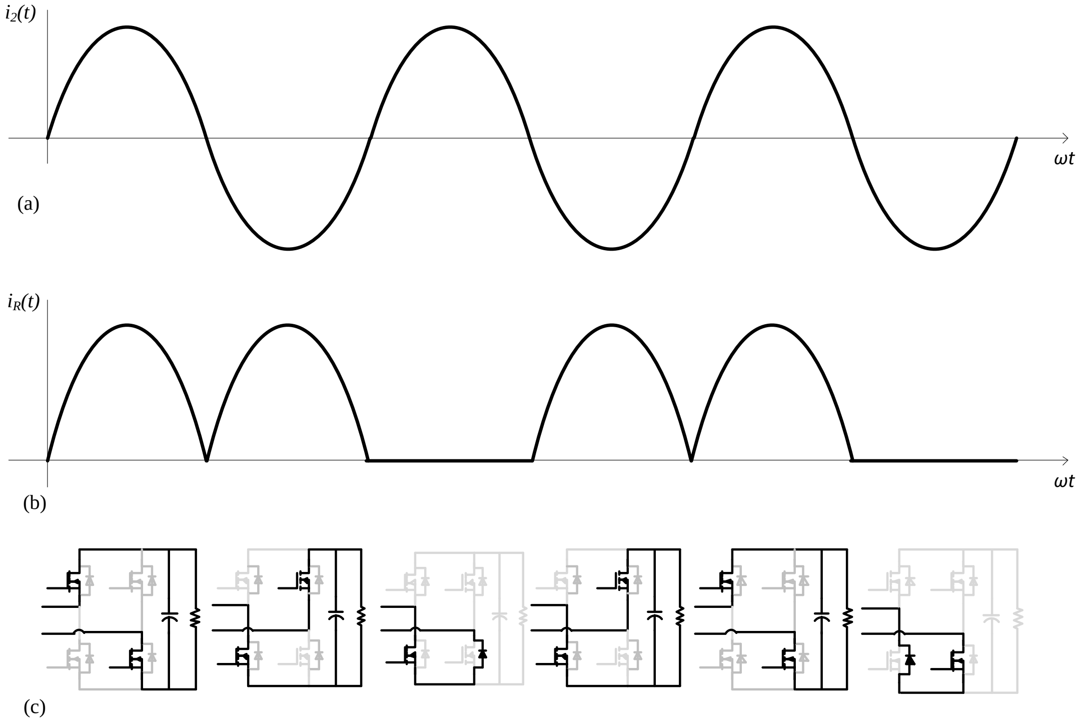

Figure 3.11 a) Current $i_2(t)$ b) Rectified current $i_R(t)$ c) Current conduction path

However, there are some drawbacks to this control strategy. Since, for the durations when current is freewheeling through antiparallel diodes, although there is no current flowing through the load, losses will be incurred because of the current that is circulating in the CPT transformer, the input side inverter and the rectifier circuit.

3.7 Conclusions

In this chapter, power electronic converters for the CPT systems are discussed. Resonant converter topology working at resonance frequency of the designed CPT transformer is best suited for CPT systems. With power transfer efficiency being major criteria for acceptance of this technology, efficiency of the power electronic converts used in a CPT system has been discussed. A novel CPT system has been proposed to increase the overall efficiency of the system using active rectifier which would also eliminate the DC-DC charge control convert used in literature. Theoretical model for output current ripple calculation has been presented for SS resonant converter topology. Load current control has also been discussed. A novel load current control methodology called α –control has been proposed for control of load current from source side. Load current control by controlling the switching of the load side active rectifier is also discussed.

Chapter 4

Experimental Results and Practical Implementation

4.1 Introduction

In previous chapters, analysis and design criteria for a contactless power transfer system are presented along with power electronics requirements of such a system. To start with, the design of the CPT was considered and due to inherent advantages, air cored transformer was chosen as the CPT transformer. In this chapter, firstly, a numerical method is presented to calculate the self inductance of the individual windings and mutual inductance between the windings of a planar CPT transformer. Using this numerical method, for a given number of turns and dimensions of the primary and secondary windings, the self and mutual inductance of the CPT transformer windings are calculated. The values of self and mutual inductances so obtained are then used to design a SS compensated CPT system to feed a resistive load using the design criteria developed in chapter 2. The CPT system is then practically implemented to build an experimental setup to transfer 100W of power over an air gap of 50mm. The effect of misalignment between the CPT transformer windings on the efficiency is also discussed. Practical implementation of CPT technology in on-board energy replenishment is present with the help of a remote controlled car. This car is called Magnetically Induced Charging (MagIC) car.

4.2 Inductance Calculation

Self inductance of a winding can be described by the electromotive force induced in the winding by the change in current in the same winding, due to its own flux linkages whereas mutual inductance between two windings can be described by the electromotive force induced in one winding by change in current in the other winding, due to flux linkages of the other winding. Estimation of self and mutual inductance to a relatively good accuracy is important because these values are used in designing a CPT system.

In this section, a numerical method is presented to estimate self inductance and mutual inductance of planar CPT transform windings using Biot-Savart law. The Biot-Savart law is used to compute the magnetic field due to a steady current.

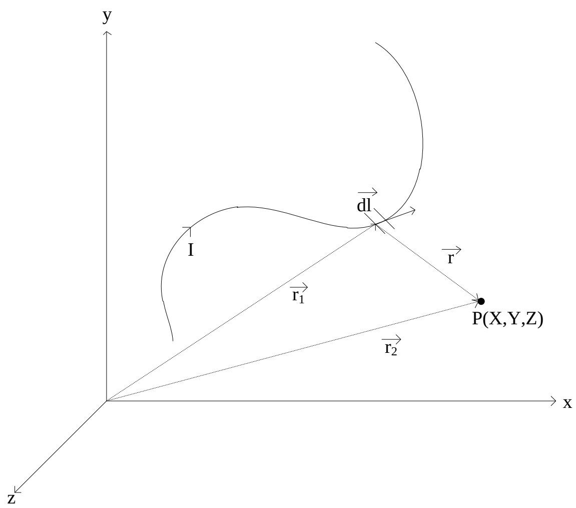

Figure 4.1 Magnetic field vector at point P due to a current carrying conductor

According to the definition of Biot-Savart law,

$$\vec{B} = \frac{\mu_0}{4\pi} \int \frac{I\overrightarrow{dl} \times \hat{r}}{|\vec{r}|^2} \tag{4.1}$$

Where

$\vec{B}$ is the magnetic field at point P,

I is the current flowing through the conductor,

$\overrightarrow{dl}$ is a vector whose magnitude is the length of the differential element of the current carrying conductor and whose direction is the direction of current I,

$\hat{r}$ is the unit vector pointing from the conductor element under consideration towards the point P, at which magnetic field vector is being computed,

$\vec{r}$ is the vector given by $\overrightarrow{r_2} - \overrightarrow{r_1}$; the full displacement vector from the conductor element under consideration to the point P.

4.2.1 Self inductance and mutual inductance calculation

A numerical method is presented for calculating self and mutual inductances of the CPT transformer windings. Although this method can be employed to measure self and mutual inductances of windings of any given geometry, in this thesis, planar square windings are considered. In literature [14][15][16][9], planar circular and rectangular geometries of CPT transformer are most widely studied and although circular geometry is the one having better coupling [6], rectangular geometry is preferred over the circular geometry because rectangular geometry show better tolerance to misalignment between the primary and secondary windings of the CPT transformer [13].

Consider a straight conductor carrying current I along the +ve y axis of length h lying on x-y plane of the coordinate system as shown in Figure 4.2.

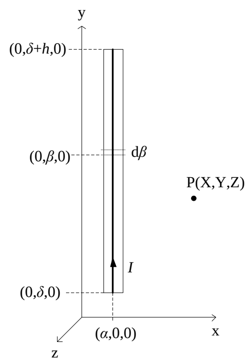

Figure 4.2 Magnetic field at P due to a straight current carrying conductor

Using the Biot-Sarvat law as given by Eq. (4.1), magnetic field vector at point P can be found. The magnetic field vector $\vec{B}$ at point P due a differential element of conductor of length $d\beta$ can be written as

$$\vec{B} = \frac{\mu_0 I}{4\pi} \int_{\delta}^{\delta+h} \frac{(-(X-\alpha)\hat{k} + Z\hat{\imath})d\beta}{((X-\alpha)^2 + (Y-\beta)^2 + Z^2)^{\frac{3}{2}}} \tag{4.2}$$

Where $\hat{\imath}$ and $\hat{k}$ are the unit vectors along x and y axis respectively, and X, Y and Z are the coordinates of the point P. The differential magnetic flux $d\phi$ enclosed by the differential area vector $\overrightarrow{dA}$ is given by

$$d\phi = \vec{B} \cdot \overrightarrow{dA} \tag{4.3}$$

Consider a planar coil with rectangular geometry lying in the x-y plane carrying a current as shown in Figure 4.3. The shaded area in Figure 4.3 represents the total area enclosed by the coil turn. The differential area vector in this case points in the –ve z direction. Therefore the differential magnetic flux can be written as

$$d\phi = \overrightarrow{B_z} \cdot \overrightarrow{dA} \tag{4.4}$$

Where $\overrightarrow{B_z}$ is the z component of the magnetic field vector at any point P lying inside the shaded area. $\overrightarrow{B_z}$ is given by

$$\overrightarrow{B_z} = -\frac{\mu_0 I}{4\pi}\frac{X-\alpha}{(X-\alpha)^2+Z^2}\left(\frac{Y-\delta}{\sqrt{(X-\alpha)^2+(Y-\delta)^2+Z^2}} - \frac{Y-h+\delta}{\sqrt{(X-\alpha)^2+(Y-h+\delta)^2+Z^2}}\right)\hat{k} \tag{4.5}$$

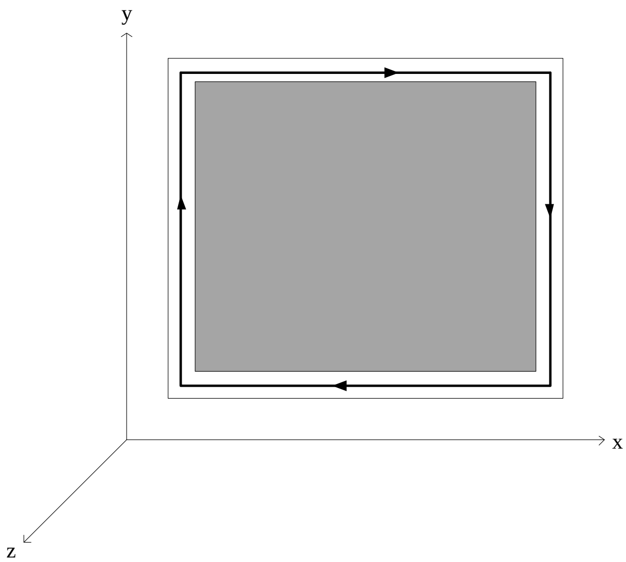

Figure 4.3 Area enclosed by one coil turn

The self inductance of each turn can be found by determining the flux enclosed by that turn due to the current flowing in it. In general, the self inductance of a nth turn of the planar winding under consideration is be given by

$$L_n = \frac{\phi_{nn}}{I} \tag{4.6}$$

Where ϕ_{nn} is the total magnetic flux enclosed by the nth turn due to current I flowing in it.

Similarly mutual inductance between turns of the windings can be found. The mutual inductance between nth and mth turn of the winding is given by

$$M_{nm} = \frac{\phi_{nm}}{I} \tag{4.7}$$

Where ϕ_{nm} is the flux enclosed by the mth turn due to current I flowing in the nth turn of the winding.

The self inductance of a complete winding requires the calculation of self inductance of each turn and the mutual inductance between the turns of the winding. The self inductance of a winding is given by

$$L_{total} = \sum_{n=1}^{N} L_n + \sum_{m=1}^{N} \sum_{\substack{n=1 \\ n \neq m}}^{N} M_{mn} \tag{4.8}$$

Where N is total number of turns in the winding.

Similarly, mutual inductance between the primary and secondary winding can be found. The mutual inductance between the primary and secondary winding is calculated by numerically calculating the magnetic flux enclosed by one due to the current flowing in the other.

4.3 Calculated and measured CPT transformer parameters

Using the numerical method presented, for given dimensions and number of turns of the primary and secondary windings and given air gap between the windings, the self inductance and mutual inductance of the CPT transformer windings was calculated. The CPT transformer with square winding geometry was considered. The diameter of the wire used to construct the windings was chosen to be 2.2 mm. The primary winding with 30 turns and the dimensions of the outermost turn being 180mm X 180mm was considered. The secondary winding with 15 turns and dimensions of the outermost turn being 90mm X 90mm was considered. The air gap between the primary and secondary windings was chosen to be 50mm. The isometric view of these windings is shown in Figure 4.4. A set of windings with the same dimensions, same thickness of coil is constructed using Litz wire as shown in Figure 4.5 (a) and are arranged to form CPT transformer with 50mm air gap between the primary and secondary windings as shown in Figure 4.5 (b).

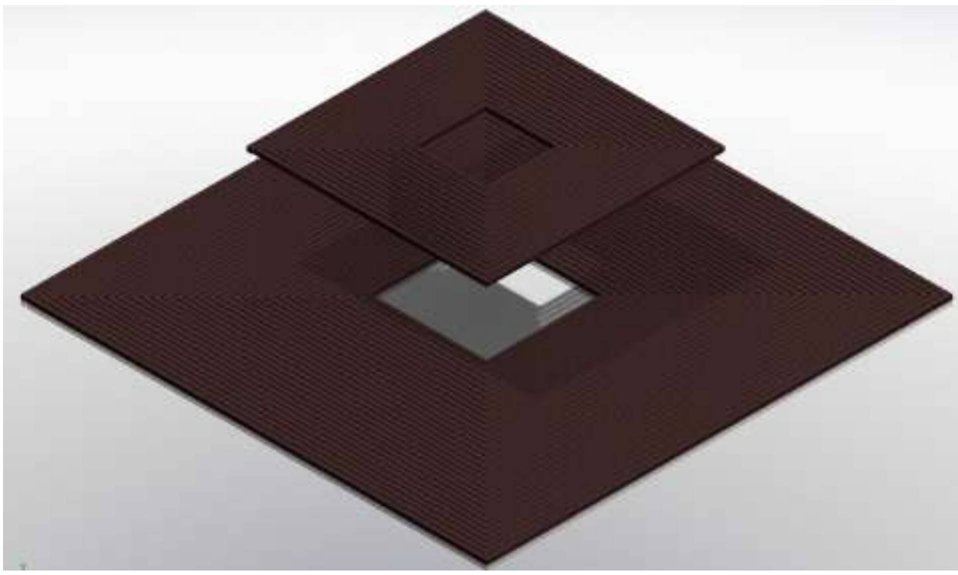

Figure 4.4 Isometric view of the CPT transformer

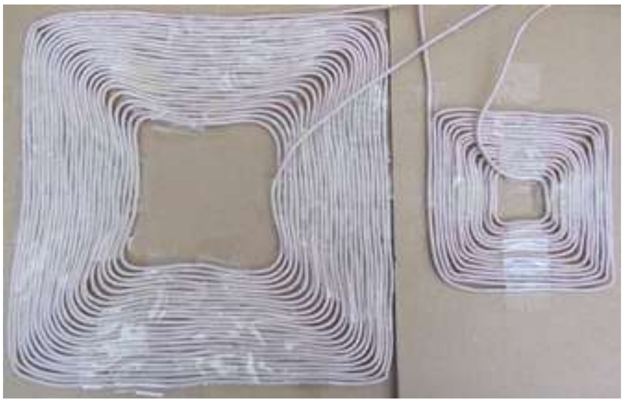

(a)

(b)

Figure 4.5 CPT transformer windings a) Primary and secondary winding b) CPT transformer with 50mm air gap

Following are the calculated and measured parameters of the CPT transformer windings:

Table 4-1 CPT transformer parameters

	Calculated	Measured
Self inductance of primary winding L_1 [μH]	99.2	106.5
Self inductance of secondary winding L_2 [μH]	14.1	15.4
Mutual inductance M [μH]	5.8	6.5
DC resistance associated with primary winding R_1 [Ω]	0.13	0.15
DC resistance associated with secondary winding R_2 [Ω]	0.03	0.04

As evident from the calculated and measured CPT transformer parameters tabulated in Table 4-1, the calculated and measure quantities are off by a significant margin. There are several reasons for that. One of the reasons is that in the case of the numerical calculation, the thickness of the coil was ignored which is only valid when dimensions of the winding are very much greater than the thickness of the coil. The other reason is that the windings made were not perfectly of the same shape and dimensions as intended because the Litz wire has a minimum bending radius and also because of the fact that the windings were manually made and hence some discrepancies in dimensions crept in. However, the numerical method can be used as the first approximation and more accurate techniques like Finite Element Analysis (FEM) can be used to obtain a better estimate.

In the following section, design and analysis of a SS compensated CPT system is presented using the design criteria developed in chapter 2.

4.4 CPT system – analysis and practical implementation

In chapter 2, analysis and design considerations for the four compensated CPT topologies namely SS, SP, PS and PP are presented. Using this design criteria, analysis and practical implementation of a CPT system is presented in this section. Since one of the major objectives of this exercise is to achieve efficient power transfer, achievable efficiency becomes a major factor, apart from other factors discussed in chapter 2, while choosing the compensation topology.

In order to make a comparison based on the achievable efficiency of power transfer, the CPT system parameters have to be well defined. The measured CPT transformer parameters are tabulated in Table 4-1 and are thus well defined. The load is defined to be a resistor of 2.5Ω and a power transfer of 100W is to be achieved to this load. For the parameters so defined, the calculated efficiencies of SS and PS, and PS and PP topologies given by Eq (2.18), Eq. (2.27), Eq. (2.35) and Eq. (2.44), are shown in Figure 4.6 and Figure 4.7 respectively. It is to be noted that while calculating the efficiency as a function of the resonance frequency, the AC resistance of windings as calculated using Eq. (2.3) was considered and losses in the power electronic converters (input side inverter and load side rectifier) were neglected.

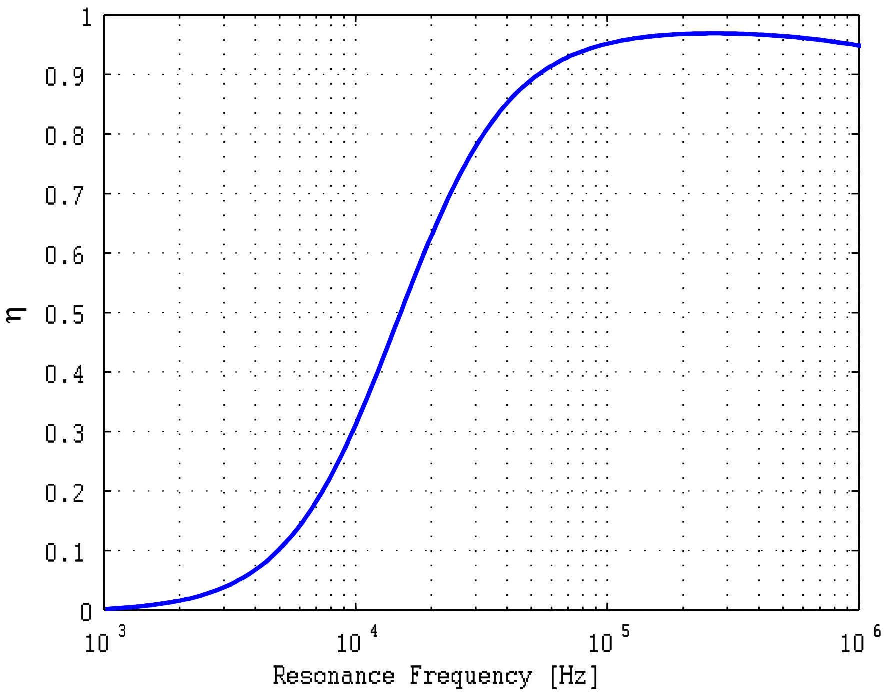

Figure 4.6 Calculated efficiency vs. resonance frequency (SS and PS)

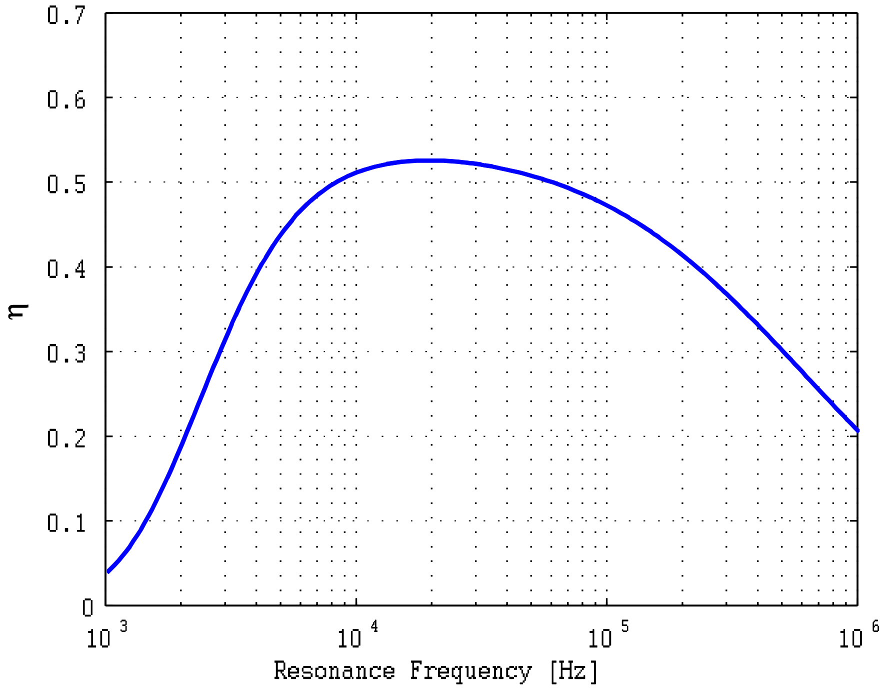

Figure 4.7 Calculated efficiency vs. resonance frequency (SP and PP)

From Figure 4.6 and Figure 4.7 either SS or PS topologies become obvious compensation choices solely based on the achievable efficiency. However, due to other inherent advantages discussed in chapter 2, SS topology was chosen over PS topology. Also, from Figure 4.6, choice of operational frequency, which is equal to the resonance frequency, can be made. The operating frequency was chosen to be 100kHz at which the calculated efficiency is 95.4%. The calculated primary and secondary compensation capacitances for the resonance frequency of 100kHz and measured parameters of the CPT transformer are 23.6nF and 164.5nF respectively.

4.4.1 SS topology – experimental setup

A SS compensated CPT experimental setup is built to illustrate power transfer of 100W over an air gap of 50mm. Figure 4.8 shows the schematic diagram of the CPT system. Figure 4.9 and Figure 4.10 shows the various components of the experimental CPT system.

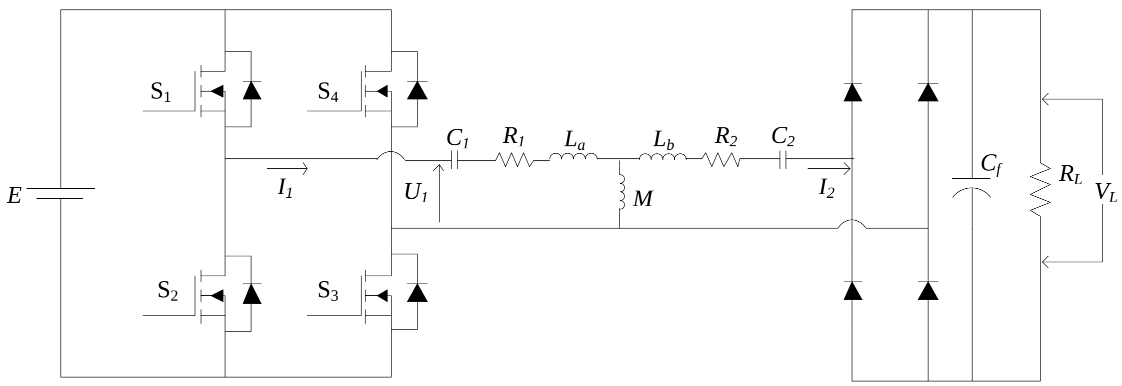

Figure 4.8 Schematic diagram of the experimental setup

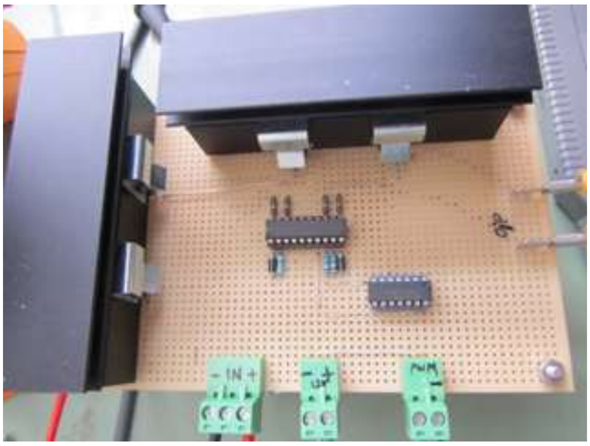

(a)

(b)

(c)

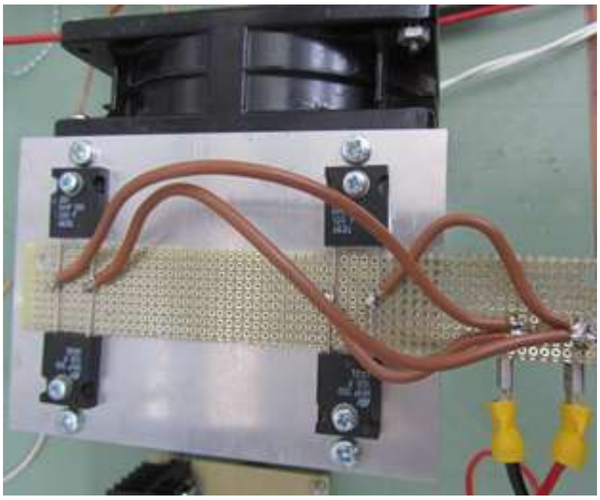

(d)

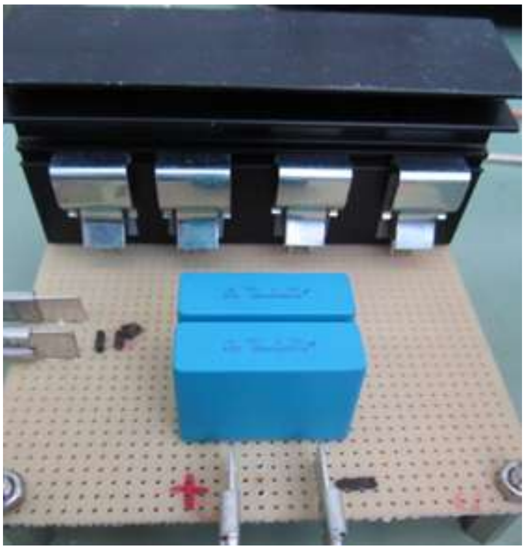

(e)

Figure 4.9 CPT system components a) Input side inverter b) Primary compensation capacitors c) Secondary compensation capacitor d) Resistive load e) Output side rectifier with filter

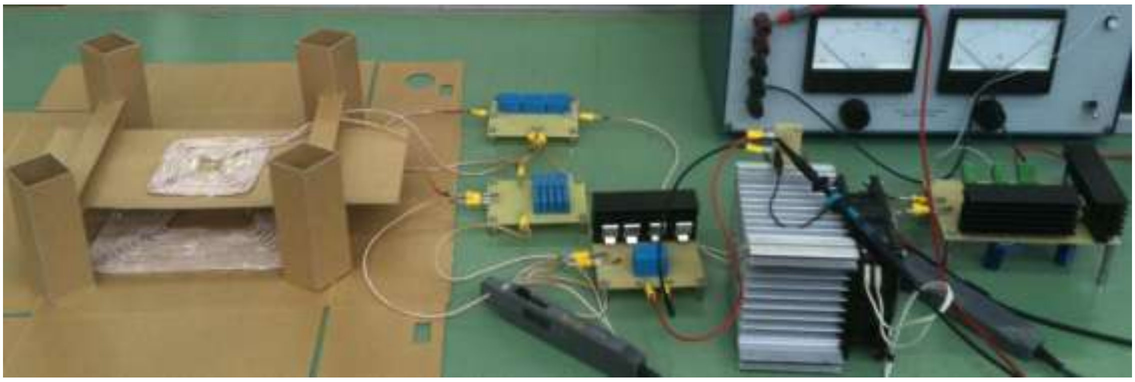

Figure 4.10 CPT system – experimental setup

4.4.2 Adjusted parameters

In the previous section, it was calculated that for the resonance frequency of 100kHz, the primary and secondary windings must be compensated with capacitors of 23.6nF and 164.5nF respectively. However, capacitors with these values are not available in market and so capacitors of 22nF and 170nF were used for primary and secondary compensation respectively were used. Since the primary and secondary compensation capacitors have been adjusted to the values that are practically available, correspondingly the resonance frequency and the input zero phase angle frequency will also change. For the adjusted values of primary and secondary compensation capacitance, Figure 4.11 and Figure 4.12 show the calculated efficiency and the input power factor as a function of operational frequency. From these figures it could be inferred that because of the adjustment, the operational frequency at which maximum efficiency is achievable is different from the zero phase angle frequency. However, the operational frequency is chosen to be 105kHz which is the zero phase angle frequency because at frequency of 100kHz at which maximum efficiency of power transfer is achievable, the input power factor is as low as 0.77 which is not acceptable.

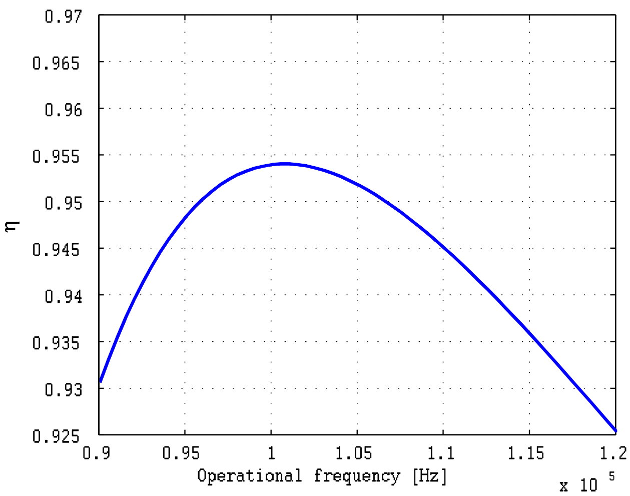

Figure 4.11 Calculated efficiency vs. operational frequency after adjustment

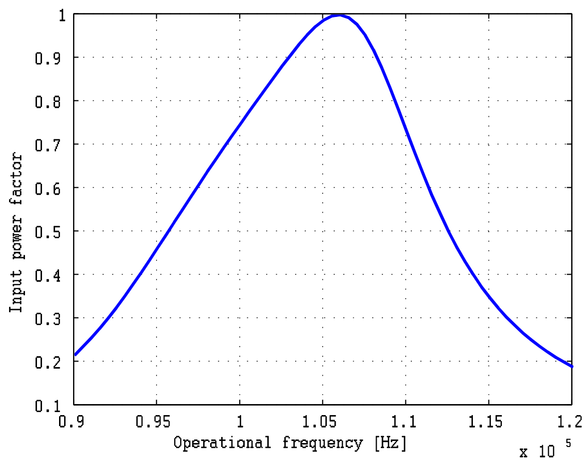

Figure 4.12 Calculated input power factor vs. operational frequency after adjustment

4.4.3 Measured parameters

The parameters of the experimental setup are tabulated in Table 4-2. To calculate the overall efficiency of the CPT system, losses in CPT transformer windings, losses associated with the input side inverter and losses in the diodes used in rectification process are taken into consideration.

Table 4-2 Parameters of the experimental setup

	Calculated (after adjustment)	**Measured**
R_L [Ω]	2.5	2.5
P_L [W]	100	100
V_L [V]	16	16
Operational frequency (zero phase angle)	105	105.6
V_{C1} [V]	289.4	308.5
V_{C2} [V]	55.7	58.2
E [V]	28.1	30.2
I_1 [A]	4.2	4.5
C_f [μF]	30	29
Output voltage ripple	1.13%	1%
% Efficiency CPT transformer	95.2%	91%
% Efficiency overall	89%	83.2%

Figure 4.13 shows the switching characteristics of the input side H bridge inverter. Zero current switching at both turning ON and OFF can be observed. Figure 4.14 and Figure 4.15 shows the various voltage and current waveforms for both non-rectified and rectified output.

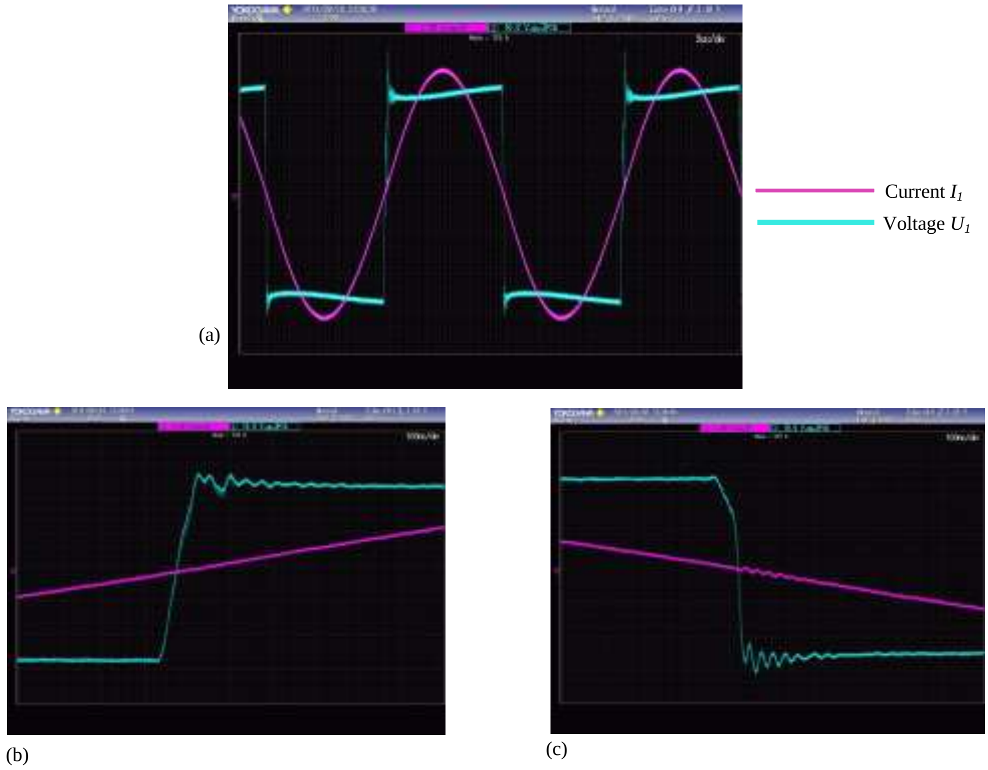

Figure 4.13 Switching characteristics a) Voltage U_1 *and current* I_1 waveforms b) ZCS at turn ON (S1 & S3) and turn OFF (S2 & S4) c) ZCS at turn ON (S2 & S4) and turn OFF (S1 & S3)

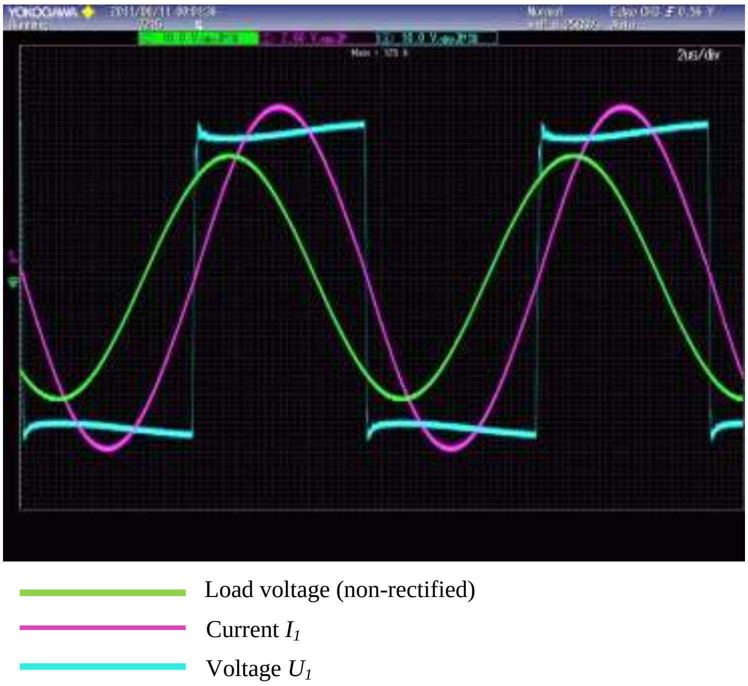

Figure 4.14 Waveforms – non rectified output power

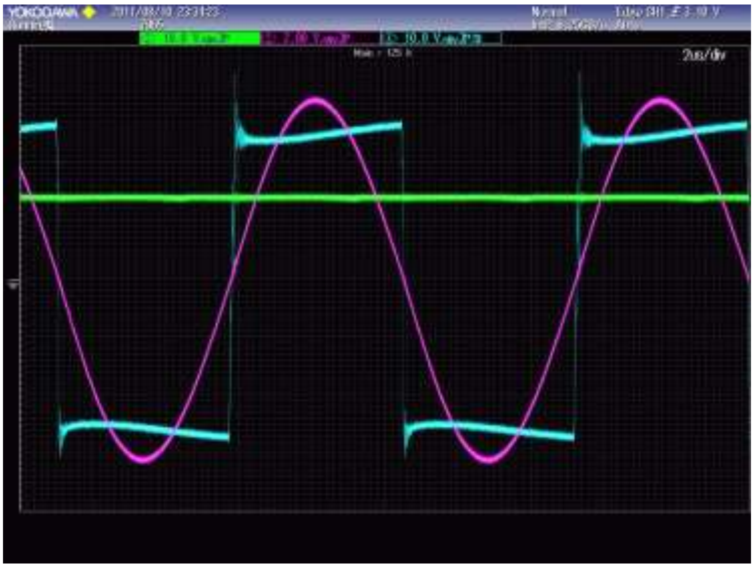

Load voltage V_L (rectified)

Current I_1

Voltage U_1

Figure 4.15 Waveforms – rectified output power

4.4.3.1 Tolerance to misalignment

In many CPT applications, there is a high probability that there would a misalignment between the primary and secondary windings which will lead to reduced system efficiency. In order to study this effect, relative displacement between the primary and secondary windings from the point of maximum mutual inductance (also the point of maximum efficiency) is deliberately introduced and the overall efficiency of the system is measured. Figure 4.16 shows the reduction in efficiency due to the introduced misalignment.

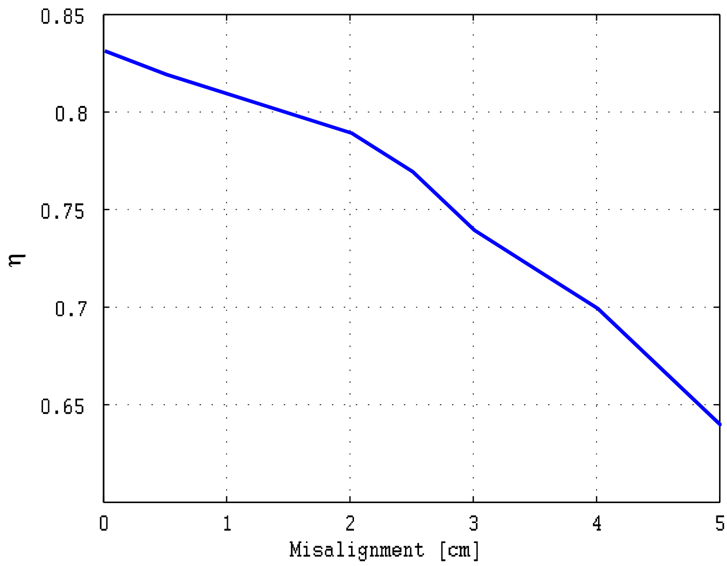

Figure 4.16 Efficiency vs. misalignment of transformer windings

Whenever there is a misalignment between the primary and secondary windings, the mutual inductance between the windings of the CPT transformer would reduce. Because of this reduction in the mutual inductance, the reflected impedance of the secondary on to the primary will also reduce which in turn will lead to higher primary current causing higher resistive losses in the primary winding and hence the reduction in power transfer efficiency is observed.

4.5 Practical implementation - MagIC car

MagIC (Magnetically Induced Charging) car is a remote controlled car built to demonstrated CPT technology for charging using the principles and design parameters developed. A SS compensated CPT system is built to transfer wirelessly the energy to car which is stored in form of electrostatic energy in the super-capacitor bank. These super-capacitors act as the primary energy source for propelling the car. Figure 4.17 shows the side view and top view of the MagIC car.

Figure 4.17 MagIC car

The complete schematic of this car is shown in Figure 4.18. The main components of the MagIC car are MagIC circuit, super-capacitor bank and charge control circuit, and motor controller and RF receiver circuit. In the following sections, descriptions of these components are presented.

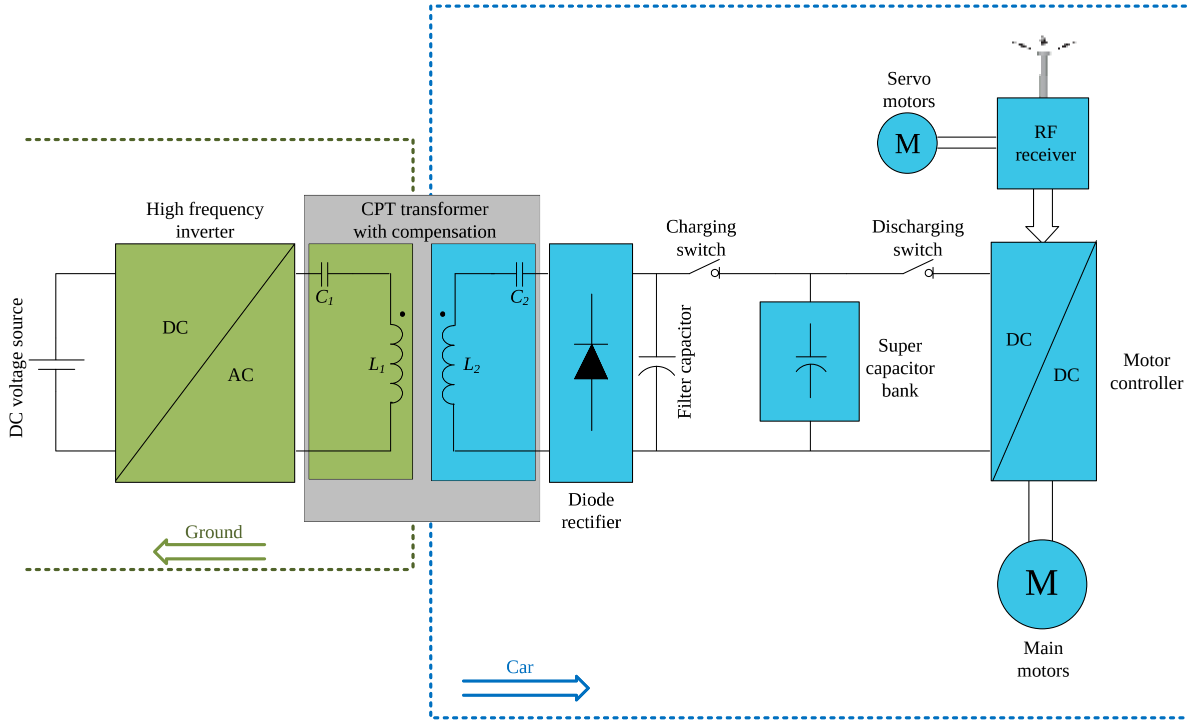

Figure 4.18 Schematic – MagIC car

4.5.1 MagIC circuit

The MagIC circuit consists of CPT system, output rectifier and appropriate filter. Some parts of the MagIC circuit such as input side high frequency inverter, primary compensation and primary winding are present on the ground while some other parts such as secondary winding, secondary compensation and output rectifier with appropriate filter are present on-board the car. The windings of the CPT system are made from Litz wire due to reasons discussed in chapter 2. Figure 4.19 shows the primary and secondary windings housed in acrylic glass casing. The self inductance of the primary and secondary windings was measured to be 112.8 μH and 16.4 μH respectively. It is assumed that the air gap over which the power is to be transferred is 50mm. This means that the distance between the primary winding which is on the ground and the secondary winding underneath the car is 50mm. With this air gap, the mutual inductance between the primary and secondary winding is measured to be 5.2μH. SS topology based compensation is considered for this system. For efficient power transfer to occur, resonance frequency of 100kHz is chosen and hence the primary and secondary compensation capacitance of 20nF and 150nF are used. The input side high frequency inverter is a full bridge inverter with MOSFET switches. The load side rectifier is a full bridge rectifier with Schottky diodes and filter capacitor of 3mF in parallel to the output terminals as shown in Figure 4.18.

Figure 4.19 Primary and secondary windings

4.5.2 *Super-capacitor bank and charge control circuit*

This circuit consists of a super-capacitor bank and two charge control switches which essentially create the path of charge flow. There are two paths of charge flow, one into the super-capacitor bank i.e., the process of charge storage in the super-capacitors and the other is from the super-capacitor bank to the motor controller i.e., the process of discharging of the super-capacitors. The super-capacitor bank consists of 10 super-capacitors of 350F each connected in series, therefore, the equivalent capacitance of the super-capacitor bank is 35F with a maximum voltage rating of 27V (maximum voltage rating of 2.7V across each capacitor). The super-capacitor bank acts as the primary energy source to propel the car. Figure 4.20 shows the super-capacitor bank used. The charging of super-capacitor bank occurs at constant current because of inherent nature of SS compensation topology used and therefore no additional circuitry is required to limit the charging current. The maximum energy that can be stored in the super-capacitor bank is 12.75 kJ which is enough to propel the car for several minutes.

Figure 4.20 Super-capacitor bank

4.5.3 Motor controller and RF receiver circuit

Motor controller and RF receiver circuit consists of DC-DC converter which acts as the motor controller, controlling the speed of the propelling motors on board the car. The control signal for the motor controller comes from a RF receiver. The RF receiver receives signals from the hand held transmitter through which user controls the speed and steering of the car. Two servo motors are used to provide steering torque to the car. The main motors, which are DC motors, provide the propelling torque to the wheels of the car.

4.6 Conclusions

In this chapter, analysis and practical implementation of a SS compensated topology is presented. The numerical method presented to estimate the parameters of rectangular based planar geometry CPT transformer windings is not very accurate but can be used as first step in estimating the transformer parameters. FE analysis method must be employed for a more accurate estimation of the CPT transformer winding parameters.

The measured and calculated parameters of the CPT system are compared and they closely relate to each other. The efficiency of the CPT transformer is measured to be 91% which is close to the calculated efficiency which is 95.2%. Even though Litz wire is used to construct the primary and secondary windings of the CPT transformer, because of the operating frequency which was 105kHz, rise in winding AC resistance due to skin effect was taken into consideration. However, rise in winding AC resistance due to proximity effect, because of geometrical complexity of the windings, was neglected and hence the discrepancy in the calculated and measured efficiency. The overall efficiency of the system, however, was measured to be 83.2% owing to the losses in the inverter stage and especially the rectifier stage. The effect of misalignment between the CPT transformer windings on efficiency of the CPT system is measured and reduction in system efficiency is observed. Lastly, practical implementation of MagIC car is presented. CPT technology is used to charge the on-board super-capacitor bank which acts as the primary energy source.

Chapter 5

Application of CPT in EV Charging

5.1 Introduction

The soaring oil prices and environmental consciousness have provided an impetus for development of electric vehicles as an alternate mode of transportation. However, electric vehicles fail to gain the much needed popularity and acceptance. Limited driving range and long charging time are two major reasons why people are still reluctant to switch to electric vehicles. Also, the existing technology only enables stationary charging which means that an EV has to be stationary during the duration of its charge replenishment. Application of CPT in charging of EVs has the potential of bringing about a paradigm shift in how the EVs are perceived today. CPT makes the charging process more convenient and safe by eliminating the need for physical contacts and manual plugging in to the charging point. Since there are no galvanic connections formed when charging electric vehicle contactless, charging can also be accomplished when the vehicle is in motion and not just when it is parked. This may lead to increased driving range or lower on-board battery size or both.

In this chapter, with special emphasis on Battery Electric Vehicles (BEV), application of CPT technology in charging of BEVs is studied. The capacity of the battery pack, efficiency of drive-train and electric motors determine the range of a BEV with capacity of the battery pack being the most important factor among the three. Unlike in conventional vehicles, the present commercially available BEVs cannot be replenished with energy quickly enough. In this chapter an overview of the existing and upcoming BEV energy storage technology is presented with emphasis on charging technologies and state-of-the-art of battery technology. Concept of on-road charge replenishment is introduced in this chapter. With the help of two case studies, driving range enhancement with on-road charging in urban and highway conditions is studied. In the later parts of this chapter, battery charging characteristics of the BEV under consideration are presented. An estimation of cost of a CPT system for various power levels is also discussed.

5.2 Battery technology

Battery is a key component in any BEV. To this date it is the only device that can store so much of energy so as to give a vehicle a reasonable driving range. The most popular batteries in usage to this day are the lead acid batteries. Although a lot is known about these batteries in terms of technology, these batteries are not suitable for EV application. One of the main reasons for this is that its specific energy is limited to about 40 Wh/kg making it impossible to achieve a driving range of few hundreds of kilometres.

Nickel metal hydride (NiMH), Sodium metal chloride (ZEBRA) and Lithium ion (Li-ion) are the other vastly used batteries in today's EVs.

5.2.1 Nickel metal hydride (NiMH)

NiMH batteries have almost double the specific energy when compared to lead acid batteries. These batteries are quite famous with EV manufactures and the most famous of IC hybrid vehicles, like Toyota Prius, employ these batteries. However, the specific energy of these batteries is not high enough for these to be installed in more energy intensive vehicles like plug-in hybrid vehicles (PHV) and BEVs.

5.2.2 Sodium metal chloride (ZEBRA)

Zero Emissions Battery Research Association (ZEBRA) belongs to family of sodium based batteries. Optimum performance of this battery is obtained at relatively high temperatures of 270-350 ^{o}C and therefore additional components are required to be installed on-board the EV to make optimum use of these batteries. These batteries have moderately high specific energy of about 103 Wh/kg [24] which makes them suitable for PEVs and BEVs. These batteries are specifically tested for automotive applications and are commercially available. However, their specific power is not very high and charging time can be long.

5.2.3 Lithium ion (Li-ion)

Li-ion technology is the most promising battery technology among the three so far discussed. They have been used extensively in portable electronics, but higher power packs are being developed by several companies, trying to meet the expectations of the many car manufacturers willing to have them as the main electric energy storage devices in PHVs and BEVs. Lithium-based batteries can also be designed to have high specific power, and prototypes have been built allowing for very quick recharge. However, cost of these batteries is too high to be readily accepted by the automobile manufactures.

In Table 4-1, basic parameter indices of battery technology so far discussed are tabulated and their respective Ragone plots (energy versus power in logarithmic scale) are shown in Figure 5.1. All figures have a significant spread on the Ragone plot which could be because of particular technological process and energy/power trade off of a particular battery.

Table 5-1 Nominal parameters of some battery technologies

	Lead acid	NiMH	ZEBRA	Li-ion
Specific energy (Wh/kg)	30-40	50-80	103	100-250
Energy density (Wh/l)	50-90	150-200	180	150-250
Specific power (W/kg)	250	<1000	180	<2000
Nominal cell voltage (V)	2.1	1.2	2.58	3.6
Number of cycles @80% DOD	700	2000	1500	2000

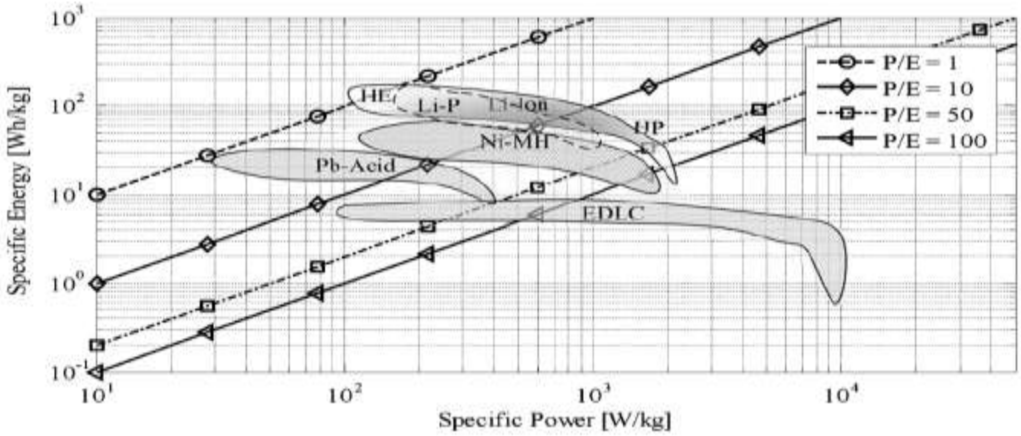

Figure 5.1 Ragone plot of several battery types [25]

5.3 Charging technology

Today's conventional internal combustion engine vehicles can be easily replenished with energy by refilling the fuel which can be done in few minutes. This, however, is not the case with BEV's. A BEV can take anywhere from several minutes to few hours to replenish its energy depending upon the charging power and capacity of the batteries. The Society of Automotive Engineers has come up with battery charging standards for EVs which are presented in this section.

5.3.1 SAE J1772

SAE J1772 is standard for charging of batteries has been established by SAE EV charging system committee. According to these standards, charging levels fall into 3 categories depending upon the power. AC level 1 and AC level 2 charging electric vehicle supply equipment (EVSE) be located on board and DC charging EVSE must be located off-board [27]. Figure 5.2 shows the EV charging system architecture as prescribed by SAE J1772.

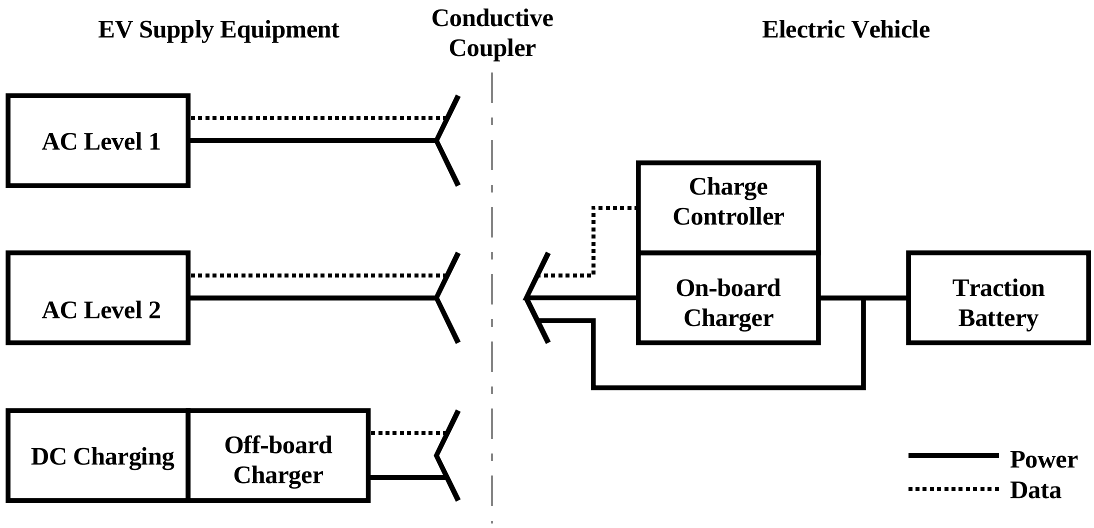

Figure 5.2 EV Charging architecture [26]

5.3.1.1 AC level 1

AC level 1 charging uses 120 VAC, 15/20 A, National Electrical Manufacturers Association (NEMA) connector. This configuration would enable a power transfer of 1.9 kW [27]. This means that a Nissan leaf electric car which a battery capacity of 24 kWh can be replenished from 20% charge to 100% charge in about 10 hrs. So, the disadvantage of an AC level 1 charging is that it takes long time to charge the batteries. But, this charging system coasts the least when compared to other two charging schemes.

5.3.1.2 AC level 2

AC level 2 charging uses 208-240 VAC, 80 A connector. This configuration enables a power transfer of 19 kW [27]. This means that the same Nissan leaf electric car can be replenished from 20% charge to 100% charge in about 1 hr. AC level 2 charger charges the batteries comparatively faster than the AC level 1 charger but cost of an AC level 2 chargers will be considerably more than an AC level 1 charger.

5.3.1.3 DC charging

DC charging is a fast charging scheme which would allow power upward of 100 kW [27]. This scheme would employ off-board charging equipment which would directly connect to the vehicle high voltage DC bus. This means that the same Nissan leaf electric car which was considered earlier can be replenished from 20% charge to 100% charge in about 10-15 minutes. However, this charging scheme is limited by the fact that the infrastructure required to accomplish this fast charging will be quite expensive. Charge limitations of a battery and safety concerns are other factors that would limit the use of this scheme.

Other than the above mentioned charging schemes, some auto manufacturers are also considering replenishment of energy by replacing the discharged batteries by charged batteries. In this business model, an EV would get its batteries replaced by driving into a battery replacement station.

5.4 Case study

The idea of CPT for EV charging application is not new but a lot of research is being pursued in this topic to find innovative solution which could lead to change in mindset of consumers toward EV technology by enhancing the range of EVs and making charging process simpler with respect to human interaction. CPT systems can be installed at homes, work places and public parking facilities, and would make it more convenient for users to charge their EVs without the need of physically connecting wires to the charging points. An innovative use of a CPT system could be to replenish the battery charge in an EV when on road. A CPT system installed underneath the roads would make it possible to replenish charge in EVs either on move, in case of a highway setting, or when stationary for some time at traffic signals, in case of urban setting. To study the effect of on-road charge replenishment on driving range of EVs, energy usage of an EV has to model in such a way that it can be clubbed with a battery model which will provide a good estimate of battery performance. To accomplish this, vehicle and battery models are presented to replicate energy usage.

5.4.1 Vehicle model to replicate energy usage

The operational range of a BEV depends upon capacity of battery and the driving conditions. To determine the quantity and rate of energy transferred to and from a battery during driving conditions, a model that computes the energy needed to propel a typical vehicle is constructed. The simulated vehicle is a typical mid-size BEV [28]. The parameters of this BEV are tabulated in Table 5-2.

Table 5-2 Parameters of simulated BEV

Vehicle	**Mass**	1600 kg
	Frontal area	2.7 m^2
	Co-efficient of rolling resistance	0.01
	Co-efficient of drag	0.28
Battery	**Current capacity**	90 Ah
	Energy capacity	24 kWh

The power requirement of a vehicle has following components [29]

- Base load P_{base} which consists of all on board electronic load. P_{base} is taken to be 800 W on account of the power needed for all activities unrelated to movement such as heater, air conditioner, radio, signals and other accessories [30].

- Rolling resistance P_{roll} which is due to resistance offered by road to rolling motion of the wheels. P_{roll} is given by $C_{rr}mg\cos\theta|v|$ where C_{rr} is the co-efficient of rolling resistance, m is the mass of the vehicle, g is acceleration due to gravity, θ is the angle of inclination and v is the instantaneous velocity of the vehicle.
- Aerodynamic drag P_{drag} which is due to resistance offered by air. P_{drag} is given by $1/2C_d\rho|v|^3 A$ where C_d is the co-efficient drag, ρ is the density of air taken as 1.23 kgm^{-3} and A is the frontal area of the vehicle.
- Gravitational load P_g which is due to uphill/downhill driving. P_g is given by $mg\sin\theta|v|$.
- Inertial load P_{acc} which is due acceleration/braking. P_{acc} is given by $ma|v|$ where a is the instantaneous acceleration of the vehicle.

$$P_{load} = P_{base} + P_{roll} + P_{drag} + P_g + P_{acc} \tag{5.1}$$

Of all the loads mentioned above, apart from the base load, all other loads are dependent on velocity and/or acceleration of the vehicle. Also, P_g and P_{acc} could be positive or negative depending upon angle of inclination (which is positive when driving uphill and negative when driving downhill) and acceleration (which is positive when accelerating and negative when braking). There are certain assumptions made when building the model to calculate power flow to or from the battery of the BEV. These assumptions are as follows

- The electric drive train (electric motor, converter and transmission system) is assumed to have an overall efficiency of 80%
- The efficiency of power transfer from wheels to batteries during regenerative braking is assumed to be 40%
- The initial SOC of batteries is assumed to be 80%
- Since there is no information about the angle of inclination of the road, it is assumed that the angle of inclination of road though-out the journey in all driving cycles under consideration to be zero i.e., $\sin\theta = 0$ and $\cos\theta = 1$. This means P_g=0
- The overall efficiency of power transferred to a BEV via CPT system is assumed to be 80%

5.4.2 Battery model

To design the drive system of an electric vehicle, it is necessary to have a model that describes the electric behaviour of a battery. In literature researchers have come up with many battery models. There are many factors that determine the performance of a battery and therefore to predict behaviour of a battery, in literature many battery models exist. Some of the important factors that determine the behaviour and performance of a specific kind of battery are State of charge (SOC), Battery storage capacity, Rate of charge/discharge, Temperature, age of the battery. Depending upon the specific purpose of the battery model, degrees of complexity of these models vary. Electrochemical models, Mathematical models and Electrical equivalent models are some of the most widely researched battery models available in literature.

Electrochemical models [31][32][33] are mainly used to optimize the physical design aspects of batteries characterizing fundamental mechanism of power generation. This model takes into consideration both microscopic and macroscopic information like battery voltage and current, and concentration distribution respectively. These models are complex because they model the behaviour of a battery from first principles and requires good understanding of material, electrochemistry, chemical reactions and thermodynamics.

Mathematical models [34][35][36], are too abstract to attach any practical meaning. These models adopt empirical equations or mathematical methods like stochastic approaches to predict system-level behaviour, such as battery runtime, efficiency, or capacity. However, mathematical models cannot offer any I–V information that is important to circuit simulation.

Electrical models [37][38][39], are equivalent electrical circuit models using a combination of voltage sources, resistors, and capacitors for design and simulation with other electrical circuits and systems as in case of an EV performance simulation. Electrical models are more intuitive, useful, and easy to handle, especially when they can be used in simulators like MATLAB SIMULINK. There are many electrical models of batteries, from lead-acid to polymer Li-ion batteries. The simplest of equivalent electrical model is as shown in Figure 5.3. Such a circuit is apparently very simple, but in order for it to describe accurately the behaviour of a real battery, both the open circuit voltage (indicated as $V_{B,OC}$) and the internal resistance (indicated as $R_{i,B}$) must change according to the state of charge (SOC) of the battery. This is true for all battery technologies, even though the dependency may be very different according to the particular chemistry and technology. The battery model simulated used to study the behaviour of the battery has been extensively covered in [40].

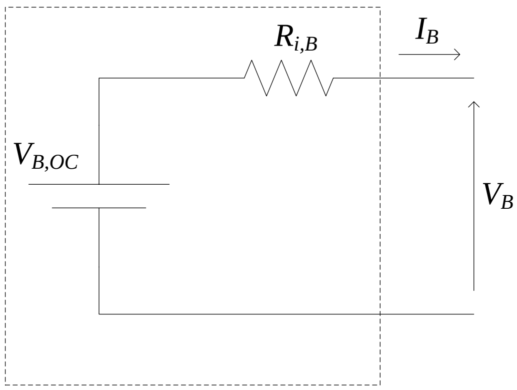

Figure 5.3 Basic Thevenin equivalent battery model

Some of the most modern full-sized commercially manufactured BEVs like Tesla Roadster, Mitsubishi i MiEV, Nissan Leaf etc. are Li-ion battery powered, so, Li-ion battery is simulated as the power source of the EVs to model energy usage.

In the battery model used, effects of certain parameters have not been taken into consideration. The dependency of battery performance on the cell temperature has been neglected. The model is also unable to predict the dynamic behaviour of the battery as the pseudo-capacitance effects are neglected. Also, the effects due to the aging of the battery are neglected. The model used in the simulations can predict the performance of a vehicle in terms of range to a reasonable accuracy, so, more complex electrochemical models and mathematical models are not considered.

5.4.3 Case Study 1: Urban driving cycle

In case study 1, it is studied how CPT system when installed underneath the roads at traffic signals would enhance the range of a BEV. To simulate this, three standard urban driving cycles are considered. These are the tests patterns which manufacturers have to refer to while stating their vehicles performance in terms of range and emission. These are

- U.S. standard FTP 72 (Federal Test Procedure) cycle also called Urban Dynamometer Driving Schedule (UDDS)
- European standard ECE-EUDC combined urban test cycle
- Japanese standard JC08 urban test cycle

Some characteristics of these urban test cycles under consideration are tabulated in Table 5-3. It is assumed that the time a vehicle spend idling during a journey in a test cycle is the time for which the vehicle has stopped at traffic signals.

Table 5-3 Characteristics of UDDS, ECE-EUDC and JC08 driving cycles

Cycle	**Duration (s)**	**Distance travelled (km)**	**Average speed (kmph)**	**Maximum speed (kmph)**	**Idle time from start to end of journey (s)**	**% Time spent idling**
UDDS	1369	12.0	31.5	90.9	234	17.1
ECE-EUDC	1180	11.0	33.5	120	261	22.1
JC08	1204	8.2	24.4	81.6	330	27.4

5.4.3.1 UDDS cycle

Figure 5.4 and Figure 5.5 show the speed of a vehicle and distance covered by the same vehicle as a function of time respectively in UDDS cycle. The idle time indicated in Figure 5.4 is assumed to be the time the vehicle is stationary at traffic signals.

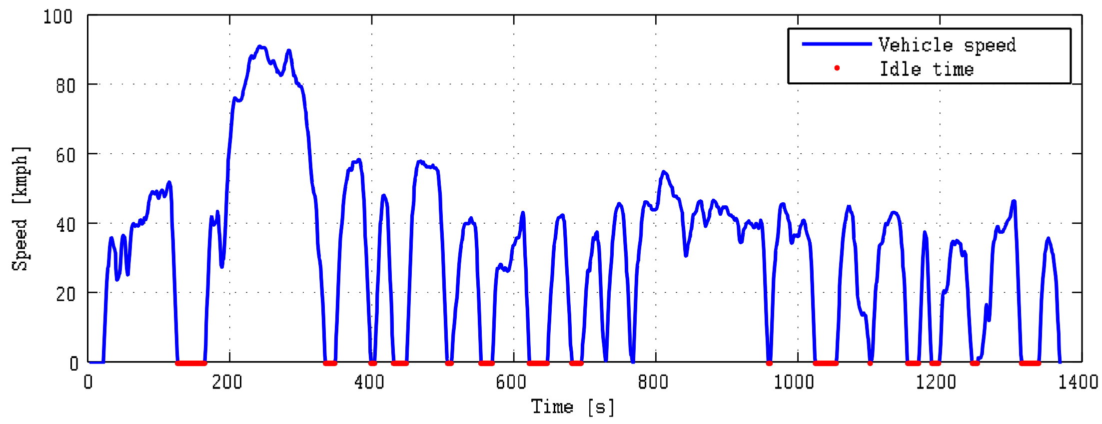

Figure 5.4 Vehicle speed as a function of time (UDDS)

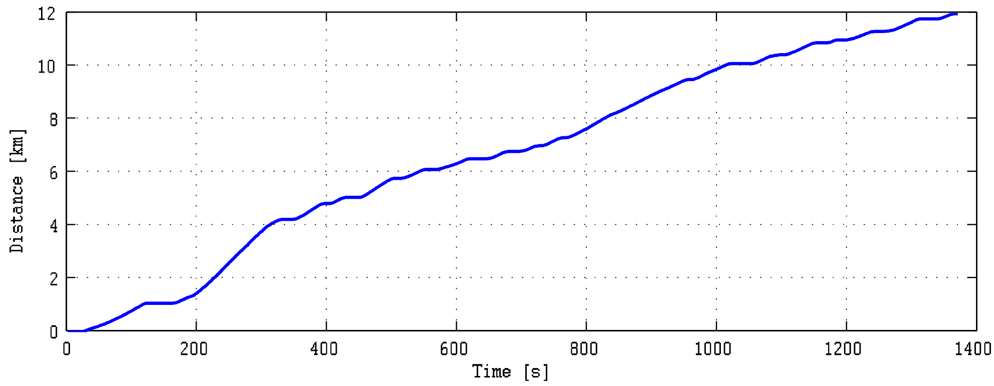

Figure 5.5 Distance covered by vehicle as a function of time (UDDS)

Figure 5.6, Figure 5.7 and Figure 5.8 show the power flow from the battery, battery terminal voltage and current flow from the battery as a function of time respectively. The negative power in Figure 5.6 represents the power that flows to the battery during regenerative braking when the vehicle decelerates. Corresponding effect of regenerative braking can be seen on the terminal voltage of the battery and battery current in Figure 5.7 and Figure 5.8 respectively. Figure 5.9 shows the SOC of the battery as a function of time during the journey.

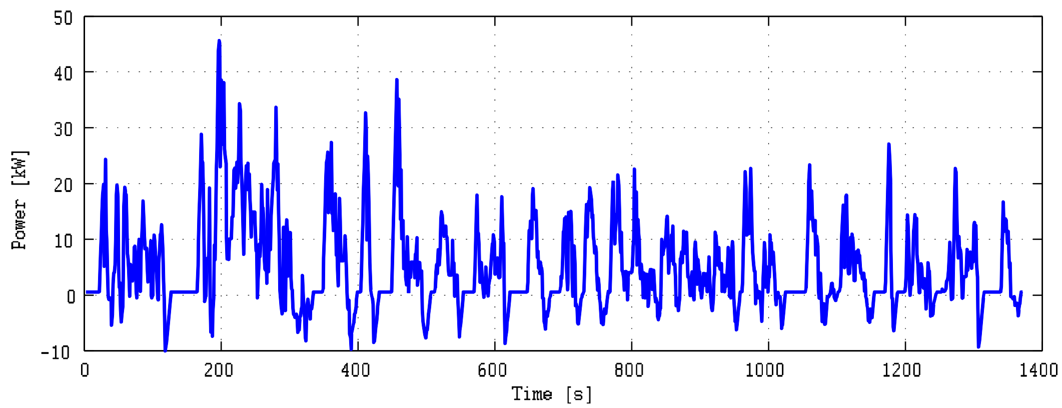

Figure 5.6 Power flow from battery as a function of time (UDDS)

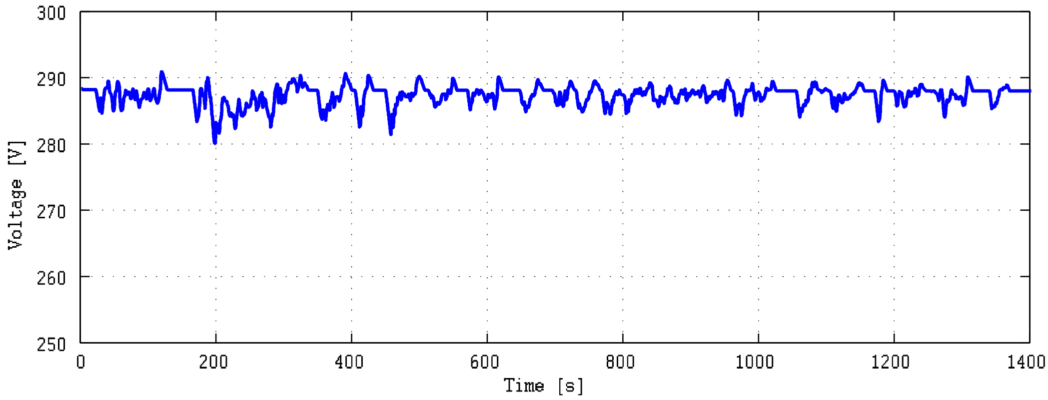

Figure 5.7 Battery terminal voltage as a function of time (UDDS)

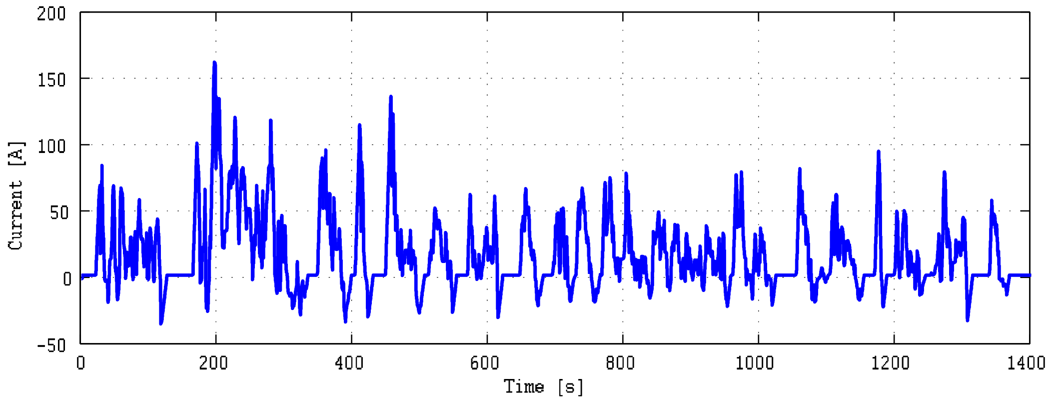

Figure 5.8 Current flow from battery as a function of time (UDDS)

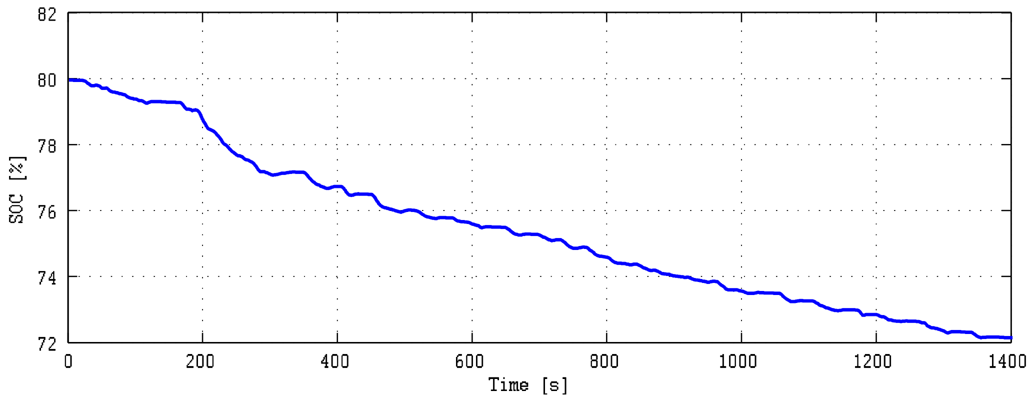

Figure 5.9 SOC of battery as a function time (UDDS)

5.4.3.2 ECE-EUDC cycle

Figure 5.10 and Figure 5.11 show the speed of a vehicle and distance covered by the same vehicle as a function of time respectively in ECE-EUDC cycle.

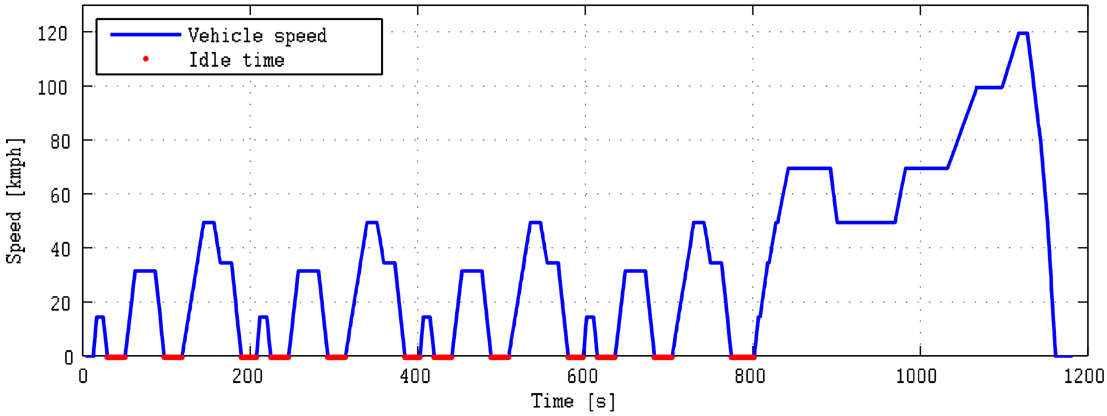

Figure 5.10 Vehicle speed as a function of time (ECE-EUDC)

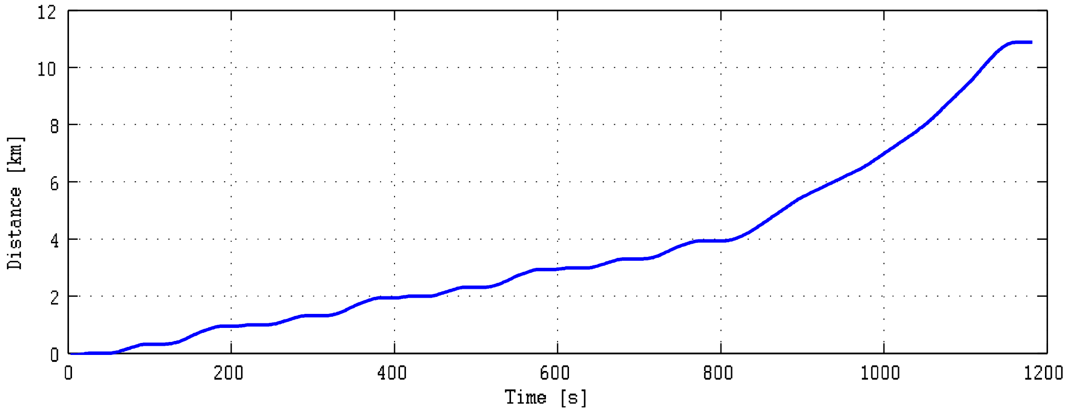

Figure 5.11 Distance covered by vehicle as a function of time (ECE-EUDC)

Figure 5.12, Figure 5.13 and Figure 5.14 show the power flow from the battery, battery terminal voltage and current flow from the battery as a function of time respectively. Figure 5.15 shows the SOC of the battery as a function of time during the journey.

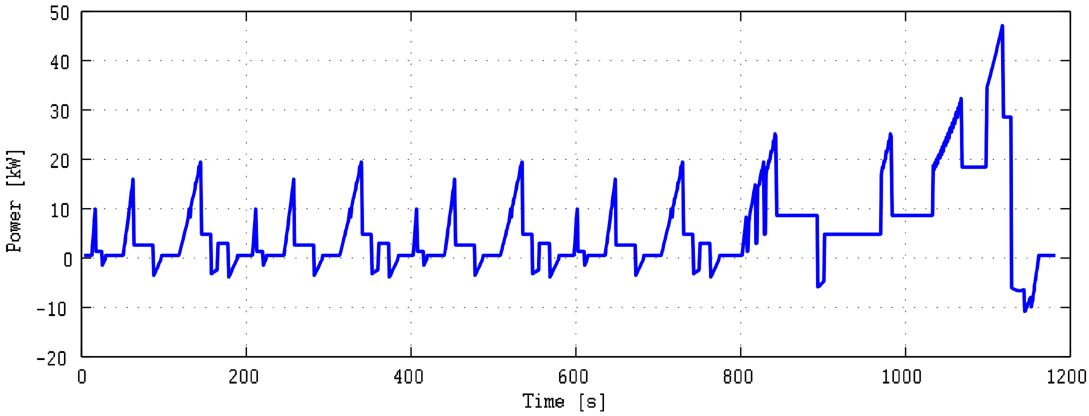

Figure 5.12 Power flow from battery as a function of time (ECE-EUDC)

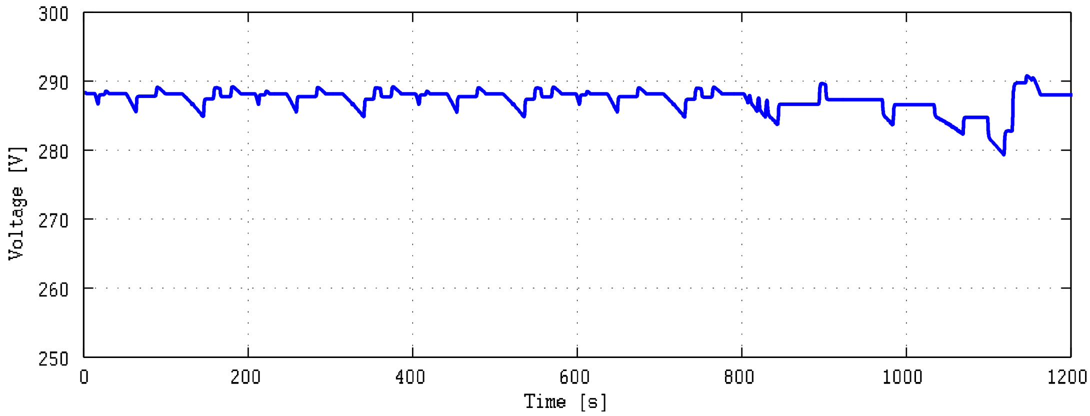

Figure 5.13 Battery terminal voltage as a function of time (ECE-EUDC)

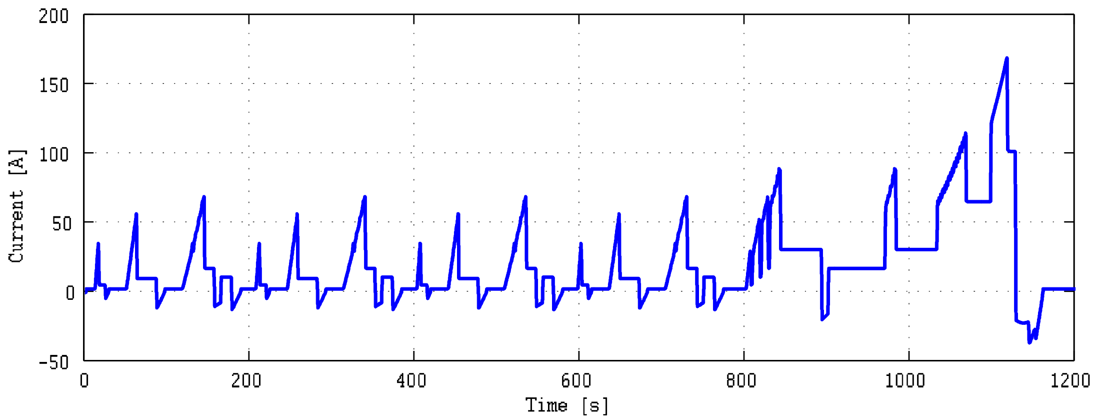

Figure 5.14 Current flow from battery as a function of time (ECE-EUDC)

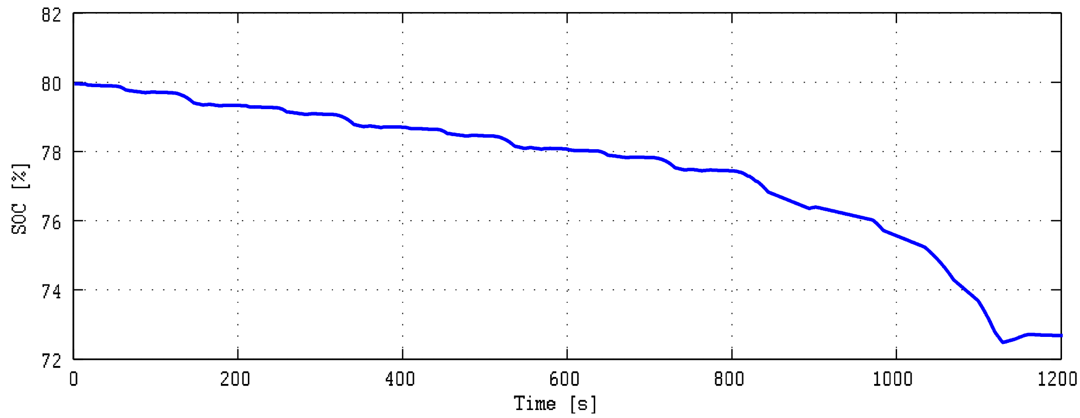

Figure 5.15 SOC of battery as a function time (ECE-EUDC)

5.4.3.3 JC08 cycle

Figure 5.16 and Figure 5.17 show the speed of a vehicle and distance covered by the same vehicle as a function of time respectively in JC08 cycle.

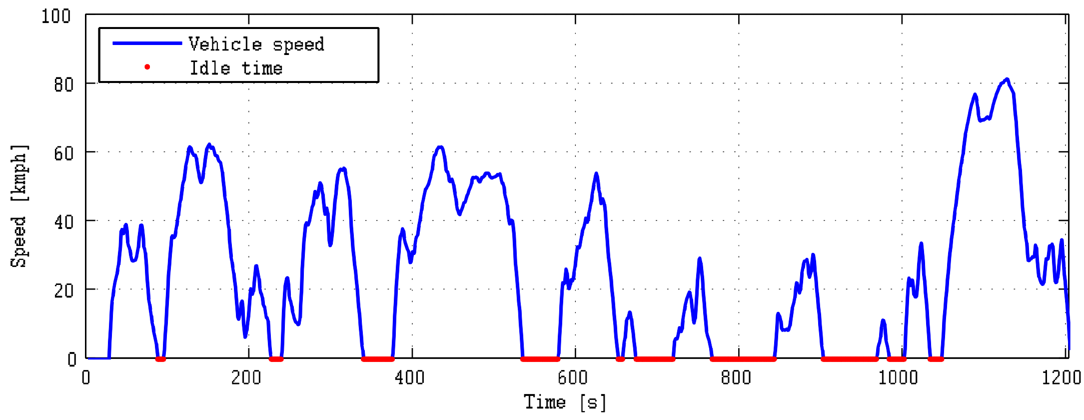

Figure 5.16 Vehicle speed as a function of time (JC08)

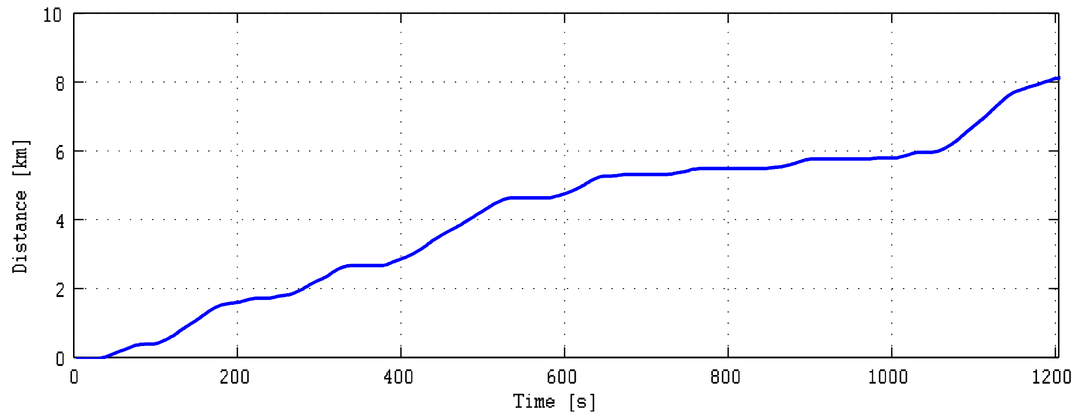

Figure 5.17 Distance covered by vehicle as a function of time (JC08)

Figure 5.18, Figure 5.19 and Figure 5.20 show the power flow from the battery, battery terminal voltage and current flow from the battery as a function of time respectively. Figure 5.21 shows the SOC of the battery as a function of time during the journey.

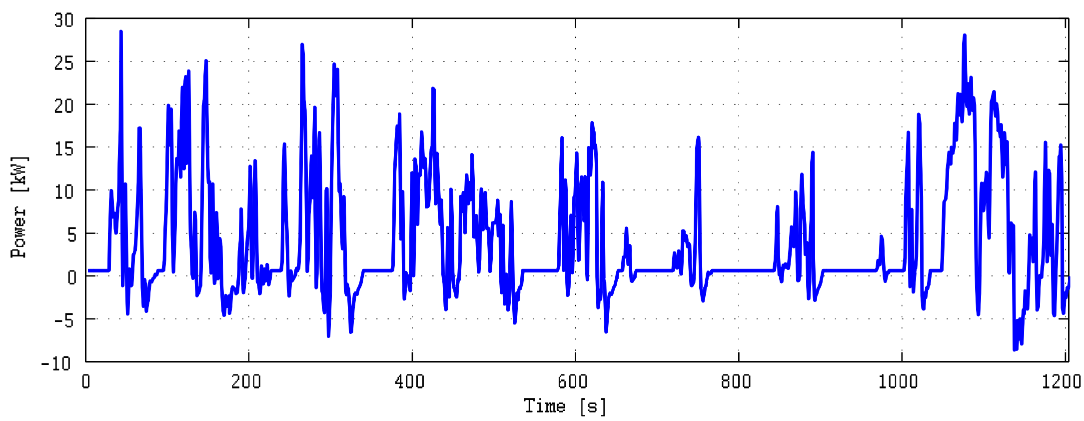

Figure 5.18 Power flow from battery as a function of time (JC08)

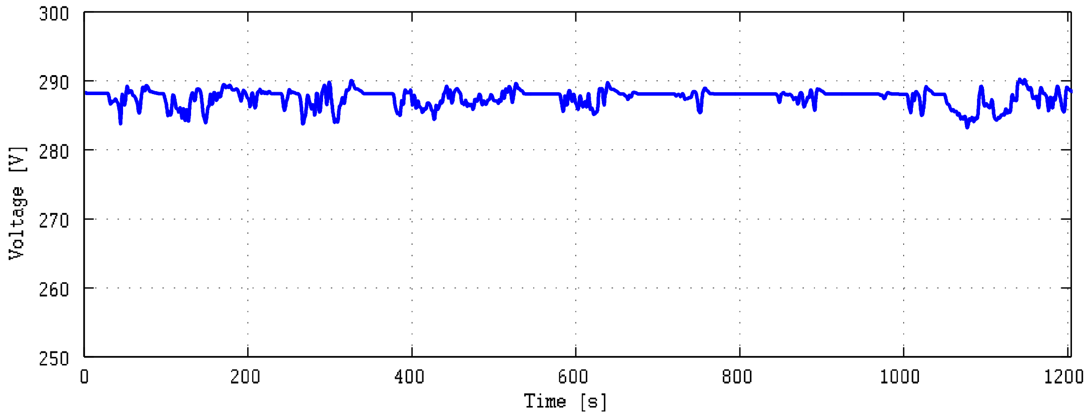

Figure 5.19 Battery terminal voltage as a function of time (JC08)

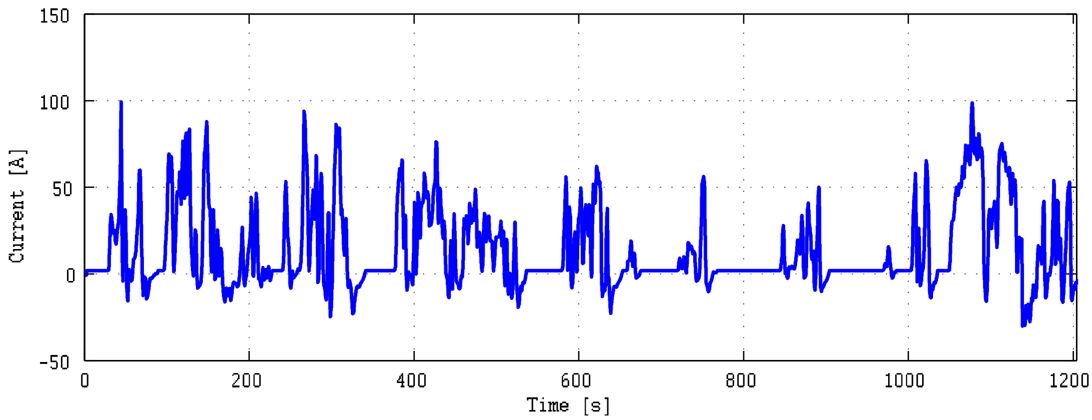

Figure 5.20 Current flow from battery as a function of time (JC08)

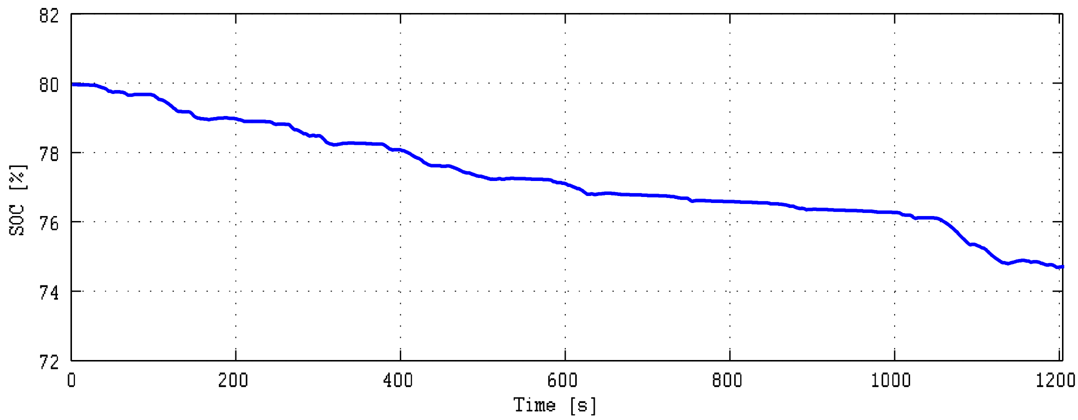

Figure 5.21 SOC of battery as a function of time (JC08)

The ECE-EUDC cycle is a rather simple pattern consisting of periods of constant acceleration, constant deceleration and constant speed. This cycle, however, is not a true resemblance of actual driving conditions in an urban scenario. It is presented here, as these are standards with which European car manufacturers have to refer when stating their vehicle's performance in terms of achievable range and emissions. On the other hand UDDS and JC08 cycles are derived from actual urban driving data which exhibits continuously varying speed over the entire driving cycle.

5.4.3.4 CPT at traffic signals

CPT systems are installed at traffic signals which will replenish the battery charge when the vehicle is stationary at these traffic signals. These periods are indicated as 'idle time' in Figure 5.4, Figure 5.10 and Figure 5.16 in UDDS, ECE-EUDC and JC08 cycles respectively. It is assumed that CPT systems at different traffic signals in the driving cycle under consideration are identical in terms of power rating. So, depending upon the time a vehicle is stationary at a traffic signal and the power rating of the installed CPT system, the amount of energy replenished to the battery varies. To determine the effect of power transferred via CPT system on the SOC of the battery, CPT systems with varying amount of power transferred are incorporated in vehicle–battery energy model. Figure 5.22, Figure 5.23 and Figure 5.24 show the SOC of the battery as function of time with power transferred via CPT system varying from 0 W to 40 kW for UDDS, ECE-EUDC and JC08 cycles respectively.

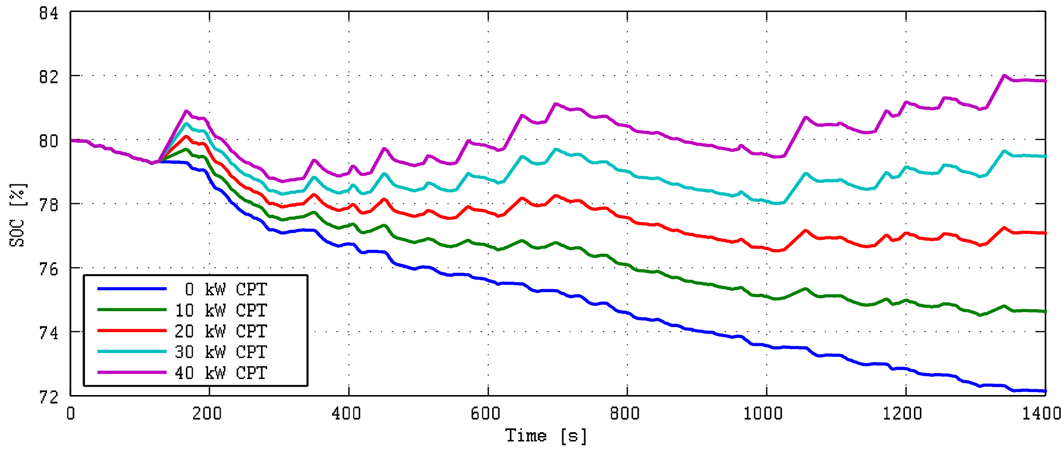

Figure 5.22 SOC of battery as a function of time (UDDS)

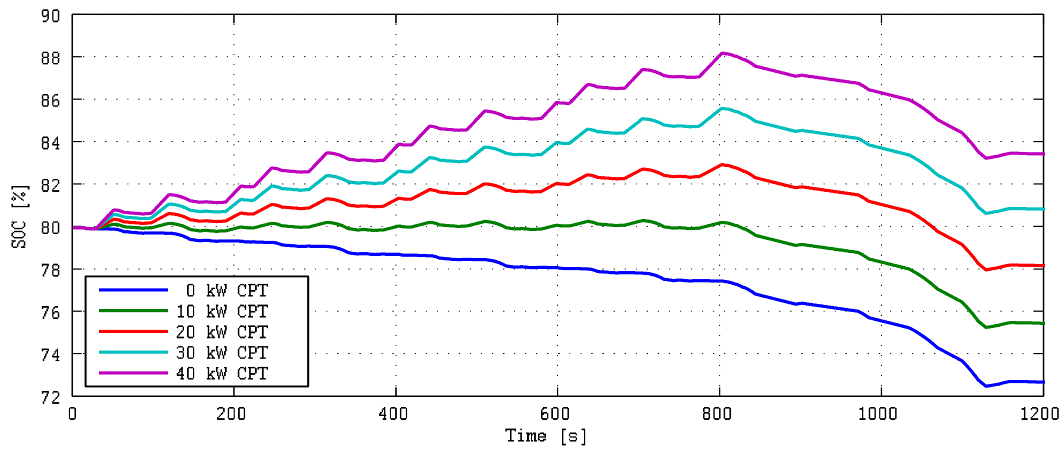

Figure 5.23 SOC of battery as a function of time (ECE-EUDC)

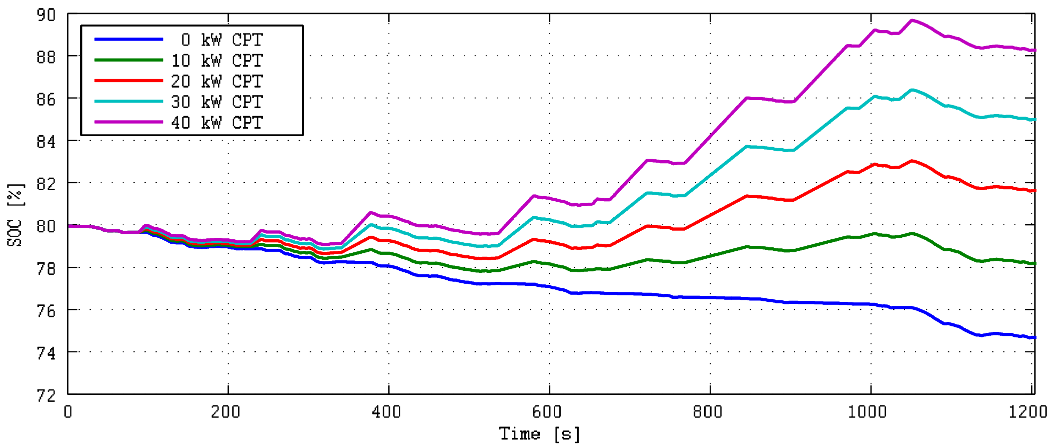

Figure 5.24 SOC of battery as a function of time (JC08)

5.4.3.5 Effect of CPT on driving range of BEV in urban driving conditions

SOC of a battery is representative of the energy content of the battery and change in SOC is representative of the energy consumption in a journey. Figure 5.25 shows the change in SOC of battery for three different urban driving cycles in consideration. With CPT enabled at traffic signals, change in SOC of battery of the vehicle under consideration for the entire journey with varying amount of CPT is shown in Figure 5.25.

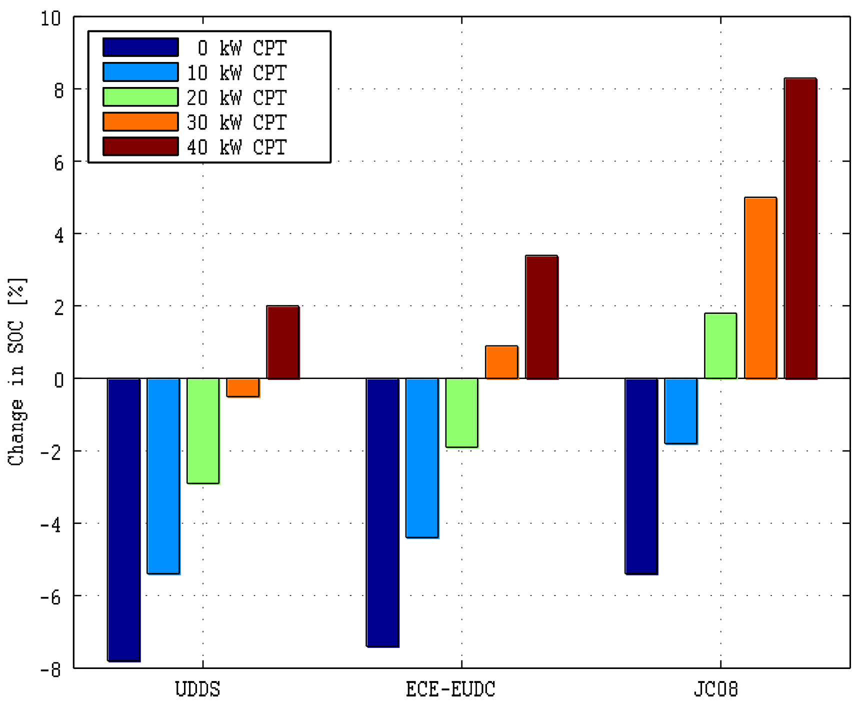

Figure 5.25 Change in SOC of battery for UDDS, ECE-EUDC and JC08 driving cycles with CPT

With driving range of a BEV seen as a major limitation; CPT system being installed at traffic signals, major improvement in driving range can be achieved. In case of UDDS and ECE-EUDC driving cycles, with 20 kW CPT, the change in SOC of battery during the journey has been reduced from 7.8% and 7.4% to 2.9% and 1.8% respectively when compared to the case when there is no CPT system installed. This means that with 20 kW CPT, the range of the vehicle has been more than doubled in both cases, i.e., an increase of 172% and 311% in range respectively in case of UDDS and ECE-EUDC driving cycles. Similarly, in case of JC08 driving cycle, with 10 kW CPT, the change in SOC of battery during the journey has been reduced from 5.3% to 1.8% which means that there is a 194% increase in the range of the vehicle. Another important observation is that in case of UDDS and ECE-EUDC driving cycles, with 30 kW CPT, the change in SOC of battery during the during the journey is close to 0%, which means that the SOC of battery at the end of the journey is approximately same as it was during the start of journey. Similarly, in case of JC08 driving cycle, this effect is seen with 20 kW CPT.

5.4.4 Case Study 2 – Highway driving cycle

In case study 2, it is studied how CPT system installed underneath the highways would enhance the driving range of range of a BEV. To simulate this, HighWay Fuel Economic Test (HWFET) cycle has been considered. HWFET cycle is a US dynamometer driving schedule used by vehicle manufactures to determine fuel economy in highway driving conditions. To simulate a reasonable driving distance, two HWFET cycles are considered back to back. This new cycle is henceforth addressed to as HWFET2. Some characteristics of HWFET2 cycle are tabulated in table 4.

Table 5-4 Characteristics of HWFET2 driving cycle

Duration (s)	Distance travelled (km)	Average speed (kmph)	Maximum speed (kmph)
1526	32.9	77	96.4

Figure 5.26 and Figure 5.27 show the speed of a vehicle and distance covered by the same vehicle as a function of time respectively in HWFET2 cycle.

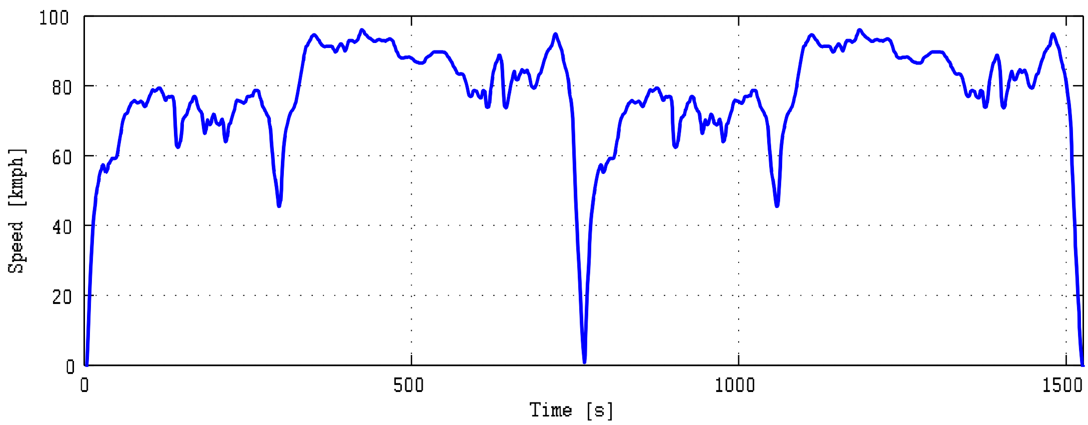

Figure 5.26 Vehicle speed as a function of time (HWFET2)

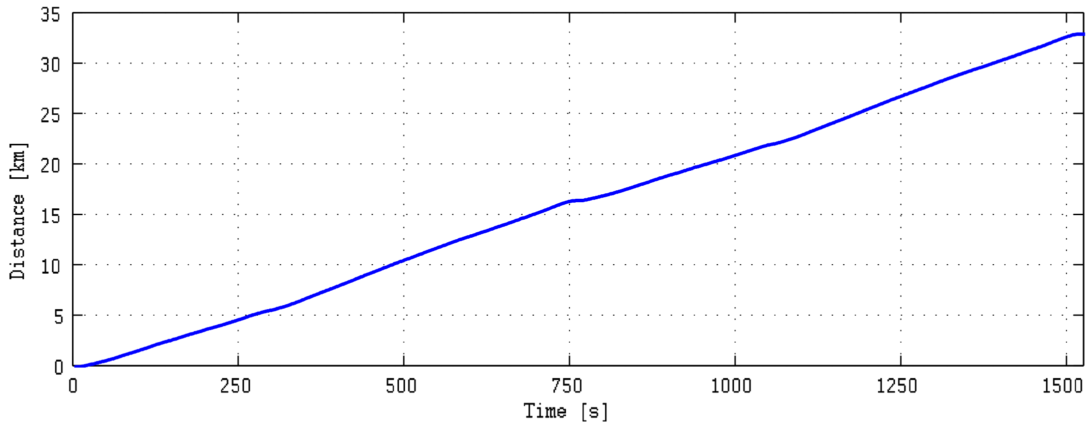

Figure 5.27 Distance covered by vehicle as a function of time (HWFET2)

Figure 5.28, Figure 5.29 and Figure 5.30 show the power flow from the battery, battery terminal voltage and current flow from the battery as a function of time respectively. Figure 5.31 shows the SOC of the battery as a function of time during the journey.

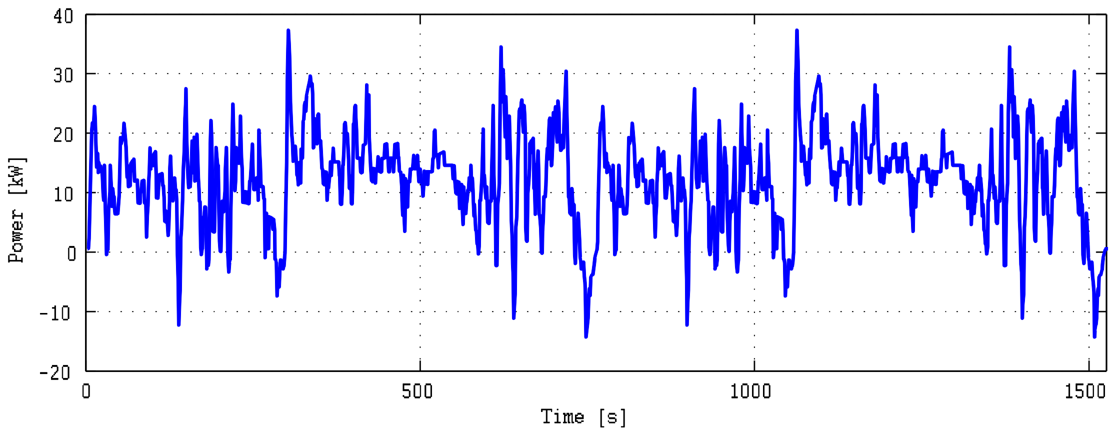

Figure 5.28 Power flow from battery as a function of time (HWFET2)

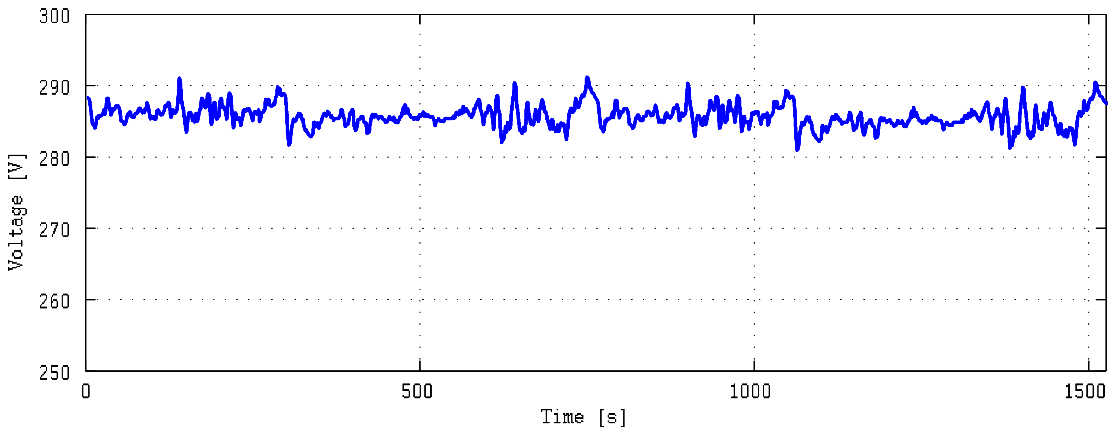

Figure 5.29 Battery terminal voltage as a function of time (HWFET2)

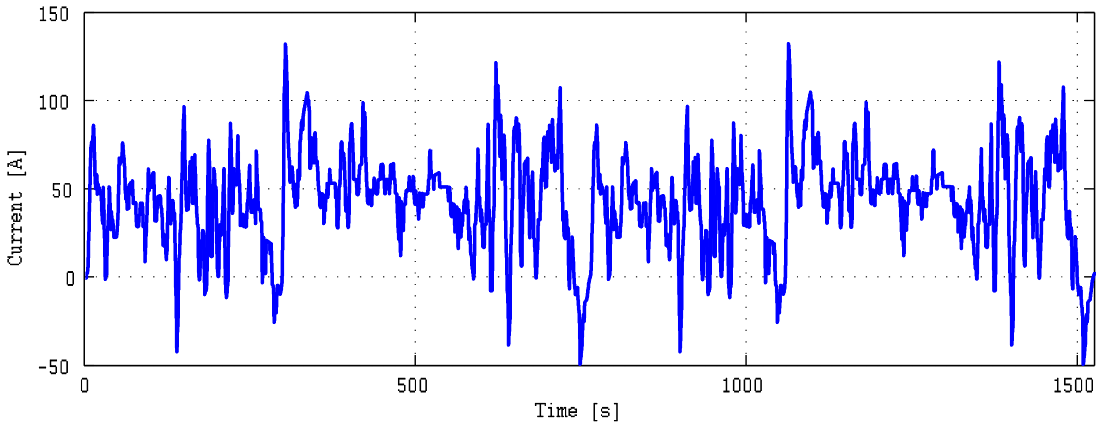

Figure 5.30 Current flow from battery as a function of time (HWFET2)

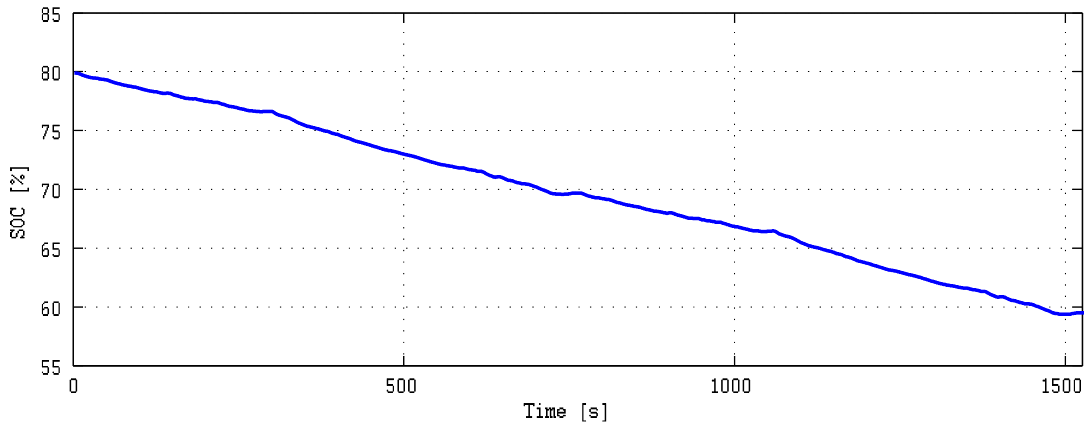

Figure 5.31 SOC of battery as a function time (HWFET2)

5.4.4.1 CPT to BEV in motion

Unlike in urban cycles, in the highway cycle HWFET2 under consideration, the vehicle is never idle during the journey. So, in order to replenish charge of the battery, CPT has to be achieved when the vehicle is in motion. To accomplish this, the primary winding of the CPT system has to be laid underneath the road through different parts of highway. The average speed of the vehicle in HWFET2 cycle is 77 kmph which means that to achieve a reasonable enhancement in range of a BEV; a considerable amount of road must be covered by the primary winding of CPT system. In this case study, the effect on range of the modelled BEV for varying road cover by primary winding of CPT system and varying amount of power transfer via CPT system is studied.

To study the effect of varying coverage of highway by primary of the CPT system, it is assumed that there are 10 CPT systems that are deployed i.e., the highway is divided into 10 equally long segments with one CPT system deployed in each section as shown in Figure 5.32. It is later shown that variation in change in SOC of battery for the entire journey when considering different number of segments is insignificant for a given percentage of road coverage by primary winding of the CPT system. Figure 5.33 shows the speed of the vehicle and distance travelled by the vehicle when travelling on the parts of the highway where CPT is enabled.

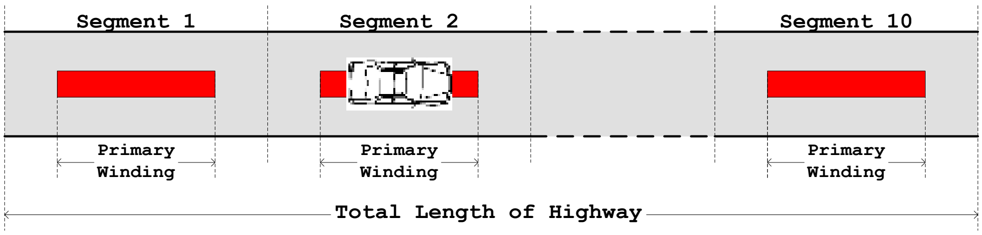

Figure 5.32 Primary winding highway coverage

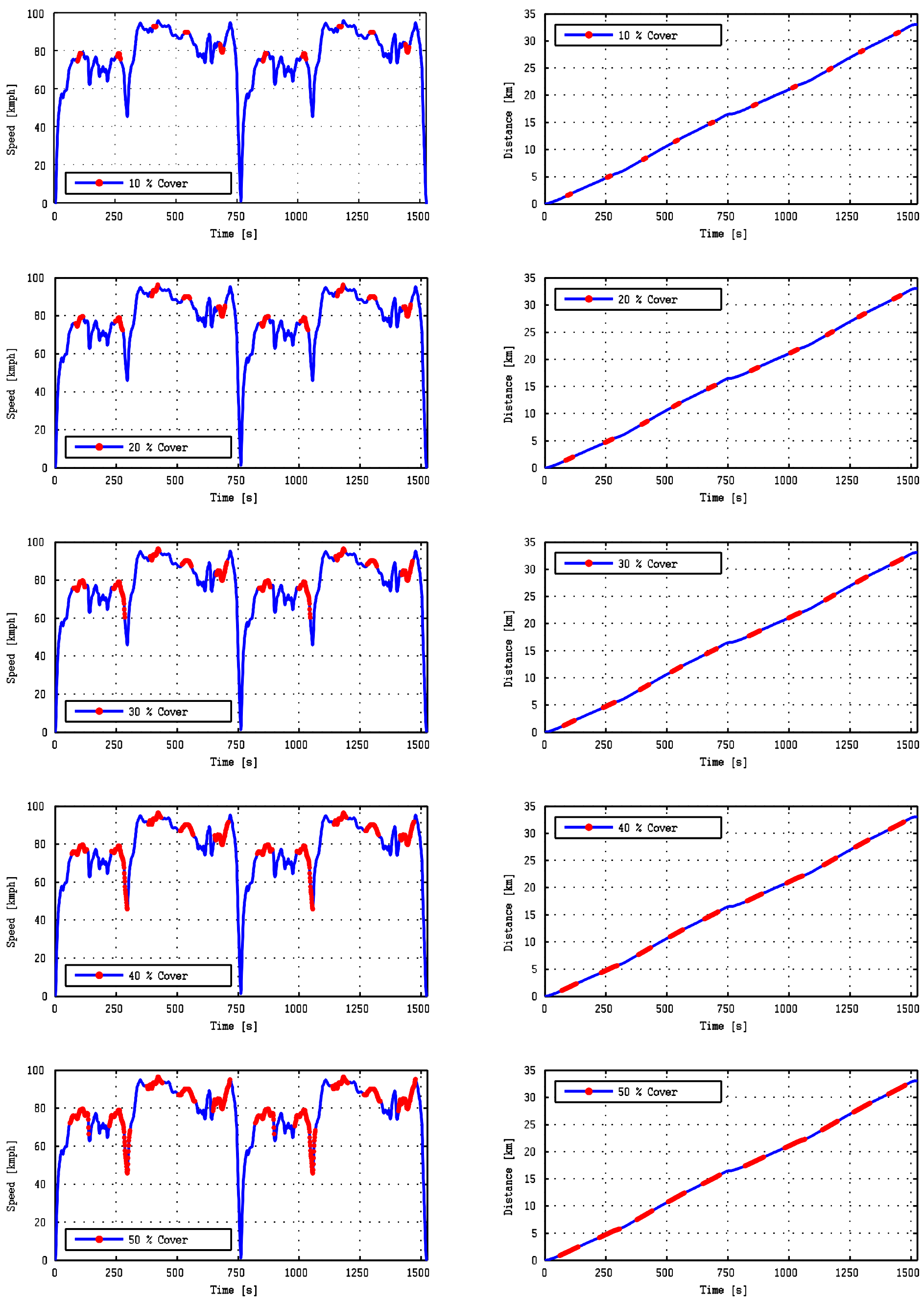

Figure 5.33 Percentage coverage of road by primary winding of CPT system

To determine the effect of power transferred via CPT system on SOC of the battery, CPT systems with varying amount of power transferred and varying percentages of highway cover by

CPT system is incorporated in vehicle-battery energy model. Figure 5.34, Figure 5.35, Figure 5.36 and Figure 5.37 show the SOC of the battery during the journey for 10 kW, 20kW, 30 kW and 40 kW of power transfer via CPT system respectively for varying coverage of highway by primary winding of CPT system.

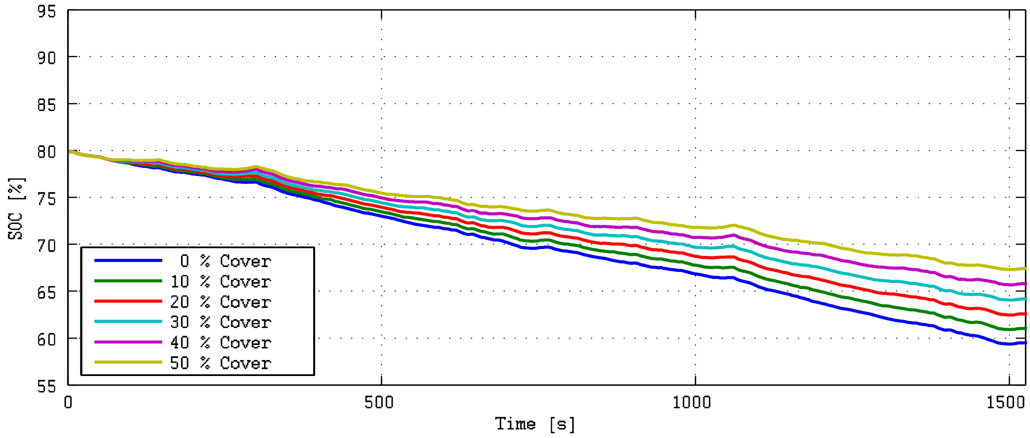

Figure 5.34 SOC of battery as a function of time for 10 kW CPT (HWFET2)

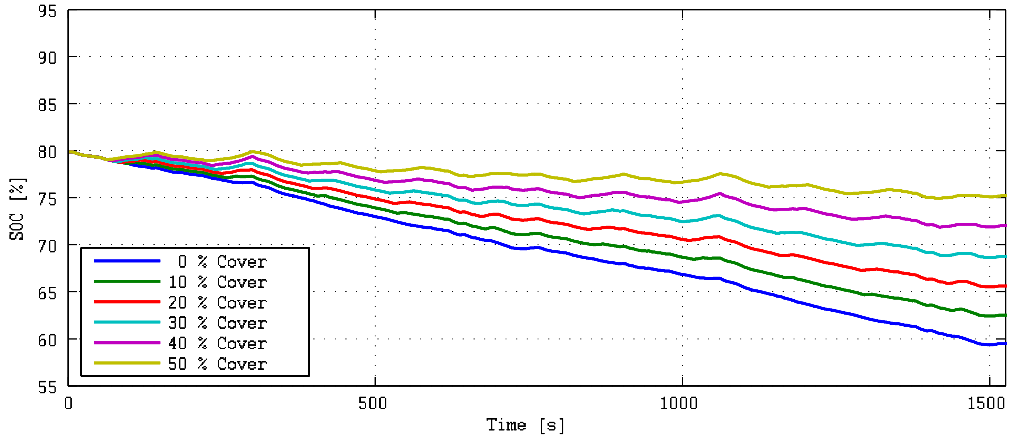

Figure 5.35 SOC of battery as a function of time for 20 kW CPT (HWFET2)

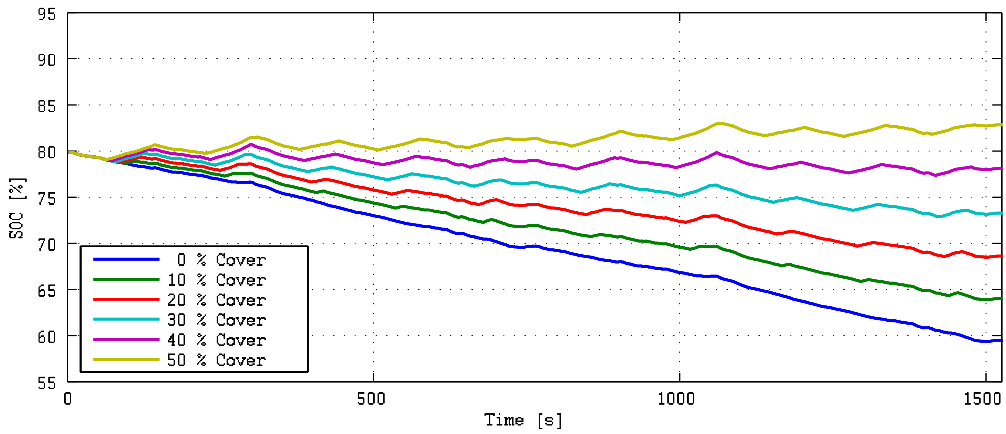

Figure 5.36 SOC of battery as a function of time for 30 kW CPT (HWFET2)

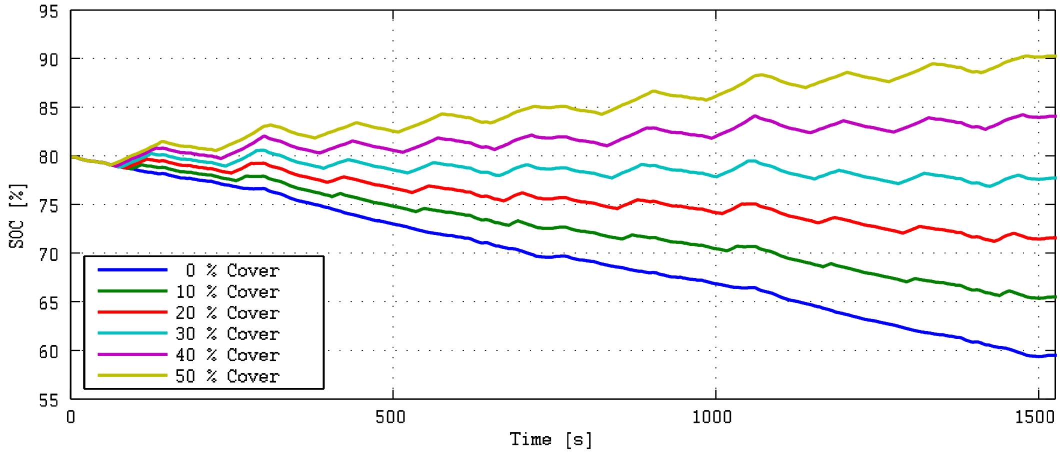

Figure 5.37 SOC of battery as a function of time for 40 kW CPT (HWFET2)

5.4.4.2 Effect of CPT on driving range of BEV in highway driving conditions

In this case study the highway is divided into 10 segments of equal length with one CPT system deployed in each segment. Simulations show that change in SOC of battery for the entire journey for a given percentage of highway cover and given power transferred via CPT system, variation with respect to the number of segments is negligible. Figure 5.38 shows the change in SOC of battery for power transfer of 10 kW via CPT with varying highway coverage and varying number of segments.

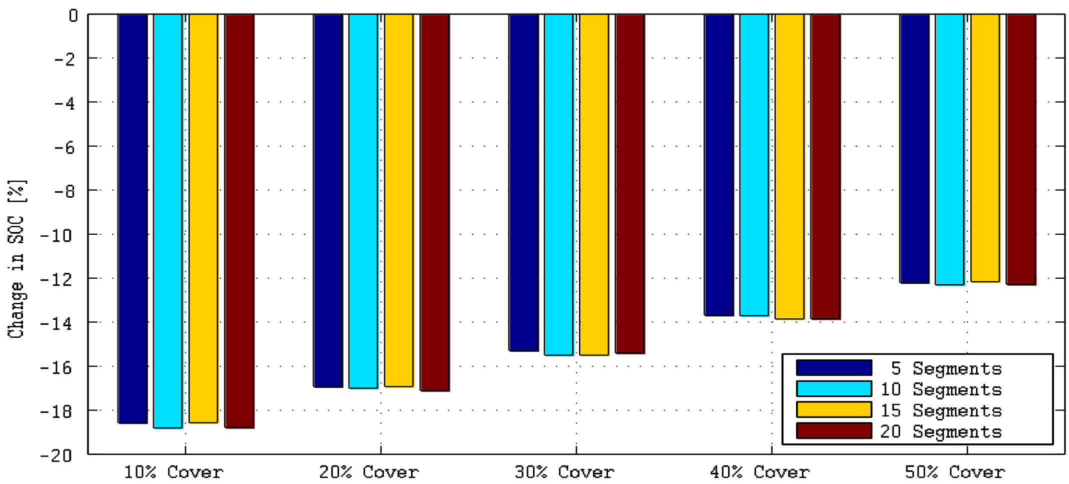

Figure 5.38 Change in SOC of battery for 10 kW CPT

Comparison of change in SOC of battery for entire journey of HWFET2 cycle for varying power transmission levels via CPT and varying percentages of highway cover by primary of CPT is shown in Figure 5.39.

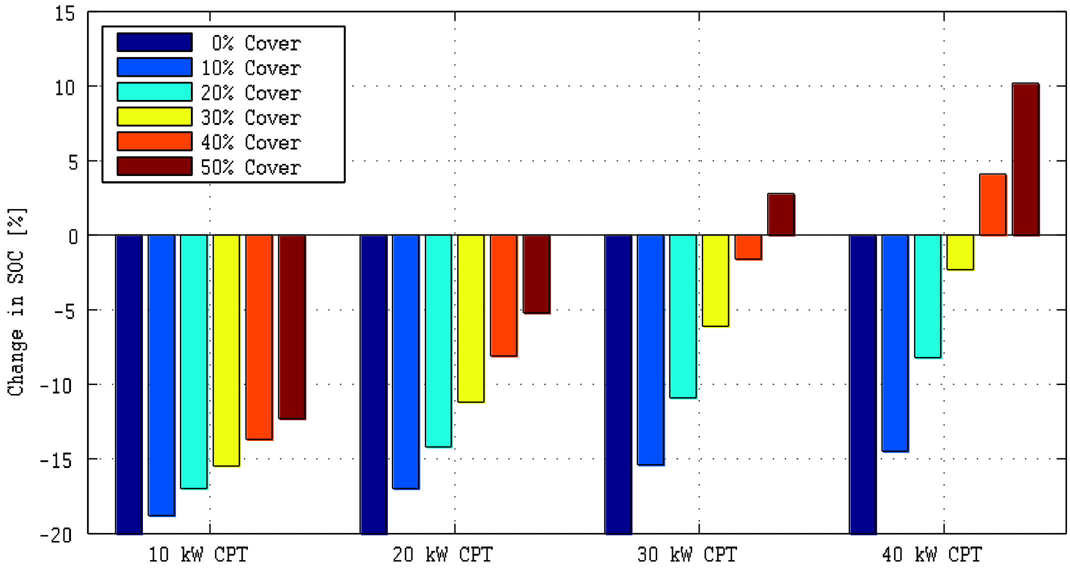

Figure 5.39 Change in SOC of battery for entire journey of HWFET2 driving cycle

It can be observed that to achieve considerable enhancement in driving range, large lengths of highway needs to be covered with primary windings of CPT system. For eg., 37% increase in range is achieved with CPT of 40 kW and highway cover of 10% (3.3 km) with primary winding of CPT. With this large length of primary winding, efficient CPT is possible only when either frequency of operation is high enough or when number of CPT systems are large in number. Both of these solutions have their own economic and practical implications which need to be studied further in depth. Another factor that has been ignored in these simulations is the effect due to presence of more than one vehicle on the same stretch of road receiving power from same CPT system. This scenario is very probable and in this case, depending upon the number of vehicles on the same stretch of road which is being powered by the same CPT system, power transfer to each vehicle will only be a fraction of power that was initially assumed. For e.g., if there are 2 vehicles on same stretch of road powered by a CPT system capable of transferring 40 kW, this power will be divided between these two vehicles and each vehicle will only receive 20 kW. These are some of the drawbacks of using CPT system in highway conditions.

5.5 Battery charging characteristics

The charging process of a Li-ion battery can be divided into two stages as shown in Figure 5.40. During the process of charging Li-ion battery, care must be taken so that each battery cell voltage do not exceeding a specified maximum value. In most cases, this peak cell voltage is specified to be 4.2 V. In stage I of the charging process, the battery is charged at constant current until the specified peak voltage of battery cells is reached. There is a linear rise of the battery cell voltage during this period of constant current charging as shown in Figure 5.40. Higher the charging current during stage I, lower is the time taken by the battery cell to reach the specified peak voltage, i.e., the slope of battery cell voltage increases with the increase in the current during stage I. In stage II, the charging takes place at constant voltage. At the end of stage I, the battery cell voltage is at the specified peak value and this voltage is maintained across the battery cell throughout the stage II. So, depending on the charging current the duration of stages I and II can be controlled.

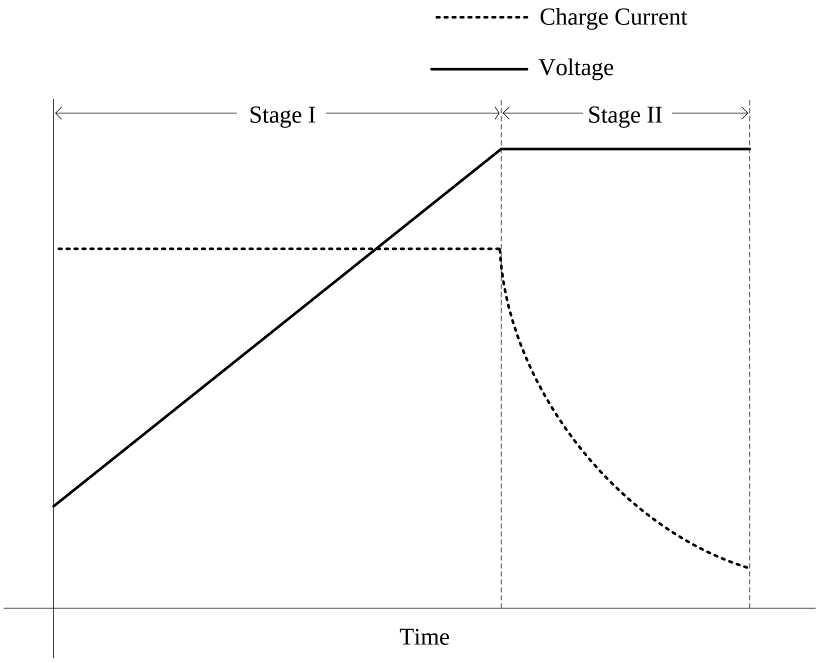

Figure 5.40 Li-ion battery charging stages

Li-ion batteries do not need to be fully charged, as in the case with lead acid batteries, nor it is desirable to do so because of the voltage stresses that the battery experiences. Studies have shown that choosing a lower voltage threshold or eliminating the saturation charge stage II altogether, prolongs the battery life but this reduces the runtime as the energy stored in battery is lowered. So, depending on the application, one can go for charging to lower peak voltage and eliminating the saturation charging which would not only increase the lifetime of the battery call but also reduce the charging time as desirable in case of BEVs, or go maximum runtime as desirable in case of consumer goods.

In case of EV applications where fast charging is required, it is desirable for the charge replenishment to occur only during stage I, i.e., constant current charging. By charging at constant current and avoiding the saturation charging, less time is taken for charge replenishment but this has a disadvantage that the battery is not charged to 100% SOC but to a lower SOC because some capacity of the battery that is replenished by stage II saturation charging is lost. Fast charging which occur at high currents may lead to sudden and localized temperature rise at some points in the battery which in turn may affect the state of health of the battery and cause faster deterioration of the battery. So, in essence, fast charging, although the need of the hour, has its own limitations.

The same battery simulation model used in case studies is used to here to demonstrate the charging characteristics of the EV battery. For the battery of capacity 24kWh under consideration for the case study, Figure 5.41. shows the battery terminal voltage for different charging currents. The nominal voltage of the battery is assumed to be 280V so the nominal capacity of the battery is 85.7 Ah. The battery is charged only up to 90% SOC so that the region of exponential voltage increase that occur when the SOC is nearing 100% is avoided which in turn reduces the voltage stress on the battery. The time taken for the battery to reach 90% SOC for different charging currents is shown in Figure 5.42. The time taken for charge replenishment of the battery under consideration for different power levels is as shown in Figure 5.43. So, depending upon the time taken for charging of the battery, choice can be made on the power rating of the CPT system.

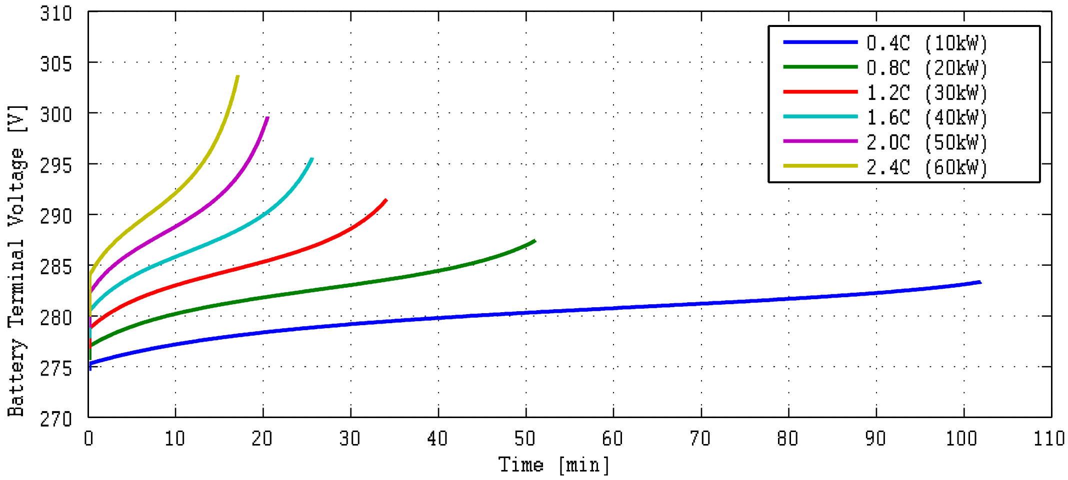

Figure 5.41 Battery terminal voltage for different charging currents

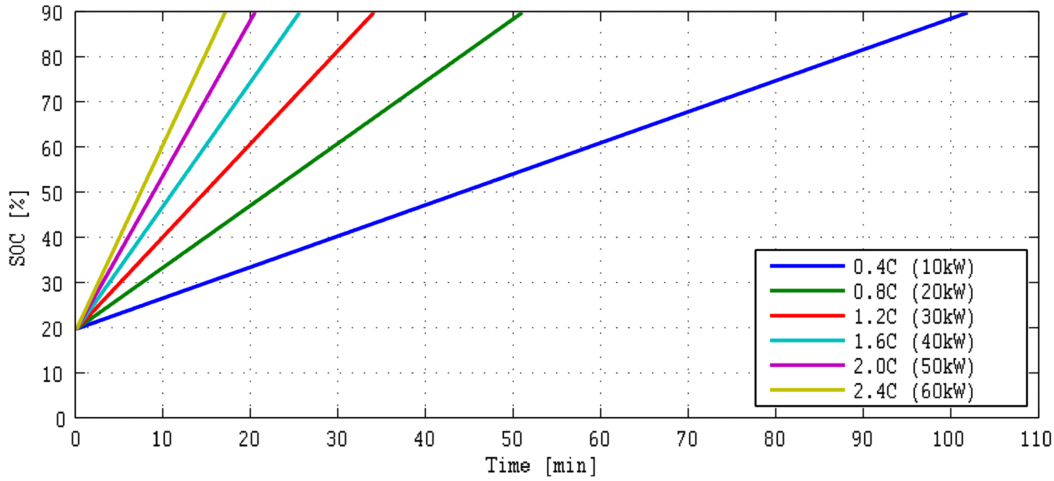

Figure 5.42 SOC of battery for different charging currents

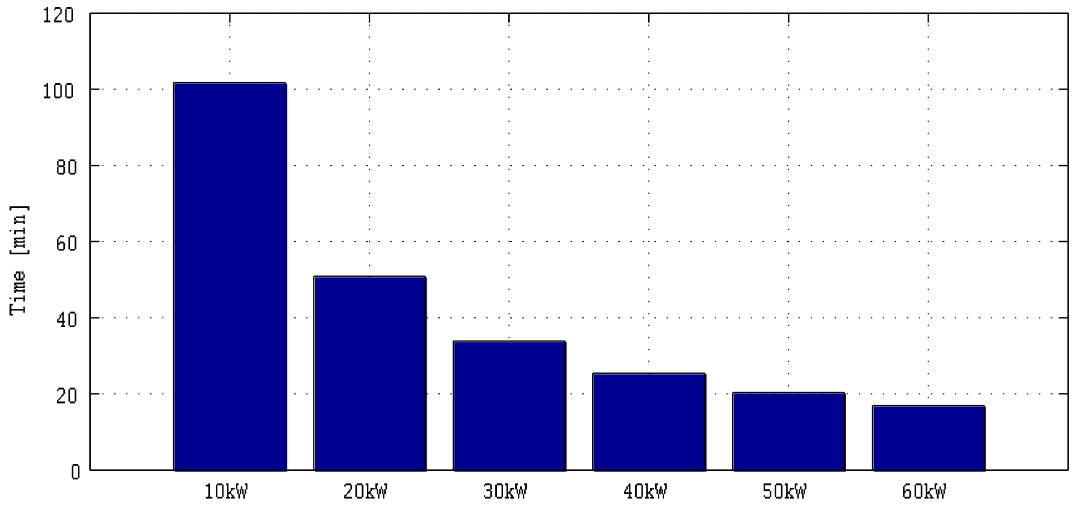

Figure 5.43 Charging time for different power levels

5.6 Cost estimation of CPT system

In this section, a rough estimate of cost of such a CPT system is present. It is fair to assume that the power electronics and the copper in the windings will be the major contributors towards the cost of such a system. A discussion with sources in power electronics converter manufacturing industry revealed that the converters employed in CPT systems, on large scale production, would cost somewhere in the vicinity of €100-120/kW and Litz wire would cost somewhere in the vicinity of € 25-35/kg.

In [9], an estimate of copper mass for square geometry of CPT transformer windings is presented. Figure 5.44 shows the estimated mass of copper to construct CPT transformer which has identical primary and secondary windings with a square geometry and an air gap of 35cms. In Figure 5.44, 'h' refers to the length of the air gap (also the distance between the base of vehicle to the ground) and 'a' refers to dimension of CPT transformer windings.

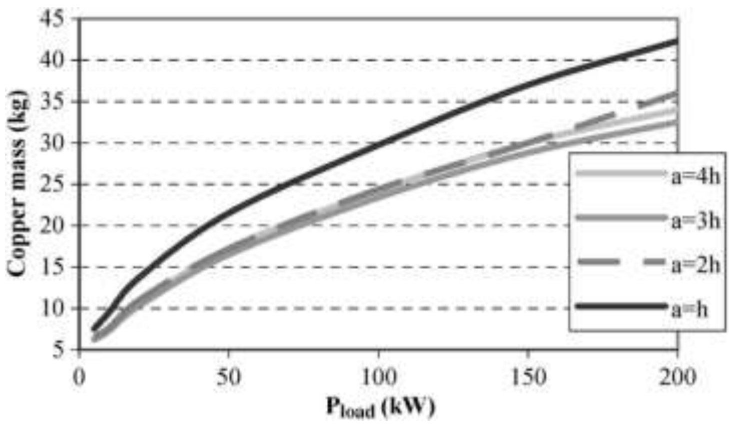

Figure 5.44 Mass of copper vs. transferred power for square geometry of CPT transformer windings with SS compensation [9]

Using this data, a rough estimate of the cost of such a CPT is shown in Figure 5.45.

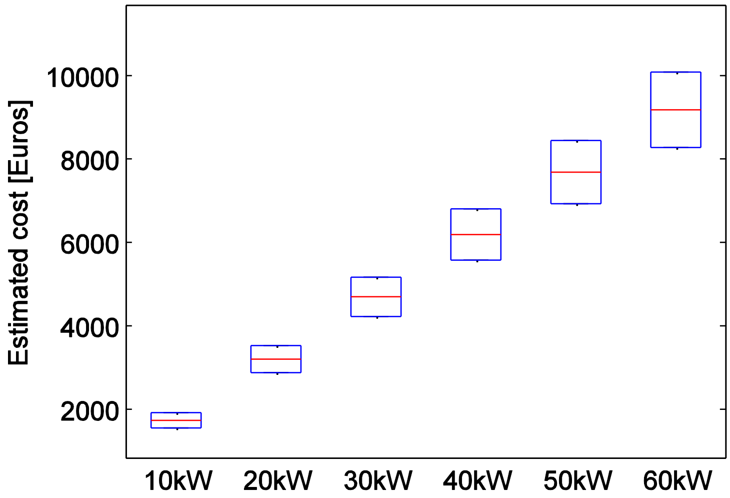

Figure 5.45 Estimated cost of CPT system

5.7 Conclusions

In this chapter, case studies are presented which demonstrated that a considerable increase in range of an EV could be attained by on-road charge replenishing CPT systems. To start with, vehicle and battery model are developed to simulate the energy usage. Urban and highway driving scenarios are considered to perform the case studies. In case of urban driving conditions, it was assumed that CPT systems are installed at the traffic signals and whenever the EV stops at a red light, charge replenishment would occur. It is found that for the three different urban driving cycles considered, the range of the EV would be more than double for CPT of 20kW. In case of highway scenario, it was assumed that the CPT primary windings are buried under the highway and charge replenishment would occur when the EV would drive over it. In other words, unlike urban scenario, in highway scenario, power transfer would occur when the EV is in motion. From the case study, it was found that in order to double the driving range of the EV, CPT of 20kW with 30% of road covered by the primary winding or 30kW CPT with 20% of road covered by the primary winding of the CPT was required. Therefore, in highway driving scenario, to attain considerable enhancement in range, large portions of the highway have to be covered by the primary winding of the CPT system.

Battery chagrining characteristics of the battery pack under consideration was discussed in the later part of the chapter. Charging times required to replenish the battery charge for various levels of power rating of CPT system is present. Finally, a rough cost estimation of CPT system for power levels of up to 60kW is presented.

Chapter 6

Conclusions and Recommendations

6.1 Conclusions

Contactless power transfer, as used in this thesis, describes the process of power transfer between two or more galvanically isolated circuits by the process of magnetic induction. The potential application of such technology can range from low level power transfer to office or home appliances to high level power transfer in industrial applications. Medical, marine, transportation etc. are some of the areas that stand to gain a lot from this kind of contactless power transfer solution. However, in this thesis, special attention is given to use of CPT technology in EV charging application.

The soaring oil prices and environmental consciousness have provided an impetus for development of electric vehicles as an alternate mode of transportation. There is no doubt that the future of transportation is electric. It is expected that by 2020 there will be more than 1 million EVs on roads in Netherlands alone. But, this will become a reality only when EVs become more acceptable and more desirable by general public than what they are today. People are reluctant to switch to EVs because of their limited range, long charging time, insufficient charging infrastructure and price. Application of CPT in charging of EVs has the potential of bringing about a paradigm shift in how the EVs are perceived today by making the charging process more convenient and safe by eliminating the need for physical contacts. Since, in case of CPT charging, the charging infrastructure would not be visible above the ground, the charging infrastructure would be tamperproof and thus easier to access and more cost effective unlike the conventional EV charging poles in public area which are prone to abuse and may depreciate urban aesthetics. CPT technology for charging application is not only efficient but also enables vehicle to grid power transfer making charging process more sustainable by enabling easy integration with smart grids.

The main goals of this thesis are to develop better understanding of CPT system in general and look at specific application of CPT in EV charging. To this end, several thesis objectives were formulates and presented in section 1.4, which can be summarized as follows:

- Develop firm theoretical background for a general purpose CPT system based on the knowledge existing in literature and pin point key design criteria for a CPT system
- Demonstrate CPT by building a prototype based on the analysis and design criteria developed.
- Study the effect of CPT charging on driving range of an EV. The concept of on-road charging is introduced and advantages of such charging process are studied.

The purpose of this chapter is put forth the important conclusions of this thesis and discuss possible recommendations for future work.

To begin with, analytical procedures for determining basic design criteria of a CPT system are presented. Limited power transfer capability and low input power factor of basic CPT transformer configuration are discussed and capacitive compensation in both primary and secondary windings as a remedy to these shortcomings is investigated. SS, SP, PS and PP compensation topologies are introduced and basic design criterion for these topologies are discussed. Extensive analyses of each of the four compensation topologies are presented. Phenomenon of bifurcation is introduced which is existence of more than one zero phase angle frequency and general criteria for bifurcation-free operation of a variable frequency control CPT system are developed. Specific advantages of using SS topology in battery charging application, which are constant current source mode and constant voltage source mode operations, are presented.

Power electronic converters which are one of the core components of a CPT system are also discussed. Resonant converter topology working at resonance frequency of the designed CPT transformer is best suited for CPT systems. A novel CPT system has been proposed to increase the overall efficiency of the system using active rectifier which would also eliminate the DC-DC charge control convert used in literature. Load current control using α –control methodology and controlling the switching of the load side active rectifier is presented.

Using the design criteria developed, practical implementation of a SS compensated topology is presented. A numerical method is presented to estimate the CPT transformer parameters which is not very accurate but can be used as for first approximation. The measured and calculated parameters of the CPT system built are compared and they closely relate to each other. Efficiency of the CPT transformer was measured to be 91% which is close to the calculated efficiency which was 95.2%. The discrepancy between the measured and calculated efficiencies is due to neglecting of proximity effect when calculating the AC resistance of CPT transformer winding. The overall efficiency of the system, however, was measured to be 83.2% owing to the losses in the inverter stage and especially the rectifier stage. Use of active rectifiers is recommended to improve the overall efficiency. The effect of misalignment which leads to lowering of efficiency of the CPT system is also studied. Practical implementation of MagIC car, is presented in which CPT technology is used to charge the on-board super-capacitor bank which acts as the primary energy source for this car.

Application of CPT in on-road charging of EVs is discussed. Case studies with urban and highway driving scenarios are presented which demonstrated that considerable increase in driving range of an EV could be attained by on-road charge replenishing CPT systems. In case of urban driving conditions, it is assumed that CPT systems are installed at the traffic signals and whenever an EV stops at red light, charge replenishment occurs. It is found that for three different urban driving cycles considered, range of the EV would be more than double for CPT of 20kW and that a CPT system of 30kW rating would fully replenish the battery charge such that change in SOC during the journey is zero. In case of highway scenario, it is assumed that the CPT primary windings are buried under the highway and charge replenishment occurs as the EV drives over it. In other words, unlike urban scenario, in highway scenario, power transfer occurs when the EV is in motion. From this case study, it was found that in order to double the driving range of the EV, CPT of 20kW with 30% of road covered by the primary winding or 30kW CPT with 20% of road covered by the primary winding was required. It is also found that for CPT of 30kW with a 40% road cover by the primary winding or for CPT of 40kW with 30% road cover by the primary winding would lead to no change in SOC of EV during the journey, which means that all the energy requirements during the journey were met by the power transferred by CPT system only and net change in SOC is zero. Lastly, a cost estimate of the CPT system for power levels up to 60kW rating is also presented.

6.2 Recommendations and scope for future work

CPT, in recent times, is emerging as one of the vastly researched topics because of sheer number of applications of this technology. This topic is also very dynamic in nature as more and more innovative solutions are emerging. With respect to this thesis, there are many issues that have not been addressed and need further investigation.

To start with, the design of CPT transformer, which is arguably the most important component of a CPT system, is not touched upon in this thesis. In literature there do exists some studies comparing different geometries and construction of CPT transformer but these studies do not conclusively address the question of which configuration/geometry is best suited for a given application.

Secondly, the control aspects of a CPT system are very faintly touched upon. There are some control strategies that have been presented but these are only discussed theoretically and not practically implemented. Practical implementation of these strategies would be necessary to study these strategies in detail.

Thirdly, in the application aspect, very simple EV and battery models were presented and used for the simulation of energy usage. It is recommended that more complex models that can more accurately simulate the energy usage should be used for similar studies in future. Also, economic and feasibility aspects of on-road charging of EV have to be looked into in more detail.

Lastly, a CPT system must comply with guidelines that have been laid down by International Commission on Non-Ionising Radiation Protection to limit human exposure to time varying EMF with the aim of preventing adverse health effects. Therefore, an in depth analysis of magnetic field around a CPT system must be performed to ascertain human safety especially in high power applications.

References

[1] Sonicare Philips Toothbrushes. www.sonicare.com

[2] B. Klontz, K.W., D. Divan, D. Novotny, R. Lorenz, *Contactless Power Delivery System for Mining Applications*, IEEE Transactions on Industry Applications, vol.31, Nº1, pp. 27-35, Jan./Feb. 1995

[3] Roberts, G., P. Hadfield, M. Humphries, F. Bauder, J. Izquierdo, *Design and Evaluation of the Power and Data Contactless Transfer Device*, 1997 IEEE Aerospace Conference Proceedings, vol.3, pp. 523-533, 1997.

[4] La Jamais Contente. http://www.e-mobile.ch/pdf/2005/Fact-Sheet_LaJamaisContente_FW.pdf

[5] Magne Charge. http://en.wikipedia.org/wiki/Magne_Charge

[6] Fernandez, C.; Garcia, O.; Prieto, R.; Cobos, J.A.; Gabriels, S.; Van Der Borght, G.; , "Design issues of a core-less transformer for a contact-less application," *Applied Power Electronics Conference and Exposition, 2002. APEC 2002. Seventeenth Annual IEEE* , vol.1, no., pp.339-345 vol.1, 2002

[7] Covic, G.A.; Elliott, G.; Stielau, O.H.; Green, R.M.; Boys, J.T.; , "The design of a contact-less energy transfer system for a people mover system," *Power System Technology, 2000. Proceedings. PowerCon 2000. International Conference on* , vol.1, no., pp.79-84 vol.1, 2000

[8] Xun Liu; Hui, S.Y.; , "Optimal Design of a Hybrid Winding Structure for Planar Contactless Battery Charging Platform," *Power Electronics, IEEE Transactions on* , vol.23, no.1, pp.455-463, Jan. 2008

[9] Sallan, J.; Villa, J.L.; Llombart, A.; Sanz, J.F.; , "Optimal Design of ICPT Systems Applied to Electric Vehicle Battery Charge," *Industrial Electronics, IEEE Transactions on* , vol.56, no.6, pp.2140-2149, June 2009

[10] M. M. Al-Asadi, A. P. Duffy, A. J. Willis, K. Hodge and T. M. Benson "A simple formula for calculating the frequency dependent resistance of a round wire", *Microwave and optical technology letters, Wiley publications,* vol. Oct. 1998, 19, issue 2, pp. 84-87.

[11] Chwei-Sen Wang; Stielau, O.H.; Covic, G.A.; , "Load models and their application in the design of loosely coupled inductive power transfer systems," *Power System Technology, 2000. Proceedings. PowerCon 2000. International Conference on* , vol.2, no., pp.1053-1058 vol.2, 2000

[12] Chwei-Sen Wang; Stielau, O.H.; Covic, G.A.; , "Design considerations for a contactless electric vehicle battery charger," *Industrial Electronics, IEEE Transactions on* , vol.52, no.5, pp. 1308- 1314, Oct. 2005

[13] de Boeij, J.; Lomonova, E.; Vandenput, A.; , "Contactless Energy Transfer to a Moving Load Part I: Topology Synthesis and FEM simulation," *Industrial Electronics, 2006 IEEE International Symposium on* , vol.2, no., pp.739-744, 9-13 July 2006

[14] Budhia, M.; Covic, G.; Boys, J.; , "Magnetic design of a three-phase Inductive Power Transfer system for roadway powered Electric Vehicles," *Vehicle Power and Propulsion Conference (VPPC), 2010 IEEE* , vol., no., pp.1-6, 1-3 Sept. 2010

[15] Budhia, M.; Covic, G.A.; Boys, J.T.; , "Design and optimisation of magnetic structures for lumped Inductive Power Transfer systems," *Energy Conversion Congress and Exposition, 2009. ECCE 2009. IEEE* , vol., no., pp.2081-2088, 20-24 Sept. 2009

[16] Chang-Yu Huang; Boys, J.T.; Covic, G.A.; Budhia, M.; , "Practical considerations for designing IPT system for EV battery charging," *Vehicle Power and Propulsion Conference, 2009. VPPC '09. IEEE* , vol., no., pp.402-407, 7-10 Sept. 2009

[17] J. L. Villa, J. Sallán, A. Liombart, J. F. Sanz, "Design of a high frequency Inductively Coupled Power Transfer system for electric vehicle battery charge" *Jour. of Appl. Energy*, vol. 86, no. 3, pp.355-363 Mar. 2009.

[18] G. A. Covic, J. T. Boys, M. L. G. Kissin, H. G. Lu, "A Three-Phase Inductive Power Transfer System for Roadway-Powered Vehicles", *IEEE Transaction on Industrial Electronics*, vol. 54, No. 6, pp. 3370-3378 Dec 2007.

[19] Raabe, S.; Elliott, G.A.J.; Covic, G.A.; Boys, J.T.; , "A Quadrature Pickup for Inductive Power Transfer Systems," *Industrial Electronics and Applications, 2007. ICIEA 2007. 2nd IEEE Conference on* , vol., no., pp.68-73, 23-25 May 2007

[20] Nagatsuka, Y.; Ehara, N.; Kaneko, Y.; Abe, S.; Yasuda, T.; , "Compact contactless power transfer system for electric vehicles," *Power Electronics Conference (IPEC), 2010 International* , vol., no., pp.807-813, 21-24 June 2010

[21] Boys, J.T.; Covic, G.A.; Yongxiang Xu; , "DC analysis technique for inductive power transfer pick-ups," *Power Electronics Letters, IEEE* , vol.1, no.2, pp. 51- 53, June 2003

[22] Jin Huh; Sungwoo Lee; Changbyung Park; Gyu-Hyeoung Cho; Chun-Taek Rim; , "High performance inductive power transfer system with narrow rail width for On-Line Electric Vehicles," *Energy Conversion Congress and Exposition (ECCE), 2010 IEEE* , vol., no., pp.647-651, 12-16 Sept. 2010

[23] Chwei-Sen Wang; Covic, G.A.; Stielau, O.H.; , "Power transfer capability and bifurcation phenomena of loosely coupled inductive power transfer systems," *Industrial Electronics, IEEE Transactions on* , vol.51, no.1, pp. 148- 157, Feb. 2004

[24] "The sodium/nickel chloride (ZEBRA) battery", J.L. Sudworth, *Journal of Power Sources* 100 (2001), pp. 149-163.

[25] "Battery and battery management for hybrid electric vehicles: a review", F. V. Conte Elektrotechnik & Informationstechnik (2006), Volume 123, Number 10. October, 2006

[26] "SAE Electric Vehicle Conductive Charge Coupler, SAE J1772, REV. MONTH01", Craig B. Toepfer, Society of Automotive Engineers (2001), http://www.arb.ca.gov/msprog/zevprog/stakeholders/infrastructure/finalsaej1772.doc

[27] "SAE J1772™ Update For IEEE Standard 1809 Guide for Electric-Sourced Transportation Infrastructure Meeting", Gery Kissel, SAE International (2010)

[28] Nissan USA, 2011, http://www.nissanusa.com/leaf-electric-car/index#/leaf-electric-car/specs-features/index

[29] "Electric vehicle technology explained", J. Larminie, J. Lowry, John Wiley & Sons, Ltd., England, 2003

[30] "Impact of Vehicle Air-Conditioning on Fuel Economy, Tailpipe Emissions, and Electric Vehicle Range" R. Farrington, J. Rugh, (2000) http://www.nrel.gov/docs/fy00osti/28960.pdf.

[31] L. Song and J. W. Evans, "Electrochemical-thermal model of lithium polymer batteries," *J. Electrochem. Soc.*, vol. 147, pp. 2086–2095, 2000

[32] P. M. Gomadam, J. W. Weidner, R. A. Dougal, and R. E. White, "Mathematical modeling of lithium-ion and nickel battery systems*," J. Power Sources*, vol. 110, no. 2, pp. 267–24, Aug. 2002

[33] D.W. Dennis,V. S. Battaglia, andA.Belanger, "Electrochemical modeling of lithium polymer batteries*," J. Power Source,* vol. 110, no. 2, pp. 310–320, Aug. 2002

[34] R. Rynkiewicz, "Discharge and charge modeling of lead acid batteries," *Proc. Appl. Power Electron. Conf. Expo.*, vol. 2, 1999, pp. 707–710

[35] D. Rakhmatov, S. Vrudhula, and D. A. Wallach, "A model for battery lifetime analysis for organizing applications on a pocket computer," *IEEE Trans. VLSI Syst.*, vol. 11, no. 6, pp. 1019–1030, Dec. 2003.

[36] P. Rong andM. Pedram, "An analytical model for predicting the remaining battery capacity of lithium-ion batteries," in *Proc. Design, Automation, and Test in Europe Conf. and Exhibition*, 2003, pp. 1148–1149

[37] B. Schweighofer, K. M. Raab, and G. Brasseur, "Modeling of high power automotive batteries by the use of an automated test system," *IEEE Trans. Instrum. Meas.*, vol. 52, no. 4, pp. 1087–1091, Aug. 2003

[38] L. Gao, S. Liu, and R. A. Dougal, "Dynamic lithium-ion battery model for system simulation*," IEEE Trans. Compon. Packag. Technol.*, vol. 25, no. 3, pp. 495–505, Sep. 2002

[39] M. C. Glass, "Battery electrochemical nonlinear/dynamic SPICE model," in *Proc. Energy Convers. Eng. Conf.*, vol. 1, 1996, pp. 292–297

[40] Tremblay, O., Dessaint, L.-A. "Experimental Validation of a Battery Dynamic Model for EV Applications." *World Electric Vehicle Journal.* Vol. 3 - ISSN 2032-6653 - © 2009 AVERE, EVS24 Stavanger, Norway, May 13 - 16, 2009

[41] J. L. Villa, J. Sallán, A. Liombart, J. F. Sanz, "Design of a high frequency Inductively Coupled Power Transfer system for electric vehicle battery charge*" Jour. of Appl. Energy*, vol. 86, no. 3, pp.355-363 Mar. 2009

[42] A.K. Ramrakhyani, S. Mirabbasi and M. Chiao, "Design and optimization of resonance-based efficient wireless power delivery systems for biomedical implants", *IEEE Trans. Biomed. Circuits and Systems*, Vol. 5, No. 1, pp. 48-63 Feb. 2011

[43] Y. Jang and M. Jovanovic, "A contactless electrical energy transmission system for portable-telephone battery chargers", *IEEE Transactions on Industrial Electronics*, vol. 50, no. 3, pp. 520–527, Jun. 2003

[44] C. Sonntag, E. A. Lomonova and J. L. Duarte "Variable-phase contactless energy transfer desktop part I: Design", *Proc. International Conference on Electrical Machines and Systems*, ICEMS, pp. 4460-4465, Oct 2008.

[45] Sample, A.P.; Meyer, D.A.; Smith, J.R.; , "Analysis, Experimental Results, and Range Adaptation of Magnetically Coupled Resonators for Wireless Power Transfer," " *IEEE Transactions on Industrial Electronics*, vol.58, no.2, pp.544-554, Feb. 2011

[46] N.A. Keeling, G.A. Covic and J.T. Boys, "A Unity-Power-Factor IPT Pickup for High-Power Applications," *IEEE Transactions on Industrial Electronics*, vol.57, no.2, pp.744-751, Feb. 2010

[47] G. Elliott, S. Raabe, G. A. Covic, and J. T. Boys, , "Multiphase Pickups for Large Lateral Tolerance Contactless Power-Transfer Systems," *IEEE Transactions on Industrial Electronics*, vol. 57, pp. 1590-1598, May 2010

[48] U. K. Madawala and D. J. Thrimawithana, "A bi-directional inductive power interface for Electric Vehicles in V2G systems," *IEEE Transactions on Industrial Electronics*, vol. 99, pp. 1-8, Feb. 2011

[49] M. L. G. Kissin, J. T. Boys, and G. A. Covic, "Interphase mutual inductance in polyphase inductive power transfer systems," IEEE Trans. Industrial Electronics, vol. 56, no. 7, pp. 2393–2400, July 2009

[50] M. L. G. Kissin, H. Hao and G. A. Covic, "A practical multiphase IPT system for AGV and roadway applications," in IEEE Energy Conversion Congress and Exposition, Sept. 2010, pp. 1844–1850

[51] G. A. J. Elliott, S. Raabe, Gr. A. Covic and J. T. Boys, "Multiphase pickups for large lateral tolerance contactless power-transfer systems," IEEE Trans. Industrial Electronics, vol. 57, no. 5, pp. 1590–1598, May 2010

Appendix A- Paper I

Paper Title: Analysis and design considerations for a contactless power transfer system

Authors: S. Chopra, P. Bauer

Conference: *33rd International Telecommunications Energy Conference (INTELEC),* 9-13 Oct. 2011

Analysis and Design Considerations for a Contactless Power Transfer System

S. Chopra, P. Bauer
Delft University of Technology
Mekelweg 4, 2628 CD Delft
The Netherlands
S.Chopra@student.tudelft.nl, P.Bauer@tudelft.nl

Abstract— Contactless power transfer (CPT) is a safe, convenient and reliable way of transferring power in many applications where there exists no physical contact between the source and the load. In this paper, general design criteria are described for efficient power transfer in a CPT system. The need for compensation has been discussed and general conditions for achieving bifurcation-free operation for each compensation topologies have been derived. Advantages of using Series-Series compensated topology over other topologies are discussed. Constant current and constant voltage modes of operation of Series-Series topology and conditions for these modes of operation are presented. An experimental CPT setup is built to validate the theory developed.

Keywords-Contactless power transfer; compensation topologies; bifurcation phenomenon

I. INTRODUCTION

The term Contactless Power Transfer (CPT), in general, can be used to describe power transfer between two objects that are physically unconnected. The word 'contactless' infers some sort of remote action, so that the transfer of power could occur over a physical distance i.e., a non-galvanic contact is established between the source and the load that enables power transfer. In context of electrical systems, CPT can be achieved by electromagnetic induction or electromagnetic radiation. In this paper, CPT refers to transfer of electric power between two or more galvanically isolated electric circuits by means of magnetic induction. Transfer of power through a non-galvanic medium in some applications is sometimes the only way of transferring the power from source to the load. CPT is must in applications where conventional cables and connectors are either impractical or useless – either for the sake of convenience, safety or because of absence of another solution. Presently, there are a number of CPT solutions for applications for varying power levels and varying distances. The applications of this technology can range from power transfer to low power home and office devices [5]-[7][12]-[14], biomedical devices [4] etc., to high power applications like public transportation[8][9], electric vehicle charging [10][11] etc.

An inductively coupled CPT system is capable of efficiently delivering power from a stationary primary source to a movable or a stationary secondary source over relatively large air gap. This way of CPT is achieved by magnetically transferring power from primary winding to the secondary winding of specially constructed transformers. These transformers have a large air gap between the primary and secondary and thus the characteristics of these transformers are very different from the conventional transformers. Due to the large air gap between the primary and secondary windings, the primary and secondary leakage inductances are large and magnetic coupling is very weak which in turn implies large magnetizing current. Since CPT transformer with air core is light in weight and has no core losses [1], for purpose of analysis, CPT transformer with air core is considered.

In this paper, analysis is presented for design of a CPT system. Firstly, a basic CPT system is considered and disadvantages of such a system and the need for capacitive compensation are identified. The various compensation topologies and analysis of these topologies with respect to the efficiency of the CPT are presented. The phenomenon of bifurcation, which could lead to loss of power transfer capability, is introduced and general criteria is determined for bifurcation-free operation for all the compensation topologies. Finally, the theory so developed is then applied to the design of a 100W CPT experimental setup with a 50 mm air gap between the source and the load.

II. BASIC CPT TRANSFORMER ANALYSIS

In this section, analysis of power transfer capability of basic CPT transformer configuration is presented. Fig. 1(a) shows the circuit representation of basic air-core CPT transformer used to demonstrate power transfer from a sinusoidal voltage source to a resistive load R_L. L_1 and L_2 represent the self-inductances of primary and secondary windings respectively; associated primary and secondary winding resistances are represented by R_1 and R_2 respectively; M is the mutual inductance between the transformer windings. The equivalent circuit representation of the CPT transformer is obtained and represented in Fig. 1(b). This equivalent circuit representation makes the process of network analysis easier. In the equivalent representation, $L_a = L_1 - M$ and $L_b = L_2 - M$, i.e., L_a and L_b represent the leakage inductances of primary and secondary windings respectively. For the purpose of analysis, it is assumed that the frequency of operation ω of the voltage source $\overrightarrow{V_1}$ is far below the resonance frequency of the CPT transformer and hence the stray capacitances are neglected.

The impedance as seen by the source is given by

$$Z_1 = \frac{\omega^2 M^2 + (R_1 + j\omega(L_a + M))(R_L + R_2 + j\omega(L_b + M))}{R_L + R_2 + j\omega(L_b + M)} \tag{1}$$

The efficiency of the power transfer from source to load is given by

$$\eta = \frac{R_L}{(R_L + R_2)\left(1 + \frac{R1(R_2 + R_L)}{\omega^2 M^2}\right) + R1\left(\frac{L_b + M}{M}\right)^2} \tag{2}$$

However, for condition specified by Eq. (3), power transfer at maximum possible efficiency occurs. This efficiency is given by Eq. (4).

$$\omega \gg \frac{\sqrt{R_1(R_2 + R_L)}}{M} \tag{3}$$

$$\eta_{\max} = \frac{R_L}{R_L + R_2 + \frac{R_1(L_b + M)^2}{M^2}} \tag{4}$$

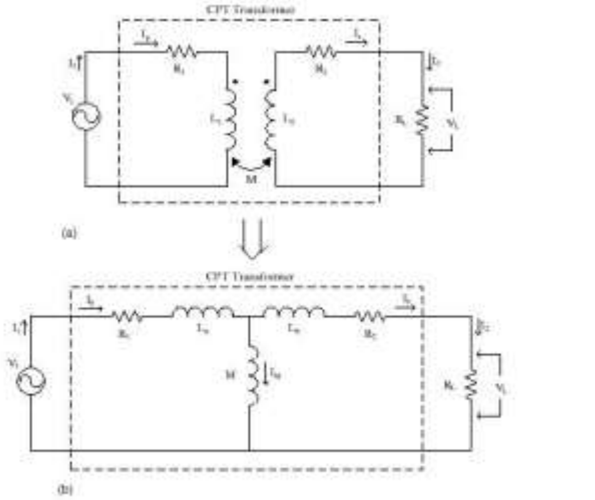

Figure 1. Basic CPT circuit representation (a) Air-core transformer representation (b) Equivalent circuit representation

The power factor, which is defined as the ratio of active power flowing into a device to the apparent power it draws, is highly dependent on the load and the CPT transformer inductances. However, in order to attain high efficiency of power transfer, high operational frequency satisfying Eq. (3) is desirable. But, at relatively high frequencies, the impedance as seen by the source becomes more and more inductive in nature. As a result, the power factor becomes very small and starts approaching zero as the frequency increases. This means that the high frequency source side inverter should have a large VA rating and the circulating power would also decrease the efficiency of power transfer. This is one of the major disadvantages of using basic CPT configuration for power transfer. To overcome this, capacitive compensation in both primary and secondary windings is recommended.

III. Capacitive Compensation Topologies

Compensation capacitors are used in CPT applications to increase the efficiency and the capability of the system to transfer power. Capacitive compensation is used in both primary and secondary winding of the CPT transformer. The purpose of compensation in the secondary winding is to enhance the power transfer capability of the CPT transformer and the primary compensation is used to decrease the VA rating of the source side converter thereby ensuring power transfer at unity power factor [3].

There exists four basic compensation topologies that are widely used. These are Series-Series (SS) topology, Series-Parallel (SP) topology, Parallel-Series (PS) topology and Parallel-Parallel (PP) topology as shown in Fig. 2.

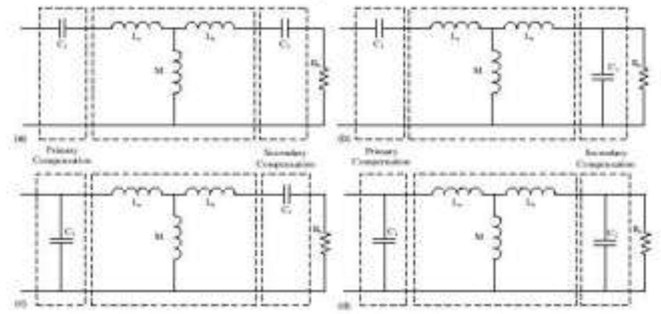

Figure 2. Compensation topologies (a) SS (b) SP (c) PS (d) PP

To increase the power transfer capability of CPT system in all the above mentioned topologies, it is necessary that the system operates at the secondary resonance frequency ω_0. When operating at this frequency, the self-inductance of the secondary winding is fully compensated by the secondary compensation capacitance and therefore the impedance of the secondary as seen by the primary is purely resistive in nature. Therefore, for all the topologies, the value of compensation capacitance C_2 is given by

$$C_2 = \frac{1}{\omega_0^2 (L_b + M)} \tag{5}$$

The primary compensation is so chosen that the high frequency inverter which acts as the primary power source has minimum possible VA rating, i.e., the input current and voltage are in phase. Therefore, based on the topology, the value of the primary compensation capacitance are derived and tabulated in Table I. For each of the compensation topologies, the equations for efficiencies are also derived and tabulated in Table II. The maximum possible theoretical efficiency, as tabulated in Table III, can be reached if the operating frequency is chosen high enough. This condition on the operating frequency is as tabulated in Table III. However, when taking into account rise of resistance associated with the primary and secondary windings due to skin effect and proximity effect at high frequencies, there exists an optimum frequency at which maximum efficiency can be achieved. The quality factors Q_1 and Q_2 associated with the primary and secondary resonance circuits are given by equations tabulated in Table IV. These quality factors are defined as the ratio of reactive power to real power and are calculated at the secondary resonance frequency ω_0.

TABLE I. PRIMARY COMPENSATION CAPACITANCE

SS topology	$C_1 = \frac{(L_b + M)C_2}{(L_a + M)}$
SP topology	$C_1 = \frac{(L_b + M)^2 C_2}{(L_a + M)(L_b + M) - M^2}$
PS topology	$C_1 = \frac{(L_a + M)(L_b + M)^2 C_2^2 R_L^2}{M^4 + (L_a + M)(L_b + M)R_L^2}$
PP topology	$C_1 = \frac{(L_b + M)^2\left((L_a + M)(L_b + M) - M^2\right)C_2}{\left((L_b + M)(L_a + M) - M^2\right)^2 + M^4 R_L^2 (L_b + M)C_2}$

TABLE II. EFFICIENCY OF THE FOUR COMPENSATION TOPOLOGIES

SS and PS topologies	$\eta = \frac{R_L}{(R_L + R_2)\left(1 + \frac{R_1(R_2 + R_L)}{\omega^2 M^2}\right)}$
SP and PP topologies	$\eta = \frac{R_L}{R_L + R_2 + \frac{R_2 R_L^2}{\omega^2 (L_b + M)^2} + \frac{R_1 R_2^2}{\omega^2 M^2} + \frac{R_1\left((L_b + M)\omega^2 + \frac{R_2 R_L}{\omega^2 (L_b + M)}\right)^2}{\omega^2 M^2}}$

TABLE III. MAXIMUM EFFICIENCY AND CONDITIONS

SS and PS topologies	$\eta_{\max} = \frac{R_L}{R_L + R_2}$	$\omega \gg \frac{\sqrt{R_1(R_2 + R_L)}}{M}$
SP and PP topologies	$\eta_{\max} = \frac{R_L}{R_L + R_2 + \frac{R_1(L_b + M)^2}{M^2}}$	$\omega \gg \frac{\sqrt{R_2 R_L^2 M^2 + R_1 R_2^2 (L_b + M)^2}}{(L_b + M)M}$

TABLE IV. PRIMARY AND SECONDARY QUALITY FACTORS

SS and PS topologies	$Q_1 = \frac{(L_a + M)R_L}{\omega_0 M^2}$	$Q_2 = \frac{\omega_0 (L_b + M)}{R_L}$
SP and PP topologies	$Q_1 = \frac{\omega_0 (L_a + M)(L_b + M)^2}{M^2 R_L}$	$Q_2 = \frac{R_L}{\omega_0 (L_b + M)}$

IV. BIFURCATION

A CPT system can be either operated with a fixed frequency control or a variable frequency control. A fixed frequency control CPT system is assumed to operate at the predefined nominal design frequency which is equal to the secondary resonance frequency. However, for reason such as temperature rise, if there is a change in secondary compensation capacitance, the secondary resonance frequency would change accordingly. In a fixed frequency control CPT system, this would mean that the system is no longer operating at secondary resonance frequency which will have an adverse effect on the power transfer capability of the CPT system. When operating at off resonance frequency, even a small change in secondary capacitance will have a profound effect on the power transfer capability as shown in [2]. Also, in case of SP, PS and PP topologies where primary compensation capacitance is a function of M and R_L which could vary depending on the positioning of the secondary w.r.t. primary and the load, a fixed frequency system would not always operate at zero phase angle of the power supply i.e., the phase difference between the power supply voltage and current will not be zero. This will cause hard switching of the inverter switches which in turn will lead to higher switching losses.

A variable frequency control can be employed to minimize the required VA rating of the power supply. This can be accomplished by controlling the frequency in such a way that the phase difference between the power supply voltage and current is always zero i.e., the imaginary part of the impedance as seen by the power supply is zero. However, analysis of a compensated CPT system shows that the system could have as many as three zero phase angle frequencies of which only one is the resonance frequency. This phenomenon of existence of more than one zero phase angle frequency is called bifurcation. Analysis of this phenomenon is shown for a SS compensated system in the following section.

A. SS topology – bifurcation analysis

In order to analyse the phenomenon of bifurcation, SS topology is considered. However, similar analysis can be carried out for the other three topologies. At the end of this analysis, a condition is derived which when fulfilled will eliminate bifurcation and the CPT system will have only one zero phase angle frequency which will be the resonance frequency.

For the system to have a zero phase angle frequency, the imaginary part of the impedance as seen by the source must be zero, i.e., $Im(Z_{1,SS}) = 0$. The imaginary part of the impedance as seen by the source is given by

$$Im(Z_{1,SS}) = \left(\omega(L_a + M) - \frac{1}{\omega C_1}\right) - \frac{\omega^2 M^2 \left(\omega(L_b + M) - \frac{1}{\omega C_2}\right)}{R_L^2 + \left(\omega(L_b + M) - \frac{1}{\omega C_2}\right)^2} \quad (6)$$

For simplifying the analysis, normalized frequency u as defined by Eq. (7) is considered. By substituting Eq. (8) in $Im(Z_{1,SS}) = 0$, Eq. (9) is obtained.

$$u = \frac{\omega}{\omega_0} \quad (7)$$

$$u^2 = (L_a + M)C_1\omega^2 = (L_b + M)C_2\omega^2 \quad (8)$$

$$(u^2 - 1)((u^2 - 1)^2 + R_L^2\omega^2 C_2^2 - M^2\omega^4 C_1 C_2) = 0 \quad (9)$$

Eq. (9) can have at most three real roots of which $u = 1$, is one of the roots which corresponds to zero phase angle frequency being equal to the resonance frequency. Further simplification of Eq. (9) gives Eq. (10), where k is the coupling coefficient.

$$(u^2 - 1)^2 + \frac{u^2}{Q_2^2} - u^4 k^2 = 0 \quad (10)$$

For bifurcation-free operation, the roots of the Eq. (10) must be complex, i.e., the discriminant of the equation must be less than zero. This gives the criterion for achieving a single zero phase angle frequency for SS topology.

$$Q_2 < \sqrt{\frac{1}{2\left(1 - \sqrt{1 - k^2}\right)}} \quad (11)$$

The necessary criteria for achieving a single zero phase angle frequency for all the topologies are tabulated in Table V.

TABLE V. NECESSARY CRITERIA FOR A SINGLE ZERO PHASE ANGLE FREQUENCY

SS topology	$Q_2 < \sqrt{\frac{1}{2\left(1 - \sqrt{1 - k^2}\right)}}$
SP and PP topologies	$Q_2 < \frac{1}{k}\sqrt{1 - k^2}$
PP topology	$Q_2 < \frac{1}{k}$

V. CHOICE OF TOPOLOGY

All the four topologies have different advantages and disadvantages, and their choice mainly depends on the type of application. In [3], some of these advantages and disadvantages are described. However, for any general CPT system, SS topology has two major advantages that make it exceptionally useful. Firstly, the reflected impedance of the secondary winding on to the primary winding has only a real reflected component and no reactive component. This means that the secondary winding will draw only active when operating at secondary resonance frequency, giving the secondary a unity power factor. The second advantage is that the choice of primary and secondary compensation capacitances is independent of either mutual inductance or the load which means that the primary and secondary resonance frequencies are independent of either the mutual inductance or the load and only depend on the self-inductance of the primary and secondary windings and their respective compensation capacitances. Therefore, for applications where relative orientations of the windings as well as load currents are variable, it is desirable to have a CPT system which has a resonant frequency independent of these variables.

In many CPT applications, the transferred power is used to replenish battery charge which means that in these applications, the load is a battery which needs to be recharged. Some of these applications are EV battery charging, battery charging of consumer electronics like cell phones etc. For battery charging applications, SS topology provides some very specific advantages which are described in the following section.

A. SS topology for battery charging application

Li-ion batteries, because of their high specific power and ability to charge quickly, are being extensively used in applications where batteries act as the primary energy source. The charging process of a Li-ion battery can be divided into two stages; the constant current charging stage and the constant voltage charging stage. During the constant current charging stage, the battery is charged at constant current until the specified peak voltage of battery cells is reached. There is a linear rise of the battery cell voltage during this period of constant current charging. During the constant voltage charging stage, the charging takes place at constant voltage. At the end of constant current charging stage, the battery cell voltage is at the specified peak value and this voltage is maintained across the battery cell throughout the constant voltage charging stage. Therefore, a topology that acts as both a constant current source and constant voltage is very much desirable in battery charging application. Based on the frequency of operation, a SS topology CPT system can act as a constant current source and a constant voltage source without any complex sensory control involved.

1) Constant current source mode

When operating at resonance frequency ω_0, the load current $\overrightarrow{I_2}$ as represented in Fig. 3, is given by

$$\overrightarrow{I_2} = \frac{\overrightarrow{V_1}}{j\omega_0 M} \quad (12)$$

This means that when operating at resonance frequency, the SS topology acts as a constant current source for the load i.e., the load current is independent of the load. Load current $\overrightarrow{I_2}$ is only dependent on the source voltage $\overrightarrow{V_1}$, the resonance frequency ω_0 and the mutual inductance M between primary and secondary windings. Apart from the obvious advantage of this topology in the constant current charging stage, this topology is inherently short circuit proof.

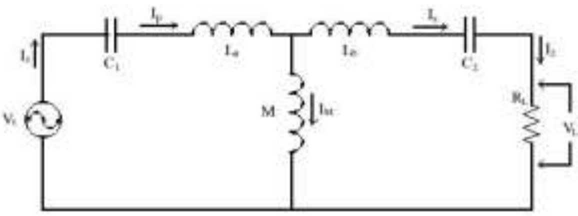

Figure 3. SS topology schematic

2) Constant voltage source mode

The same topology can also act as a constant voltage source for the load. In order to arrive at the conditions when this topology works in constant voltage source mode, consider the ratio of the load voltage $\overrightarrow{V_L}$ to the source voltage $\overrightarrow{V_1}$ given by Eq. (13).

$$\frac{\overrightarrow{V_L}}{\overrightarrow{V_1}}=\frac{-jR_L M C_1 C_2 \omega^3}{(1-(L_a+M)C_1\omega^2)(1-(L_b+M)C_1\omega^2+j\omega R_L C_2)-M^2 C_1 C_2 \omega^4} \tag{13}$$

At frequencies ω_1 and ω_2 given by Eq. (14) and Eq. (15), the load voltage becomes independent of the load. At these frequencies (ω_1 and ω_2), the load voltage is given by Eq. (16) and Eq. (17) respectively. The load voltage at these frequencies is only dependent on the self-inductances of the CPT transformer windings and the input source voltage and is either in phase with the input source voltage or 180^0 out of phase with the input source voltage.

$$\omega_1=\frac{\omega_0}{\sqrt{1-k}} \tag{14}$$

$$\omega_2=\frac{\omega_0}{\sqrt{1+k}} \tag{15}$$

$$\overrightarrow{V_L}=\sqrt{\frac{L_b+M}{L_a+M}}\overrightarrow{V_1} \tag{16}$$

$$\overrightarrow{V_L}=-\sqrt{\frac{L_b+M}{L_a+M}}\overrightarrow{V_1} \tag{17}$$

However, when operating the CPT system at either of the two frequencies ω_1 or ω_2, the system is no longer in resonance and this off-resonance operation will have an adverse effect on the power transfer capability of the system. Also, since the CPT system is no longer operating at the zero phase angle frequency at the source side, the source side inverter will have a larger VA rating when compared to zero phase angle frequency operation.

VI. Practical Implementation

Based on the design criteria discussed in the paper so far, a 100W CPT system was designed and built. The air gap between the primary and the secondary windings of the CPT system was chosen to be 50mm. SS topology was chosen as the compensation technique and the circuit schematic of the CPT system is as shown in Fig. 4.

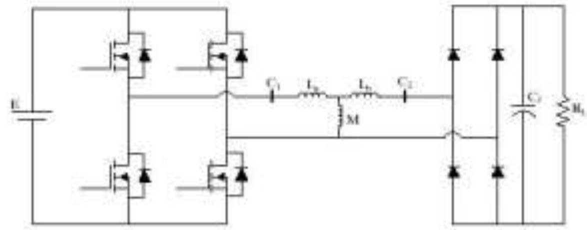

Figure 4. Circuit diagram of the experimental setup used to demonstrate CPT

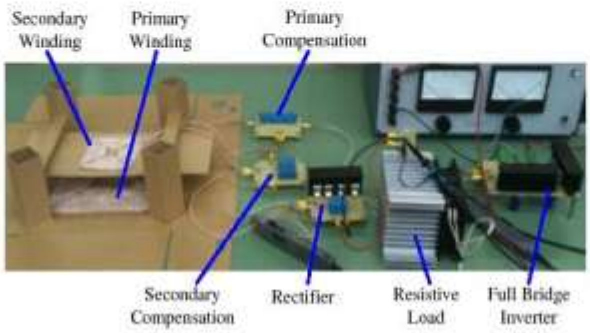

Figure 5. CPT experimental setup

The parameters of the experimental setup are tabulated in Table VI. The efficiency of the CPT transformer was measured to be 91% which is close to the efficiency as calculated by the equation given in Table II which was 95.2%. Since the operating frequency was 105 KHz, Litz wire was used to construct the primary and secondary winding of the CPT transformer. Although rise in winding AC resistance due to skin effect was taken into consideration, rise in winding AC resistance due to proximity effect, because of geometrical complexity of the windings, was neglected in the calculations and hence the discrepancy in the calculated and measured efficiency. The overall efficiency of the system was measured to be 83.2% owing to losses mostly in the rectifier stage. However, with active rectifiers, the overall system efficiency can be improved considerably.

TABLE VI. EXPERIMENTAL CPT SETUP PARAMETERS

L_a (µH)	100
L_b (µH)	8.9
M (µH)	6.5
k	0.16
$R_1(\Omega)$	0.13
R_2 (Ω)	0.04
R_L (Ω)	2.5
C_1 (nF)	22
C_2 (nF)	168
C_f (uF)	30
Resonance frequency f_0 (kHz)	105
Q_1	9.62
Q_2	4.06
% Efficiency (CPT transformer)	91
% Efficiency (overall)	83.2

VII. Conclusion

In this paper, basic design criteria of a CPT system are discussed. In order to achieve high power transfer capability and zero phase angle between the source voltage and current, four compensation topologies were discussed. Bifurcation phenomenon which is existence of more than one zero phase angle frequency was described and general criteria for bifurcation-free operation of a variable frequency control CPT system were developed. Specific advantages of using SS topology for battery charging application were discussed. Constant current source mode and constant voltage source mode operation of a SS compensated topology were discussed. Finally, based on the design criteria developed, a 100W CPT experimental system with 50 mm air gap was built.

References

[1] Fernandez, C.; Garcia, O.; Prieto, R.; Cobos, J.A.; Gabriels, S.; Van Der Borght, G.; , "Design issues of a core-less transformer for a contact-less application," Applied Power Electronics Conference and Exposition, 2002. APEC 2002. Seventeenth Annual IEEE , vol.1, no., pp.339-345 vol.1, 2002

[2] Chwei-Sen Wang; Stielau, O.H.; Covic, G.A.; , "Load models and their application in the design of loosely coupled inductive power transfer systems," Power System Technology, 2000. Proceedings. PowerCon 2000. International Conference on , vol.2, no., pp.1053-1058 vol.2, 2000

[3] Chwei-Sen Wang; Stielau, O.H.; Covic, G.A.; , "Design considerations for a contactless electric vehicle battery charger," Industrial Electronics, IEEE Transactions on , vol.52, no.5, pp. 1308- 1314, Oct. 2005

[4] A.K. Ramrakhyani, S. Mirabbasi and M. Chiao, "Design and optimization of resonance-based efficient wireless power delivery systems for biomedical implants", IEEE Trans. Biomed. Circuits and Systems, Vol. 5, No. 1, pp. 48-63 Feb. 2011

[5] Yungtaek Jang; Jovanovic, M.M.; , "A contactless electrical energy transmission system for portable-telephone battery chargers," Industrial Electronics, IEEE Transactions on , vol.50, no.3, pp. 520- 527, June 2003

[6] C. Sonntag, E. A. Lomonova and J. L. Duarte "Variable-phase contactless energy transfer desktop part I: Design", Proc. International Conference on Electrical Machines and Systems, ICEMS, pp. 4460-4465, Oct 2008.

[7] Sample, A.P.; Meyer, D.A.; Smith, J.R.; , "Analysis, Experimental Results, and Range Adaptation of Magnetically Coupled Resonators for Wireless Power Transfer," " IEEE Transactions on Industrial Electronics, vol.58, no.2, pp.544-554, Feb. 2011

[8] Keeling, N.A.; Covic, G.A.; Boys, J.T.; , "A Unity-Power-Factor IPT Pickup for High-Power Applications," Industrial Electronics, IEEE Transactions on , vol.57, no.2, pp.744-751, Feb. 2010

[9] G. A. Covic, G. Elliott, O. H. Stielau, R. M. Green and J. T. Boys, "The design of a contact-less energy transfer system for a people mover system", Proc. 2000 Int. Conf. Power System Technology, vol. 1, pp. 79–84, Dec. 2000.

[10] . Madawala, U. K.; Thrimawithana, D. J.; , "A Bi-directional Inductive Power Interface for Electric Vehicles in V2G Systems," Industrial Electronics, IEEE Transactions on , vol.PP, no.99, pp.1-8, Feb. 2011

[11] Sallan, J.; Villa, J.L.; Llombart, A.; Sanz, J.F.; , "Optimal Design of ICPT Systems Applied to Electric Vehicle Battery Charge," Industrial Electronics, IEEE Transactions on , vol.56, no.6, pp.2140-2149, June 2009

[12] Van der Pijl, F.F.A.; Ferreira, J.A.; Bauer, P.; Polinder, H.; , "Design of an Inductive Contactless Power System for Multiple Users," Industry Applications Conference, 2006. 41st IAS Annual Meeting. Conference Record of the 2006 IEEE , vol.4, no., pp.1876-1883, 8-12 Oct. 2006

[13] Van der Pijl, F.; Castilla, M.; Bauer, P.; , "Implementation of an adaptive sliding-mode control for a quantum series-resonant converter," Power Electronics and Applications, 2009. EPE '09. 13th European Conference on , vol., no., pp.1-10, 8-10 Sept. 2009

[14] F.van der Pijl. M. Castillia; Bauer, P.; "Control Method for Wireless Inductive Energy Transfer Systems with Relative Large Air Gap;" IEEE Transaction on Industrial Electronics, accepted paper, ISSN: 0278-0046

Appendix B- Paper II

Paper Title: Driving range extension of an EV with on-road contactless power transfer- A case study

Authors: S. Chopra, P. Bauer

Journal: *IEEE Transactions on Industrial Electronics*

Driving Range Extension of EV with On-road Contactless Power Transfer- A Case Study

Swagat Chopra, Pavol Bauer

Abstract— As future electric vehicles (EVs) emerge, achievable driving range by these vehicles remains a major bottleneck. A battery electric vehicle (BEV) has a fairly limited driving range per charging and takes long time to charge. Moreover, the existing technology only enables stationary charging which means that an EV has to be stationary during the duration of its charge replenishment. The use of contactless power transfer (CPT) systems presents the opportunity of on-road charge replenishment of EVs. This paper presents case studies which illustrate the effect of on-road charge replenishment on the driving range of an EV for varying levels of power transfer by CPT system. On-road charge replenishment of idle EV at traffic signal is considered for urban driving scenario whereas on-road charge replenishment of an EV in motion is considered for highway driving scenario.

Index Terms— Electric vehicles, contactless power transfer, charge replenishment, driving range

I. Introduction

CONTACTLESS power transfer (CPT) is the process of transferring power to an electrical load without any physical interconnection to the source. Inductively coupled power transfer (ICPT) is one of the widely researched topics in the field of CPT. This way of CPT is achieved through mutual coupling between coils in a manner similar to that in conventional transformers. However, the power is magnetically transferred from the source to the load over large air gaps. As a consequence of this large air gap, the mutual coupling coefficient between the primary and secondary winding of this transformer is very small when compared to that in conventional transformers.

It is more advantageous to transfer power through magnetically coupled windings than contact based systems as there is no physical connection between the source and the load, thereby reducing safety risks such as electric shocks and sparks in wet or dirty environment. ICPT systems are also more reliable and require less maintenance when compared to conventional contact based systems. Today these ICPT systems are being utilized in numerous applications like battery charging of EV [8]-[11], portable electronic devices [2]-[5], public transport [6]-[7], biomedical implants [1] etc.

CPT for charge replenishment in EVs can greatly simplify the charging process by making it more convenient for users to charge their EVs without the need of any physical connection between the vehicle and the charging point. The CPT charging systems can also be designed to allow bi-directional power flow [11] where vehicle-to-grid power flow is advantageous. The charge replenishment of an EV via CPT can be accomplished when the vehicle is parked and/or when the vehicle is on road. CPT charging systems for parked vehicles could be installed at homes, work places and public parking facilities just like the conventional EV charging stations. On-road charge replenishment of EVs can be achieved by CPT which can take place when an EV is either idle at a traffic signal or when in motion. To accomplish on-road charge replenishment, the primary winding of the CPT systems is buried underneath the road. Such on-road charging of EVs has advantage over conventional vehicles that energy replenishment can occur when the vehicle is in motion. On-road charge replenishment will lead to increase in driving range and/or reduction in onboard energy storage capacity of EVs which in turn would lead to wider acceptance of EVs.

In this paper, effect of on-road charge replenishment through CPT is investigated on the state of charge (SOC) of onboard battery of a BEV with the help of two case studies. To achieve this, all the components of the energy conversion chain in a BEV are modeled. A vehicle model is simulated to determine the energy requirement while driving and a battery model is simulated to determine the SOC of battery throughout the journey. These models are then incorporated in the case studies for urban and highway driving scenarios for which on-road charge replenishment through CPT is studied. Observations are made and conclusions are drawn based on the SOC of the battery for the two driving scenarios. But, to start with, technical concepts of a CPT system and measured efficiency of a small scale experimental CPT setup are presented.

II. CPT – Technical Aspects

The idea of CPT is not new but a lot of research is being pursued in this topic to find innovative solution which could lead to change in mindset of consumers toward EV technology by enhancing the range of EVs and making charging process simpler with respect to human interaction. Efficiency of a CPT system being perhaps the most important factor in determining the feasibility of such a system, an experimental setup has been built based on the CPT model presented in [8]. Series-series (SS) compensated [8] topology was chosen to boost the power transfer capability and to eliminate the reactive power requirement of the source when operating at secondary resonant frequency. Fig. 1 shows the circuit diagram of the SS compensated topology of CPT system. C_1 and C_2 are primary and secondary compensation capacitances respectively; L_a and L_b are primary and secondary winding leakage inductance of the CPT transformer respectively; R_1 and R_2 are the resistances associated with primary and secondary winding respectively; M is mutual inductance between primary and winding of the CPT transformer; C_f is the filter capacitor and R_L is the resistive load. Fig. 2 shows the experimental setup to demonstrate CPT over a distance of 50 mm.

The parameters of the experimental setup are tabulated in appendix Table. IV. The efficiency of the CPT transformer was measured to be 91% which is close to the efficiency obtained by simulation which was 95.2%. Since the operating frequency was 105 KHz, litz wire was used to construct the primary and secondary winding of the CPT transformer. Although rise in winding AC resistance due to skin effect was taken into consideration, rise in winding AC resistance due to proximity effect, because of geometrical complexity of the windings, was neglected in the simulations and hence the discrepancy in the simulated and measured efficiency. The overall efficiency of the system, however, was measured to be 83.2% owing to the losses in the inverter stage and the rectifier stage. This is a point for further research and beyond the scope of this paper.

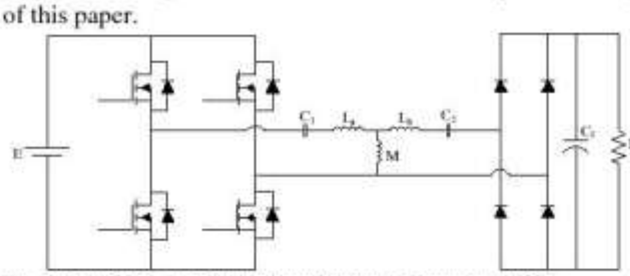

Fig. 1 Circuit diagram of experimental setup to demonstrate CPT

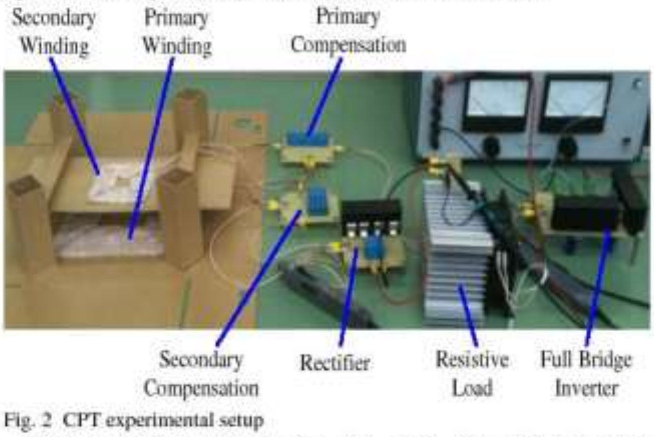

Fig. 2 CPT experimental setup

CPT systems with larger air gaps for EV charging application have been realized and presented in [5]-[7]. Fig. 3 shows the basic structure of a CPT system for this application. The primary winding of the CPT transformer is stationary, while in theory, the secondary could be either stationary (idle vehicle) or in motion (moving vehicle). The high frequency inverter block is a full bridge inverter with PWM control and switches at high frequencies to accomplish high efficiency CPT. PWM control is needed to avoid the transient current when the voltage is directly applied by the source. The DC-DC converter controls the charge flow to the battery based on the battery current and terminal voltage.

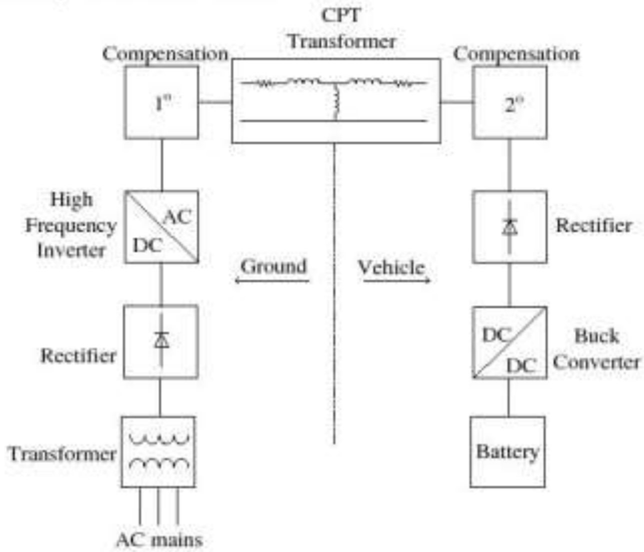

Fig. 3 Structure of a CPT system

III. Vehicle Model

The operational range of a BEV depends upon capacity of battery and the driving conditions. To determine the quantity and rate of energy transferred to and from a battery during driving conditions, a model that computes the energy needed to propel a typical vehicle is constructed. The simulated vehicle is a typical mid-size BEV [24]. The parameters of this BEV are tabulated in Table I.

Table I
Parameters of Simulated BEV

Vehicle	Mass	1600 kg
	Frontal area	2.7 m^2
	Co-efficient of rolling resistance	0.01
	Co-efficient of drag	0.28
Battery	Current capacity	90 Ah
	Energy capacity	24 kWh

The power requirement of a vehicle has following components [12]:

1) Base load P_{base} which consists of all on board electronic load. P_{base} is taken to be 800 W on account of the power needed for all activities unrelated to movement such as heater, air conditioner, radio, signals and other accessories [12].

2) Rolling resistance P_{roll} which is due to resistance offered by road to rolling motion of the wheels. P_{roll} is given by $C_{rr} mg\cos\theta|v|$ where C_{rr} is the co-efficient of rolling resistance, m is the mass of the vehicle, g is acceleration due to gravity, θ is the angle of inclination and v is the instantaneous velocity of the vehicle.

3) Aerodynamic drag P_{drag} which is due to resistance offered by air. P_{drag} is given by $1/2C_d\rho|v|^3 A$ where C_d is the co-

efficient of drag, ρ is the density of air taken as 1.23 kgm^{-3} and A is the frontal area of the vehicle.

4) Gravitational load P_g which is due to uphill/downhill driving. P_g is given by $mg\sin\theta|v|$.

5) Inertial load P_{acc} which is due acceleration/braking. P_{acc} is given by $ma|v|$ where a is the instantaneous acceleration of the vehicle.

$$P_{load} = P_{base} + P_{roll} + P_{drag} + P_g + P_{acc} \qquad (1)$$

Of all the loads mentioned above, apart from the base load, all other loads are dependant on velocity and/or acceleration of the vehicle. Also, P_g and P_{acc} could be positive or negative depending upon angle of inclination (which is positive when driving uphill and negative when driving downhill) and acceleration (which is positive when accelerating and negative when braking). There are certain assumptions made when building the model to calculate power flow to or from the battery of the BEV. These assumptions are as follows:

1) The electric drive train (electric motor, converter and transmission system) is assumed to have an overall efficiency of 80%

2) The efficiency of power transfer from wheels to batteries during regenerative braking is assumed to be 40%

3) The initial SOC of batteries is assumed to be 80%

4) Since there is no information about the angle of inclination of the road, it is assumed that the angle of inclination of road though-out the journey in all driving cycles under consideration to be zero i.e., $\sin\theta = 0$ and $\cos\theta = 1$. This means P_g=0

5) The overall efficiency of power transferred to a BEV via CPT system is assumed to be 80%

IV. Battery Model

To design the drive system of an electric vehicle, it is necessary to have a model that describes the electric behavior of a battery. In literature researchers have come up with many battery models. There are many factors that determine the performance of a battery and therefore to predict behavior of a battery, many battery models exist. Some of the important factors that determine the behavior and performance of a specific kind of battery are state-of-charge (SOC), battery storage capacity, rate of charge/discharge, temperature, age of the battery etc. Depending upon the specific purpose of the battery model, degrees of complexity of these models vary. Electrochemical models, Mathematical models and Electrical equivalent models are some of the most widely researched battery models available in literature.

Electrochemical models [14-16] are mainly used to optimize the physical design aspects of batteries characterizing fundamental mechanism of power generation. This model takes into consideration both microscopic and macroscopic information like battery voltage and current, and concentration distribution respectively. Mathematical models [17–19], are too abstract to attach any practical meaning. These models adopt empirical equations or mathematical methods like stochastic approaches to predict system-level behavior, such as battery runtime, efficiency, or capacity. Electrical models [20-22], are equivalent electrical circuit models using a combination of voltage sources, resistors, and capacitors for design and simulation with other electrical circuits and systems as in case of an EV performance simulation. Electrical models are more intuitive, useful, and easy to handle, especially when they can be used in simulators like Matlab SIMULINK.

The simplest of equivalent electrical model is as shown in Fig. 4. Such a circuit is apparently very simple, but in order for it to describe accurately the behavior of a real battery, both the open circuit voltage (indicated as $V_{B,OC}$) and the internal resistance (indicated as $R_{i,B}$) must change according to the state of charge (SOC) of the battery. This is true for all battery technologies, even though the dependency may be very different according to the particular chemistry and technology. The battery model used to study the behavior of the battery has been extensively covered in [23].

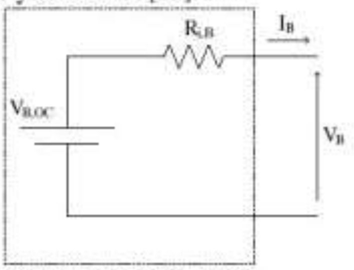

Fig. 4 Basic Thevenin equivalent battery model

In the battery model used, effects of certain parameters have not been taken into consideration. The dependency of battery performance on the cell temperature has been neglected. The model is also unable to predict the dynamic behavior of the battery as the pseudo-capacitance effects are neglected. Also, the effects due to the aging of the battery are neglected. But, the model used in the simulations can predict the performance of a vehicle in terms of range to a reasonable accuracy, so, more complex electrochemical models and mathematical models are not considered.

V. Case Study

The goal of this case study is to study the effect of on-road battery charge replenishment by CPT on the driving range of a BEV. To do that, the case study has been divided into two parts. In the first part, on-road battery charging when vehicle is idling at a traffic signal in urban driving conditions is considered. In the second part, on-road battery charging when vehicle is in motion in highway driving conditions is considered. The vehicle and battery model described are used to simulate the energy usage of a BEV. Fig. 5 shows the scheme followed to calculate the battery parameters from the available driving cycle data.

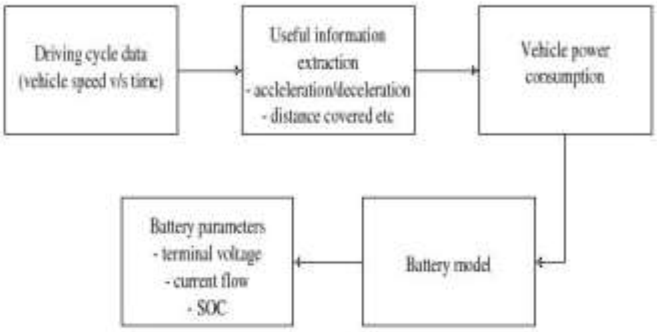

Fig. 5 Scheme - battery parameter calculation

A. Case study I

In case study I, it is studied how CPT system when installed underneath the roads at traffic signals would enhance the range of a BEV in urban driving conditions. To simulate this, three standard urban driving cycles are considered. These are the tests patterns which manufacturers have to refer to while stating their vehicles performance in terms of range and emission. These are

1) U.S. standard FTP 72 (Federal Test Procedure) cycle also called Urban Dynamometer Driving Schedule (UDDS)

2) European standard ECE-EUDC combined urban test cycle

3) Japanese standard JC08 urban test cycle

Some characteristics of these urban test cycles under consideration are tabulated in Table II. It is assumed that the time a vehicle spend idling during a journey in a test cycle is the time for which the vehicle has stopped at traffic signals.

TABLE II
CHARACTERISTICS OF THE THREE TEST CYCLES

	UDDS	ECE-EUDC	JC08
Duration (s)	1369	1180	1204
Distance travelled (km)	12.0	11.0	8.2
Average speed (kmph)	31.5	33.5	24.4
Maximum speed (kmph)	90.9	120	81.6
Time spent idling during the journey (s)	234	261	330
% time spent idling	17.1	22.1	27.4

Figs. 6-8 show the speed of the EV and battery parameters for UDDS, ECE-EUDC and JC08 driving cycles without any on-road charge replenishment. The change in SOC of battery during the journey was 7.8%, 7.4% and 5.3% respectively for UDDS, ECE-EUDC and JC08 driving cycles respectively.

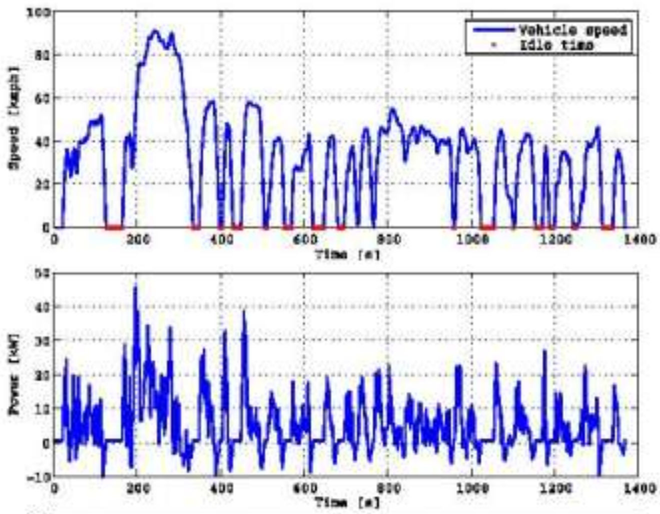

Fig. 6 Vehicle speed, battery power flow, battery terminal voltage and SOC of battery

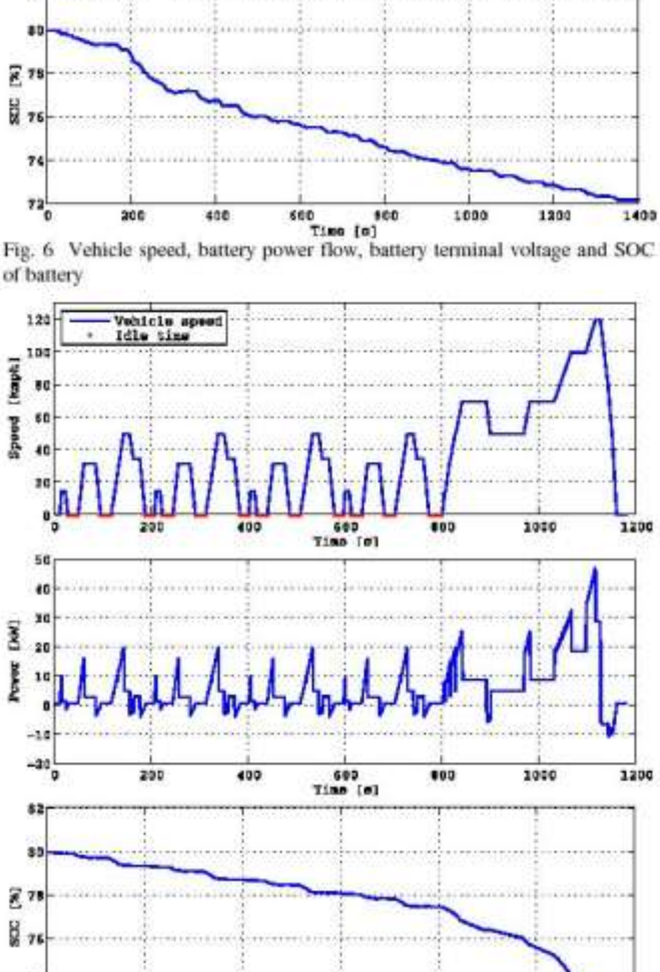

Fig. 7 Vehicle speed, battery power flow and SOC of battery for ECE-EUDC driving cycle

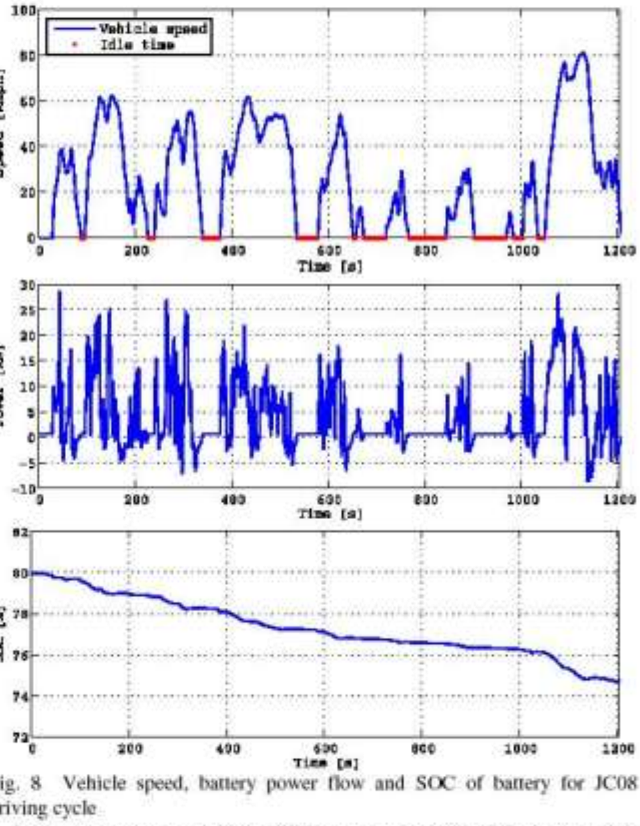

Fig. 8 Vehicle speed, battery power flow and SOC of battery for JC08 driving cycle

It is now assumed that CPT systems are installed at traffic signals which will replenish the battery charge when the vehicle is stationary at these traffic signals. These periods are indicated as 'ideal time' in Figs. 6-8 for UDDS, ECE-EUDC and JC08 cycles respectively. It is assumed that CPT systems at different traffic signals in the driving cycle under consideration are identical in terms of power rating. So, depending upon the time a vehicle is stationary at a traffic signal and the power rating of the installed CPT system, the amount of energy replenished to the battery varies. Figs. 9-11 show the SOC of the battery as function of time with power transferred via CPT system varying from 0 W to 40 kW for UDDS, ECE-EUDC and JC08 cycles respectively.

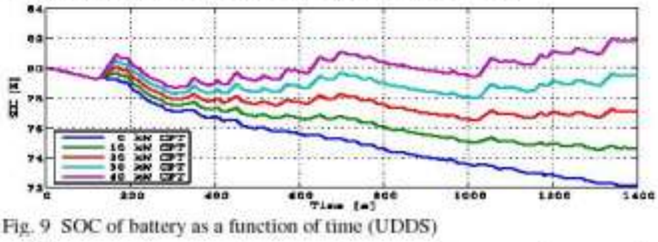

Fig. 9 SOC of battery as a function of time (UDDS)

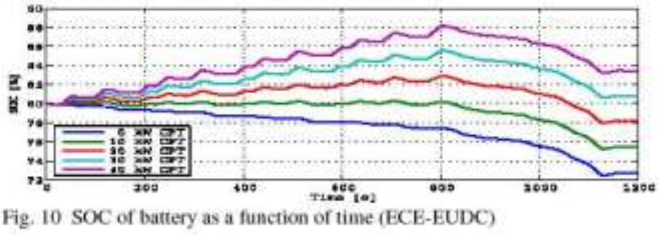

Fig. 10 SOC of battery as a function of time (ECE-EUDC)

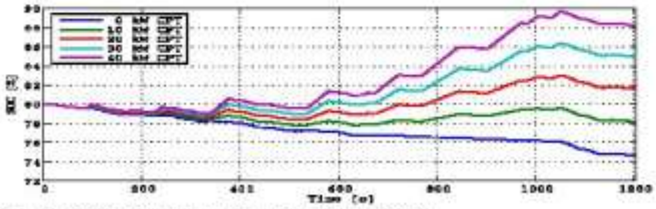

Fig. 11 SOC of battery as a function of time (JC08)

1) Observations

In case of UDDS and ECE-EUDC driving cycles, with 20 kW CPT, the change in SOC of battery during the journey has been reduced from 7.8% and 7.4% to 2.9% and 1.8% respectively when compared to the case when there is no CPT system installed as shown in Fig. 12. This means that with 20 kW CPT, the range of the vehicle has been more than doubled in both cases, i.e., an increase of 172% and 311% in range respectively in case of UDDS and ECE-EUDC driving cycles. Similarly, in case of JC08 driving cycle, with 10 kW CPT, the change in SOC of battery during the journey has been reduced from 5.3% to 1.8% which means that there is a 194% increase in the range of the vehicle. Another important observation is that in case of UDDS and ECE-EUDC driving cycles, with 30 kW CPT, the change in SOC of battery during the during the journey is close to 0%, which means that the SOC of battery at the end of the journey is approximately same as it was at the start of journey. Similarly, in case of JC08 driving cycle, this effect is seen with 20 kW CPT.

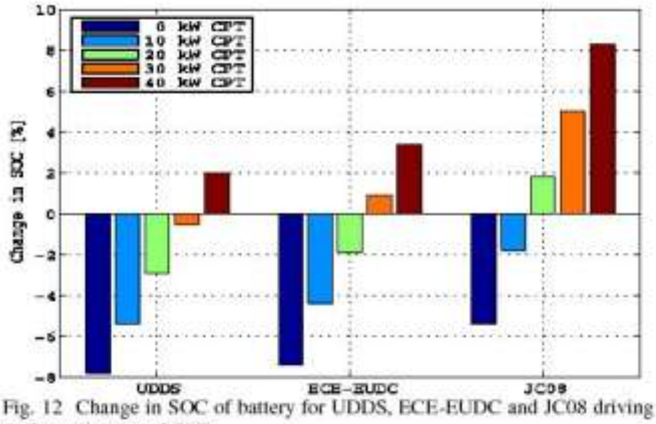

Fig. 12 Change in SOC of battery for UDDS, ECE-EUDC and JC08 driving cycles with on-road CPT

B. Case study II

In case study II, it is studied how CPT system installed underneath the highways would enhance the driving range of range of a BEV. To simulate this, HighWay Fuel Economic Test (HWFET) cycle has been considered. HWFET cycle is a US dynamometer driving schedule used by vehicle manufactures to determine fuel economy in highway driving conditions. To simulate a reasonable driving distance, two HWFET cycles are considered back to back. This new cycle is henceforth addressed to as HWFET2. Some characteristics of HWFET2 cycle are tabulated in Table III. Fig. 13 shows the speed of the EV and battery parameters for HWFET2 driving cycles without any on-road charge replenishment. The change in SOC of battery during the journey was 20%.

TABLE III
CHARACTERISTICS OF HWFET2 TEST CYCLE

Duration (s)	Distance travelled (km)	Average speed (kmph)	Maximum speed (kmph)
1526	32.9	77	96.4

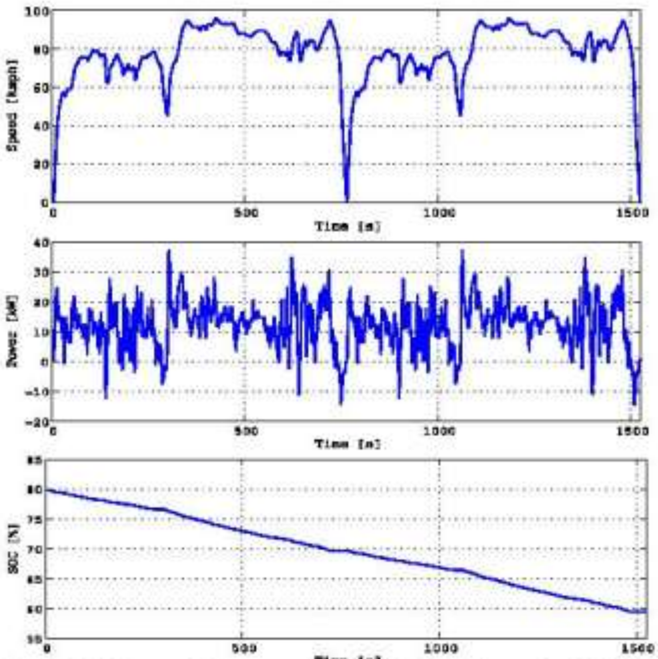

Fig. 13 Vehicle speed, battery power flow and SOC of battery for HWFET2 driving cycle

Unlike in urban cycles, in the highway cycle HWFET2 under consideration, the vehicle is never idle during the journey. So, in order to replenish charge to the battery, CPT has to be achieved when the vehicle is in motion. To accomplish this, the primary winding of the CPT system has to be laid underneath the road through different parts of highway. The average speed of the vehicle in HWFET2 cycle is 77 kmph which means that to achieve a reasonable enhancement in range of a BEV; a considerable length of road must be covered by the primary winding of CPT system. In this case study, the effect on range of the modeled BEV for varying road cover by primary winding of CPT system and varying amount of power transfer via CPT system is studied. To study the effect of varying coverage of highway by primary of the CPT system, it is assumed that there are 10 CPT systems that are deployed i.e., the highway is divided into 10 equally long segments with one CPT system deployed in each section as shown in Fig. 14.

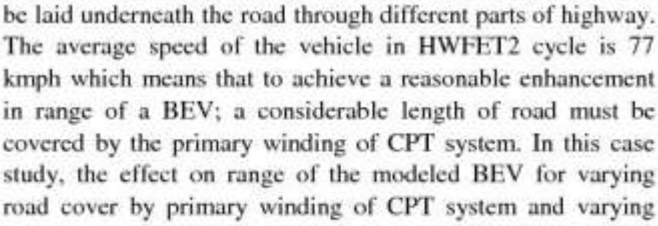

Fig. 14 Primary winding highway coverage

To determine the effect of power transferred via CPT system on SOC of the battery, CPT systems with varying amount of power transferred and varying percentages of highway cover by CPT system is incorporated in vehicle-battery energy model. Figs. 15-18 show the SOC of the battery during the journey for 10 kW, 20kW, 30 kW and 40 kW of power transfer via CPT system respectively for varying coverage of highway by primary winding of CPT system.

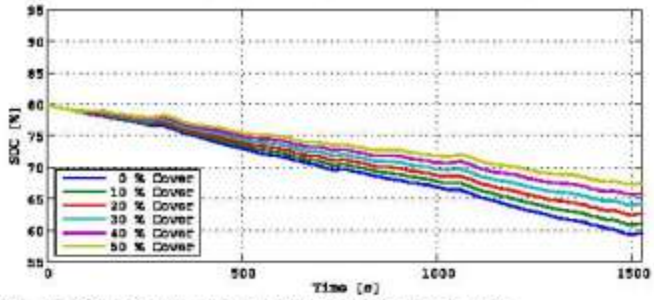

Fig. 15 SOC of battery as a function of time for 10 kW CPT

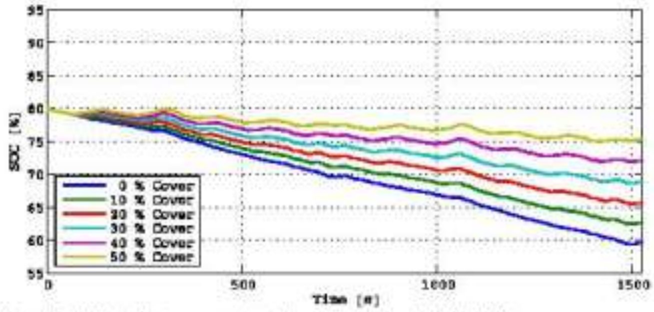

Fig. 16 SOC of battery as a function of time for 20 kW CPT

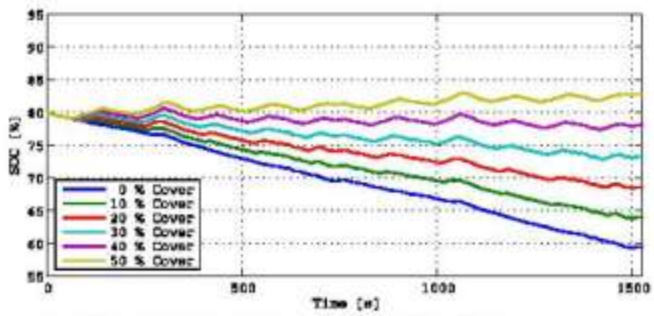

Fig. 17 SOC of battery as a function of time for 30 kW CPT

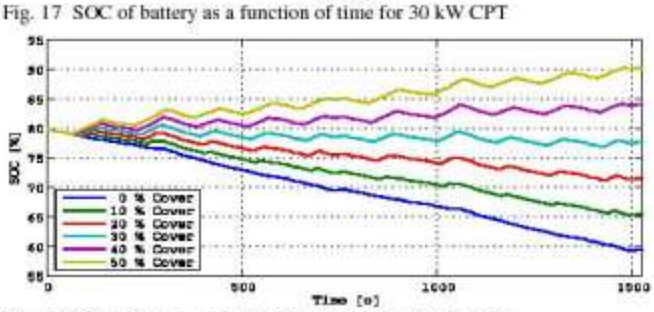

Fig. 18 SOC of battery as a function of time for 40 kW CPT

1) Observations

Comparison of change in SOC of battery for entire journey of HWFET2 cycle for varying power transmission levels via CPT and varying percentages of highway cover by primary winding of CPT system is shown in Fig. 19.

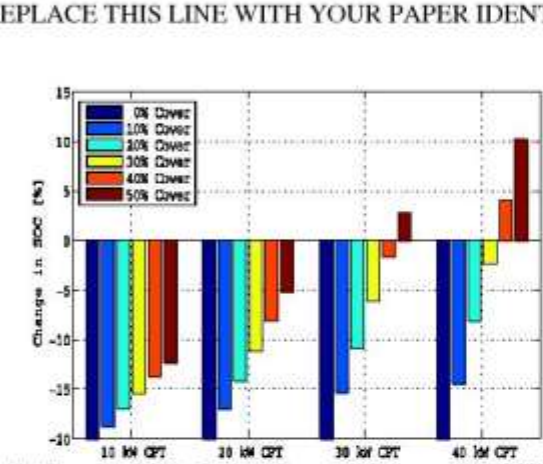

Fig. 19 Change in SOC of battery for entire journey of HWFET2 driving cycle

It can be observed that to achieve considerable enhancement in driving range, large lengths of highway needs to be covered with primary windings of CPT system. For e.g., 37% increase in range is achieved with CPT of 40 kW and highway cover of 10% (3.3 km) with primary winding of CPT system. With this large length of primary winding, efficient CPT is possible only when either frequency of operation is high enough or when number of CPT systems is large. Both of these solutions have their own economic and practical implications which need to be studied further in depth. Another factor that has been ignored in these simulations is the effect due to presence of more than one vehicle on the same stretch of road receiving power from same CPT system. This scenario is very probable and in this case, depending upon the number of vehicles on the stretch of road which is being powered by the same CPT system, power transfer to each vehicle will only be a fraction of power that was initially assumed. These are some of the some of the challenges which need to be looked into in future research.

APPENDIX

TABLE IV
PARAMETERS OF THE EXPERIMENTAL SETUP

L_a (μH)	100
L_b (μH)	8.9
M (μH)	6.5
R_1(Ω)	0.13
R_2(Ω)	0.04
R_L(Ω)	2.5
C_1(nF)	22
C_2(nF)	168
Frequency f (kHz)	105
%Efficiency (transformer)	91
%Efficiency (overall)	83.2

REFERENCES

[1] A.K. Ramrakhyani, S. Mirabbasi and M. Chiao, "Design and optimization of resonance-based efficient wireless power delivery systems for biomedical implants", IEEE Trans. Biomed. Circuits and Systems, Vol. 5, No. 1, pp. 48-63 Feb. 2011

[2] Y. Jang and M. Jovanovic, "A contactless electrical energy transmission system for portable-telephone battery chargers", IEEE Transactions on Industrial Electronics, vol. 50, no. 3, pp. 520–527, Jun. 2003

[3] C. Sonntag, E. A. Lomonova and J. L. Duarte "Variable-phase contactless energy transfer desktop part I: Design", Proc. International Conference on Electrical Machines and Systems, ICEMS, pp. 4460-4465, Oct 2008.

[4] X. Liu and S. I. Hui, "Optimal design of a hybrid winding structure for planar contactless battery charging platform", IEEE Trans. Power Electron., vol. 23, no. 1, pp. 455–463, Jan. 2008.

[5] Sample, A.P.; Meyer, D.A.; Smith, J.R.; , "Analysis, Experimental Results, and Range Adaptation of Magnetically Coupled Resonators for Wireless Power Transfer," " IEEE Transactions on Industrial Electronics, vol.58, no.2, pp.544-554, Feb. 2011

[6] G. A. Covic, G. Elliott, O. H. Stielau, R. M. Green and J. T. Boys, "The design of a contact-less energy transfer system for a people mover system", Proc. 2000 Int. Conf. Power System Technology, vol. 1, pp. 79–84, Dec. 2000.

[7] N.A. Keeling, G.A. Covic and J.T. Boys, "A Unity-Power-Factor IPT Pickup for High-Power Applications," IEEE Transactions on Industrial Electronics, vol.57, no.2, pp.744-751, Feb. 2010

[8] J. Sallan, J.L. Villa, A. Llombart and J.F. Sanz, "Optimal design of ICPT systems applied to electric vehicle battery charge" IEEE Transactions on Industrial Electronics, vol. 56, pp. 2140–2149, Jun. 2009

[9] M. Budhia, G. A. Covic and J. T. Boys, "Design and optimization of magnetic structures for lumped Inductive Power Transfer systems", Energy Conversion Congress and Exposition, 2009. ECCE, pp. 2081-2088, 2009.

[10] G. Elliott, S. Raabe, G. A. Covic, and J. T. Boys, , "Multiphase Pickups for Large Lateral Tolerance Contactless Power-Transfer Systems," IEEE Transactions on Industrial Electronics, vol. 57, pp. 1590-1598, May 2010

[11] U. K. Madawala and D. J. Thrimawithana, "A bi-directional inductive power interface for Electric Vehicles in V2G systems," IEEE Transactions on Industrial Electronics, vol. 99, pp. 1-8, Feb. 2011

[12] J. Larminie and J. Lowry, "Electric vehicle technology explained", John Wiley & Sons, Ltd., England, 2003

[13] R. Farrington and J. Rugh, "Impact of Vehicle Air-Conditioning on Fuel Economy, Tailpipe Emissions, and Electric Vehicle Range" (2000) http://www.nrel.gov/docs/fy00osti/28960.pdf.

[14] L. Song and J. W. Evans, "Electrochemical-thermal model of lithium polymer batteries,"J. Electrochem. Soc., vol. 147, pp. 2086–2095, 2000.

[15] P. M. Gomadam, J. W. Weidner, R. A. Dougal, and R. E. White, "Mathematical modeling of lithium-ion and nickel battery systems," *J. Power Sources*, vol. 110, no. 2, pp. 267–24, Aug. 2002.

[16] D.W. Dennis, V. S. Battaglia, and A.Belanger, "Electrochemical modeling of lithium polymer batteries," J. Power Source, vol. 110, no. 2, pp. 310–320, Aug. 2002.

[17] R. Rynkiewicz, "Discharge and charge modeling of lead acid batteries," Proc. Appl. Power Electron. Conf. Expo., vol. 2, pp. 707–710, 1999.

[18] D. Rakhmatov, S. Vrudhula, and D. A. Wallach, "A model for battery lifetime analysis for organizing applications on a pocket computer," IEEE Trans. VLSI Syst., vol. 11, no. 6, pp. 1019–1030, Dec. 2003.

[19] P. Rong and M. Pedram, "An analytical model for predicting the remaining battery capacity of lithium-ion batteries," Proc. Design, Automation, and Test in Europe Conf. and Exhibition, pp. 1148–1149, 2003.

[20] B. Schweighofer, K. M. Raab, and G. Brasseur, "Modeling of high power automotive batteries by the use of an automated test system," IEEE Trans. Instrum. Meas., vol. 52, no. 4, pp. 1087–1091, Aug. 2003.

[21] L. Gao, S. Liu, and R. A. Dougal, "Dynamic lithium-ion battery model for system simulation," IEEE Trans. Compon. Packag. Technol., vol. 25, no. 3, pp. 495–505, Sep. 2002.

[22] M. C. Glass, "Battery electrochemical nonlinear/dynamic SPICE model," in Proc. Energy Convers. Eng. Conf., vol. 1, pp. 292–297, 1996.

[23] Tremblay, O., Dessaint, L.-A. "Experimental Validation of a Battery Dynamic Model for EV Applications." World Electric Vehicle Journal. Vol. 3 - ISSN 2032-6653 -2009 AVERE, EVS24 Stavanger, Norway, May 13 - 16, 2009.

[24] Nissan USA, 2011, http://www.nissanusa.com/leaf-electric-car/index#/leaf-electric-car/specs-features/index